UNIVERSITY OF ROCHESTER
LABORATORY FOR LASER ENERGETICS

Volume 96
July-September 2003
DOE/SF/19460-509

LLE Review

Quarterly Report

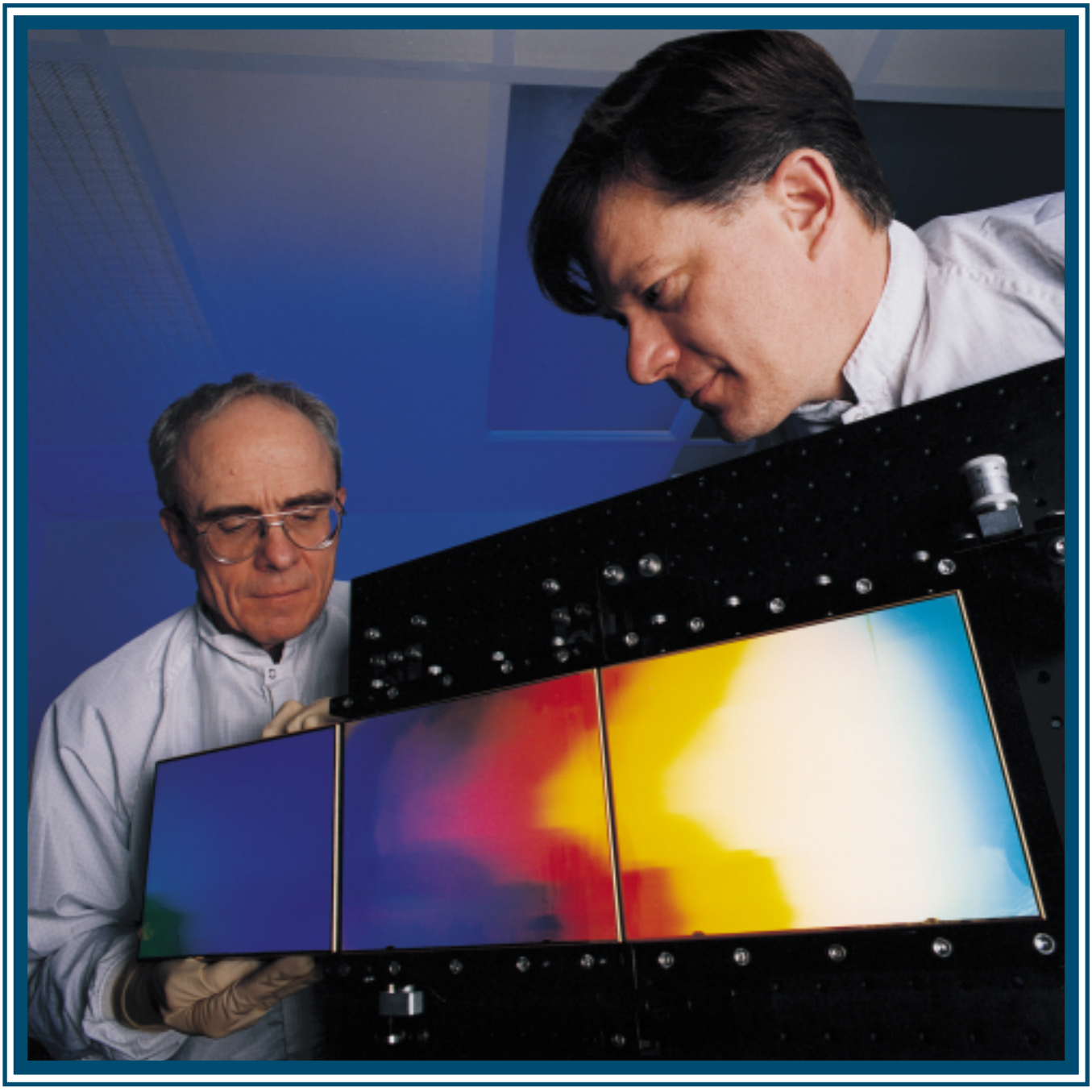

About the Cover:

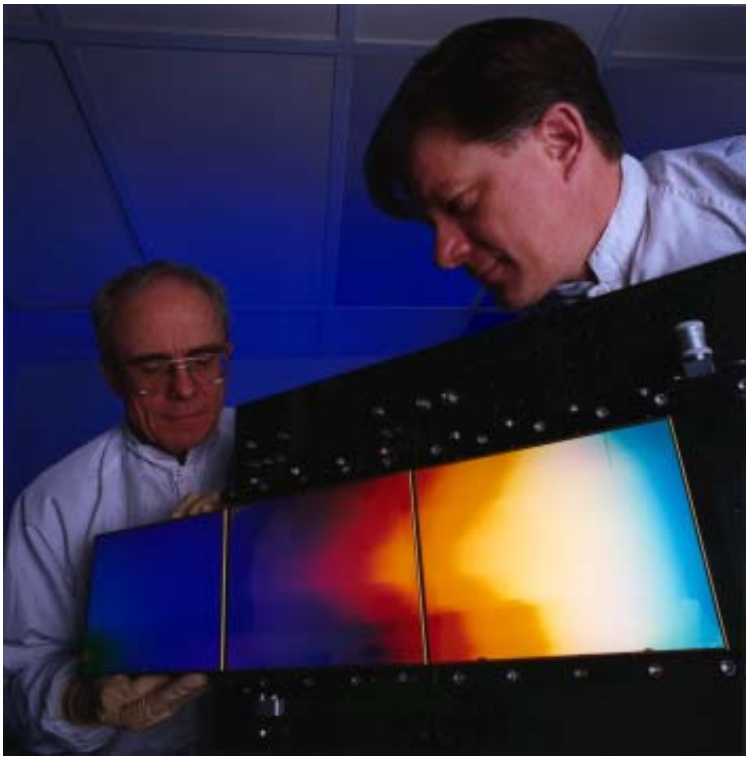

The realization of multikilojoule, multipetawatt laser systems will require very-large-area diffraction gratings to achieve compression of the laser pulse width prior to focusing on target. At present, it is not possible to manufacture monolithic gratings suitable for the OMEGA EP laser; however, Senior Research Engineer Terry Kessler (right) and Research Engineer Joe Bunkenburg show how smaller diffraction gratings can be tiled to create what is effectively a single large-area optic. In this issue, they conclusively demonstrate that a multiple-grating assembly can be aligned to behave as a single optic. These results have enabled the OMEGA EP project team to design large-aperture-grating compressors using commercially available optics. Indeed, the gratings designed for the OMEGA EP compressor will consist of three subgratings where each grating is about four times the area of those shown in the photograph.

The work described in this volume includes current research at the Laboratory for Laser Energetics, which is supported by New York State Energy Research and Development Authority, the University of Rochester, the U.S. Department of Energy Office of Inertial Confinement Fusion under Cooperative Agreement No. DE-FC03-92SF19460, and other agencies.

Printed in the United States of America
Available from
National Technical Information Services
U.S. Department of Commerce
5285 Port Royal Road
Springfield, VA 22161

Price codes: Printed Copy A05
Microfiche A01

For questions or comments, contact T. Craig Sangster, *Editor*, Laboratory for Laser Energetics, 250 East River Road, Rochester, NY 14623-1299, (585) 273-2350.

Worldwide-Web Home Page: http://www.lle.rochester.edu/

UNIVERSITY OF ROCHESTER
LABORATORY FOR LASER ENERGETICS

Volume 96
July–September 2003
DOE/SF/19460-509

LLE Review

Quarterly Report

UR LLE

Contents

In Brief

This volume of the LLE Review, covering July–September 2003, features "The Coherent Addition of Gratings for Pulse Compression in High-Energy Laser Systems" by T. J. Kessler, J. Bunkenberg, H. Huang, A. Kozlov, C. Kelly, and D. D. Meyerhofer (p. 207). This article describes the conceptual development and experimental demonstration of the coherent summation of multiple gratings to form a larger grating. The most-promising reflection-grating technology for short-pulse, high-energy petawatt-class laser systems utilizing chirped-pulse amplification (CPA) is a holographically formed grating combined with a multilayer dielectric (MLD) coating. The aperture size and damage threshold of such gratings determine the ultimate short-pulse energy capability of these laser systems. Current state-of-the-art gratings would limit a laser such as OMEGA EP to an energy of less than 1 kJ per beam. While it may be possible in the future to manufacture very large gratings, tiling the MLD gratings available today represents an extremely attractive alternative for the OMEGA EP. The key result presented in this article is the conclusive demonstration of subpicosecond pulse compression using tiled gratings. This is truly an enabling technology for the high-energy, short-pulse lasers planned for the coming decade.

Additional highlights of research presented in this issue include the following:

- S. Skupsky, J. A. Marozas, R. S. Craxton, R. Betti, T. J. B. Collins, V. N. Goncharov, P. W, McKenty, P. B. Radha, T. R. Boehly, J. P. Knauer, F. J. Marshall, D. R. Harding, J. D, Kilkenny, D. D. Meyerhofer, T. C. Sangster, and R. L. McCrory (p. 212) examine the feasibility of using the x-ray-drive beam configuration at the National Ignition Facility (NIF) to achieve direct-drive ignition. The baseline x-ray-drive beam configuration was designed to illuminate a vertically oriented hohlraum with beams arrayed symmetrically around the polar regions of the target chamber. The authors realized that nearly symmetric direct-drive illumination could be achieved by repointing some of the polar beams toward the equator of the capsule and adjusting the beam-spot sizes and energies. This new drive concept is called polar direct drive (PDD), and the authors describe the current status of their work focusing, in particular, on the beam-pointing strategy. The long-term impact of this work within the national ICF program is potentially of great importance if ignition conditions can be achieved on the NIF using the PDD concept.

- T. R. Boehly, T. J. B. Collins, E. Vianello, and D. D. Meyerhofer of LLE along with D. G. Hicks, P. M. Celliers, J. H. Eggert, S. J. Moore, and G. W. Collins of LLNL (p. 220) provide the latest experimental results on the equation of state (EOS) of hydrogen at pressures of a few megabars, temperatures of a few electron volts, and compressions of up to several times liquid density. A better understanding of the hydrogen EOS is important for the accurate simulation of direct and indirect ignition target designs on the NIF. At present, there are several different models for the hydrogen EOS, and it is exceptionally difficult to measure experimental observables with sufficient accuracy to discriminate among the models. The experimental results reported here are based on a new re-shock technique that is more sensitive to differences between the EOS models.

- V. Bagnoud and J. D. Zuegel (p. 225) describe a method to modulate both the phase and amplitude of a laser beam with a single-phase-only spatial light modulator (SLM) using a carrier spatial frequency and a spatial filter. With this technique, the authors show that dynamic corrections to a laser-beam profile are possible.

- V. Yu. Glebov, C. Stoeckl, S. Roberts, T. C. Sangster along with J. A. Frenje and R. D. Petrasso of PSFC-MIT and R. A. Lerche and R. L. Griffith of LLNL (p. 230) report on the implementation of an important new diagnostic system for direct-drive-implosion studies on the OMEGA laser system. The proton temporal diagnostic (PTD) was designed to measure the fusion reaction history in capsule implosions containing D^3He fuel. By measuring the temporal emission history and final energy spectrum of this high-energy proton, it is possible to study the areal-density evolution of the shell during the shock and compressive burn phases of an implosion. Existing range-filter spectrometers routinely measure the high-energy proton spectra from both D_2 and D^3He implosions. This data can now be combined with the temporal emission history of the new PTD to provide new constraints on the multidimensional hydrocodes used to understand implosion performance on OMEGA.

- J. DeGroote, H. J. Romanofsky, I. A. Kozhinova, J. M. Schoen, and S. D. Jacobs (p. 239) report on the use of conventional magnetorheological finishing (MRF) techniques to improve the surface finish and figure of several standard polymer optics. Since these optics are generally soft with high linear expansion coefficients and poor thermal conductivities, they are typically used as manufactured even though, in some instances, it would be desirable to have much better surface finishes. In this article, the authors show that the rms surface roughness of four different optical polymers can be reduced significantly using MRF.

- This volume concludes with a summary of LLE's Summer High School Research Program (p. 250), the FY03 Laser Facility Report (p. 252), and the National Laser Users' Facility and External Users' Programs (p. 254).

T. Craig Sangster
Editor

The Coherent Addition of Gratings for Pulse Compression in High-Energy Laser Systems

Introduction

Short-pulse, high-energy, and high-irradiance laser systems provide many new opportunities for studies in light–matter interaction and inertial confinement fusion, including x-ray radiography and fast ignition. Research in high-intensity, high-energy backlighting for high-energy-density physics experiments under ignition conditions and integrated fast-ignition experiments with cryogenic targets depend on the development of short-pulse, high-irradiance lasers.[1] High-power, solid-state lasers, using the chirped-pulse-amplification (CPA) scheme, incorporate pulse compressors containing holographic gratings.[2] The most-promising grating technology is a holographically formed grating combined with a multilayer dielectric (MLD) coating to form a highly efficient grating used in reflection.[3–5] The four primary grating requirements, namely high diffraction efficiency, high wavefront quality, large aperture, and high damage threshold, make it a highly constrained optical system. The aperture size and damage threshold of reflection gratings determine the short-pulse energy capability of petawatt laser systems. The critical compressor component is the last grating, which experiences the shortest pulse and therefore the highest power. The highest reported damage threshold for commercially available MLD gratings is 0.6 J/cm^2 at 275-fs pulse width.[6] Assuming a square root of time scaling, these gratings would have a damage threshold of ~1.2 J/cm^2 for a 1-ps pulse width. For a grating with 1740 l/mm and a Littrow angle of 66.5° for $\lambda = 1054$ nm, this surface fluence corresponds to a beam fluence, measured in a plane normal to beam propagation, of approximately 3 J/cm^2. These gratings are currently available in approximately 50-cm lengths. Assuming a 1.8 safety factor for diffraction modulation, the above provides an energy of less than 1 kJ. Gratings with larger apertures can further extend the short-pulse energy capability of petawatt laser systems; however, since the difficult fabrication process for MLD reflection gratings may limit the ultimate size of an individual grating to less than 1 m, alternative approaches are critical to scaling toward multiple-kilojoule, short-pulse laser systems.

Concept Description

The coherent summation of multiple gratings to form a larger grating provides an alternative to meter-sized MLD gratings. We refer to this alternative as grating tiling. A tiled-grating compressor (TGC) is capable of handling greater laser energy than a grating-aperture–limited compressor. For each of the gratings within the compressor, $N \times M$ sub-aperture gratings can be mounted adjacently to form a larger tiled grating.[7] When properly aligned, they will act as a monolithic optical element. For example, Fig. 96.1 shows a four-grating compressor with each tiled grating containing three sub-aperture gratings. The configuration is being considered for the OMEGA EP laser system. In general, the aperture, and therefore the energy, of a TGC is increased by a factor of $N \times M$ over that of grating-aperture–limited compressors. Similar to the scheme deployed by the astronomy community to construct very large telescopes[8] using an array of mirrors, large gratings can be assembled from multiple smaller gratings. Accurate control of the position and orientation of the grooves of each grating presents a significantly greater challenge than that associated with mirror arrays. Despite the perceived difficulty, we have developed a far-field–based approach that makes grating tiling practical.[9,10] As shown in Fig. 96.2, there are five degrees of freedom between each adjacent pair of gratings within a tiled-grating system: tip, tilt, rotation, in-plane shift, and out-of-plane shift. However, only three distinct types of optical path differences exist between closely aligned grating pairs. Relative shifts along the x and z axes result in a differential piston phase between the grating pairs. Similarly, relative rotations about the x and z axes result in a differential tilt phase between the grating pairs. Relative rotation about the y axis results in an additional tilt, while the relative shift along the y axis is inconsequential since it is parallel to the grooves of the grating. Relative tilt resulting from relative rotation about the x axis can be used to compensate relative groove rotation. In addition, the out-of-plane shift, also referred to as the piston phase error, can be used to compensate the residual error caused by the finite space between two adjacent gratings. The

effect of piston misalignment was modeled thoroughly. Theoretical simulations show the far-field irradiance resulting from relative piston-type phase error between two tiled gratings (Fig. 96.3, calculation). A half-wave piston-type error causes the focal spot to split into two symmetric spots of equal energy and irradiance. Experimental verification of the predictions for zero and half-wave errors indicates accurate control of the relative phase between the pair of tiled gratings as described below (Fig. 96.3, measurement). We experimentally observed that the majority of the focal-spot degradation occurs closer to the half-wave error, indicating a relative insensitivity in the vicinity of piston phase error, which is a multiple of 2π.

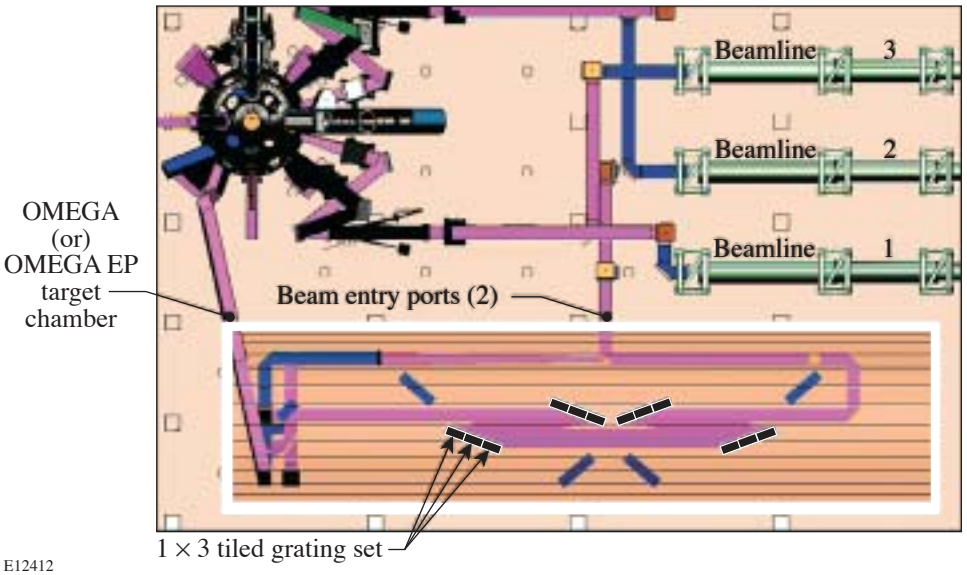

Figure 96.1
Tiled-grating compressors (TGC's) are capable of handling greater laser energy than a grating-aperture–limited compressor. For each of the gratings within a TGC, $N \times M$ sub-aperture gratings can be adjacently mounted to form a larger tiled grating. Shown here is a four-grating compressor with each tiled grating containing three sub-aperture gratings. The aperture, and therefore the energy, is increased by a factor of $N \times M$ over that of grating-aperture–limited compressors.

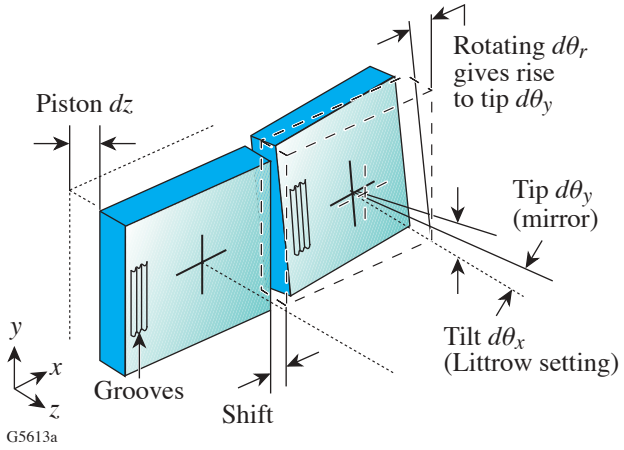

Figure 96.2
There are five degrees of freedom between each adjacent pair of gratings within a tiled-grating system. Relative shifts along the x and z axes result in a differential piston phase between the grating pairs. Similarly, relative rotations about the x and z axes result in a differential tilt between the grating pairs. Relative rotation about the y axis results in an additional tilt, while relative shift along the y axis is inconsequential since it is parallel to the grooves of the grating.

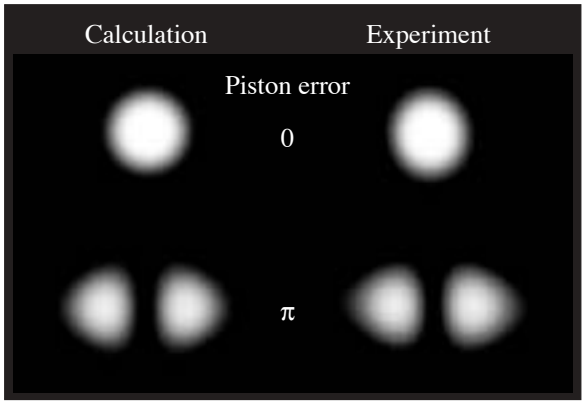

Figure 96.3
Theoretical simulations show the far-field effects from a relative piston phase error between two gratings. A π-phase shift causes the focal spot to split into two symmetric spots of equal energy and irradiance. Experimental verification of the predictions for zero and half-wave errors was achieved through accurate control of the relative piston.

Experimental Demonstrations

The feasibility of precise grating tiling was first demonstrated with continous-wave, monochromatic laser light. The tiled-grating assembly was located within a diagnostic package consisting of a Fizeau interferometer and a focal-plane sensor. An ADE Phase Shift MiniFiz,™ Model 100 interferometer contained a laser source that illuminated a pair of Jobin Ivon 165 × 220-mm gratings, with 1740 l/mm, set up in a Littrow configuration. The gratings were independently mounted within a precision assembly to achieve submicron positioning. A Zygo transmission flat, inserted into the Fizeau cavity, served as a beam splitter to pick off a portion of the beam reflected from the tiled grating. This beam was focused by a long-focal-length lens to form an aerial image. The image was magnified and relayed by an infinity-corrected, 10× microscope objective for far-field detection with a Spectral Instruments, Model 802, CCD camera. This diagnostic package provided accurate control of the phase front, thus allowing detailed studies of the focal-plane irradiance. As shown in Fig. 96.4, near-diffraction-limited performance was obtained with a pair of tiled gratings. The measured encircled energy, truncated at e^{-2} of the azimuthally averaged irradiance, was 0.89 with a Strehl ratio of 0.94. The measured focal-spot diameter was 1.2 to 1.3 times diffraction limited (XDL) as compared to an Airy-disc diameter corresponding to 84% encircled energy. For reference, the focal spot resulting from a π piston error is theoretically calculated to be 2.4 XDL. The small departure from theoretical predictions of ideal alignment is attributed to the cumulative wavefront error of the optics.

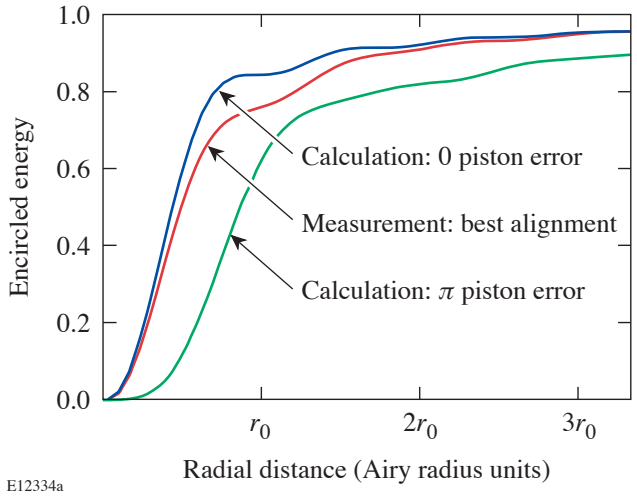

Figure 96.4
Near-diffraction-limited performance was obtained with a pair of tiled gratings. The measured encircled energy, truncated at e^{-2} of the azimuthally averaged irradiance, was 0.89 with a Strehl ratio of 0.94. The measured focal-spot diameter was 1.2 to 1.3 times diffraction limited (XDL) as compared to an Airy-disc diameter corresponding to 84% encircled energy.

A demonstration of precise grating tiling was achieved by high-fidelity pulse compression within a CPA laser. The autocorrelation trace, corresponding to a Fourier-transform–limited, 650-fs, CPA laser pulse, was maintained after including a tiled-grating pair. A Positive Light laser consisted of a positively chirped, Time-Bandwidth GLX-200,™ mode-locked oscillator followed by a Spitfire,™ Ti:sapphire, regenerative amplifier. The amplifier output was a linearly chirped, nanosecond pulse with 250 ps/nm. The laser was operated at 540 Hz with 350 μJ per pulse without subsequent amplification. In normal operation the output pulse was compressed with a two-grating, two-pass compressor consisting of gold gratings with 1740 grooves per millimeter. For our demonstration of a TGC, the first grating, and necessarily the last grating in the compressor, was replaced by two tiled gratings with the same line spacing.

In a two-pass grating compressor, only the second and third gratings intercept a beam with spatial chirp of its spectrum. Both the physical gap between tiled gratings and the obscuration at the edge of each grating, where excessive wavefront gradients may need to be masked, give rise to modifications of the spectrum that can potentially cause pulse-shape distortion. Modeling of a partially dispersed beam propagated through an accurately tiled grating indicates that the primary effect from grating-to-grating gaps is pulse broadening. The percentage of broadening is approximately equal to the product of the beam-normalized gap width and beam-normalized spectral separation. For the large laser systems for which this research is aimed, this product is at most only a few percent. For the laser system used to demonstrate grating tiling, however, pulse-width broadening would have exceeded 50%; thus, accurate control of piston and tilt control would have been masked by unrelated obscuration effects. For this reason, only the first (fourth) grating was tiled. Construction of an all-tiled grating compressor is in progress and will be the subject of a future publication. A scanning, far-field autocorrelator was used to measure the compressed temporal pulse. As shown in the autocorrelation traces of Fig. 96.5, negligible pulse broadening and distortion were measured. Accurate control of the relative position of the tiled gratings, as well as accurate alignment of the TGC, resulted in compressed pulses of the same quality as those generated from a conventional grating compressor.

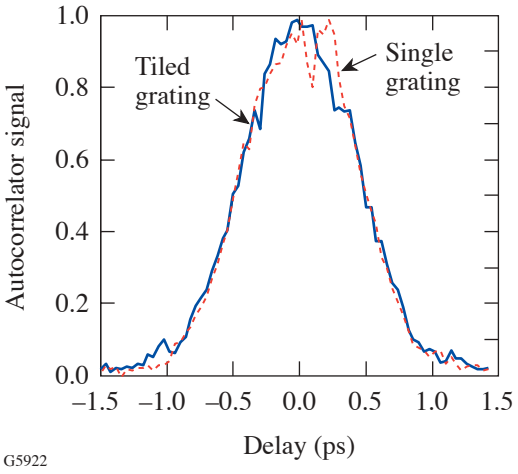

Figure 96.5
The autocorrelation trace, corresponding to a Fourier-transform–limited, 650-fs, CPA laser pulse, was maintained by replacing a single compression grating with a tiled-grating assembly. Negligible pulse broadening and distortion, as shown in the autocorrelation traces, indicate accurate control of the relative positioning of the tiled gratings as well as accurate alignment of the grating compressor.

A test bed for mounting and aligning a reduced-scale TGC for the OMEGA EP laser system is in progress. Schematically illustrated in Fig. 96.6, the tiled-grating system incorporates currently available pointing, sensor, and positioning technology. In particular, flexure mounts provide optimal characteristics for grating mounts. While flexures offer high mechanical stiffness to carry the weight of the grating substrates, they allow extremely fine motion control in the orthogonal direction. In addition, spatial synchronous phase detection can be used for accurate interferometry to monitor differential piston and tilt.

Conclusion

In conclusion, our investigations of coherently combined gratings have resulted in the demonstration of subpicosecond-pulse compression using tiled gratings. A Fourier-transform–limited, 650-fs, CPA laser pulse was maintained by replacing a single compression grating with a tiled-grating assembly. Despite the perceived difficulty, we have developed a far-field–based approach that makes grating tiling practicable. We anticipate that, in conjunction with future improvements in grating size and damage threshold, the tiled-grating compressor will significantly increase the energy and irradiance available in high-energy, short-pulse lasers.

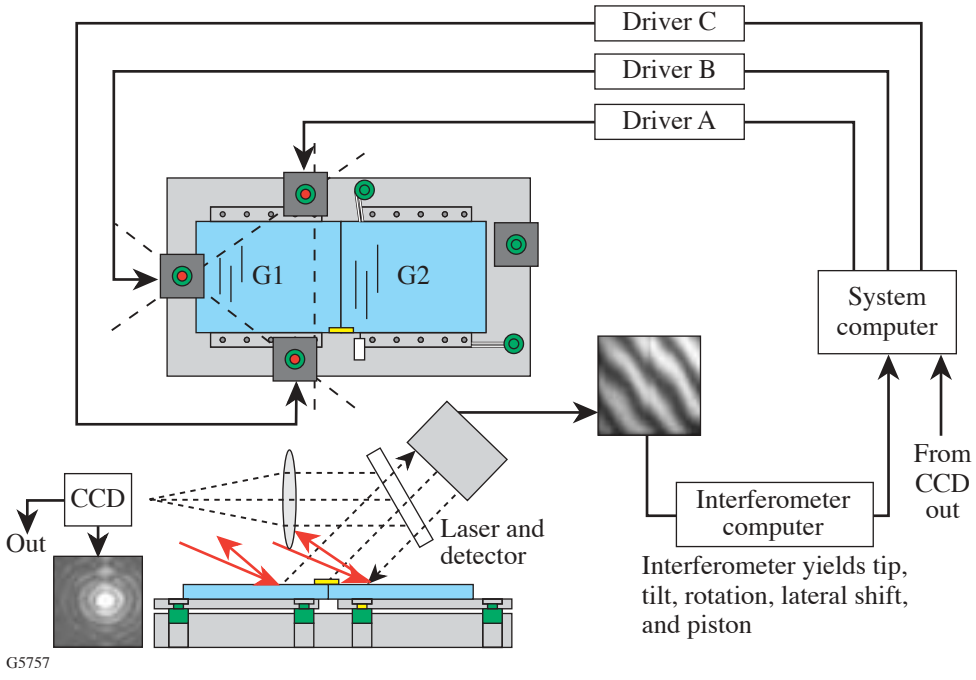

Figure 96.6
Tiled-grating systems incorporate currently available technology for mounting and alignment. Mechanical flexures provide extremely fine motion control for relatively heavy grating substrates. The interferometer yields tip, tilt, rotation, lateral shift, and piston information.

ACKNOWLEDGMENT

This work was supported by the U.S. Department of Energy Office of Inertial Confinement Fusion under Cooperative Agreement No. DE-FC03-92SF19460, the University of Rochester, and the New York State Energy Research and Development Authority. The support of DOE does not constitute an endorsement by DOE of the views expressed in this article.

REFERENCES

1. D. M. Pennington, C. G. Brown, T. E. Cowan, S. P. Hatchett, E. Henry, S. Herman, M. Kartz, M. Key, J. Koch, A. J. MacKinnon, M. D. Perry, T. W. Phillips, M. Roth, T. C. Sangster, M. Singh, R. A. Snavely, M. Stoyer, B. C. Stuart, and S. C. Wilks, IEEE J. Sel. Top. Quantum Electron. **6**, 676 (2000).
2. P. Maine *et al*., IEEE J. Quantum Electron. **24**, 398 (1988).
3. L. Li and J. Hirsh, Opt. Lett. **20**, 1349 (1995).
4. B. W. Shore *et al*., J. Opt. Soc. Am. A **14**, 1124 (1997).
5. K. Hehl *et al*., Appl. Opt. **38**, 6257 (1999).
6. B. Touzet and J. R. Gilchrist, Photonics Spectra **37**, 68 (2003).
7. T. Zhang, M. Yonemura, and Y. Kato, Opt. Commun. **145**, 367 (1998).
8. C. Pizarro *et al*., Appl. Opt. **41**, 4562 (2002).
9. T. J. Kessler, J. Bunkenburg, and H. Huang, "Grating Array Systems for the Alignment and Control of the Spatial and Temporal Characteristics of Light," U.S. Patent Application (filed May 2003).
10. T. J. Kessler, J. Bunkenburg, H. Huang, A. Kozlov, C. Kelly, and D. D. Meyerhofer, "The Coherent Addition of Gratings for Pulse Compression in High-Energy Laser Systems," to be published in *Inertial Fusion Sciences and Applications 2003* (Elsevier, Paris, 2004).

Polar Direct Drive on the National Ignition Facility

Introduction

Recent advances in direct-drive target design have enhanced target performance beyond that achieved in the original baseline ignition design.[1] This substantially increases the probability of achieving moderate to high direct-drive target gain on the National Ignition Facility (NIF). The baseline direct-drive design for the NIF is itself very attractive. It achieves a target gain of 30 (70% of the 1-D gain) in 2-D simulations that include all expected sources of laser and target nonuniformity.[1] New developments have significantly enhanced direct-drive designs in three main areas (Fig. 96.7): (1) The fraction of laser light absorbed has been increased by almost 50% through the use of wetted-foam targets, providing increased energy coupling to the target.[2] This is the result of the higher-Z material in the foam (e.g., carbon), which makes the plasma more collisional. (2) The hydrodynamic stability of the target has been significantly improved by adiabat shaping, which reduces the growth of target nonuniformities induced by the Rayleigh–Taylor instability without sacrificing target gain.[3] (3) Techniques using pulse shaping[4] and radiation preheat[5] have been developed to reduce the imprint of laser nonuniformities below that amount achieved by laser-beam smoothing alone. These enhancements allow the target to be driven to higher gain while improving hydrodynamic stability. Motivated by the enhanced performance predicted for direct-drive-ignition experiments on the NIF, this article examines the feasibility of employing direct drive, while the NIF is in the x-ray-drive configuration, as an additional approach to achieving ignition or near-ignition conditions. Polar direct drive (PDD) will couple more energy to the fuel than x-ray drive, and the compressed fuel core can be more easily accessed for high-ρR diagnostic development and fast-ignitor studies.

In the x-ray-drive configuration, the beams are clustered in the polar regions of the target chamber. To achieve the most-uniform target irradiation for direct drive, PDD repoints some of these beams toward the equator of the target (see **Beam-Pointing Strategy**, p. 213). Since these "equatorial" beams are more obliquely incident on the target than the remaining beams, they will have lower laser absorption and drive the target less efficiently. To compensate for the difference in polar and equatorial coupling, the laser intensity near the equator is increased relative to the pole, and different pulse shapes are employed to accommodate time-dependent variations in drive and absorption. The level of drive uniformity achieved by this technique is being studied using the 2-D hydrocode *DRACO*[6] (see **Two-Dimensional Simulation Results**, p. 215).

The target design used in these simulations employed both adiabat shaping and wetted foam (Fig. 96.7). Adiabat shaping is accomplished by means of an intensity picket imposed at the onset of laser irradiation. Because of its short duration, the shock launched by the picket is not fully supported, and it decays as it propagates through the target. This places the outer portion of the target shell, where the shock is strongest, on a high adiabat, and the inner portion of the shell, where the shock has weakened, on a low adiabat (adiabat is the ratio of the electron pressure to the Fermi-degenerate pressure). With proper choice of the picket intensity and duration, the high-adiabat region will be primarily confined to the ablation region of the target, leaving the main portion of the fuel on a low

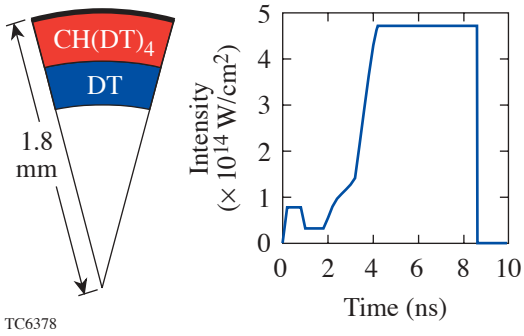

Figure 96.7
Advanced direct-drive target designs employ wetted-foam targets for increased laser absorption and a picket at the beginning of the laser pulse to provide increased hydrodynamic stability. This target and pulse shape were used for the PDD simulations.

adiabat. The higher ablator adiabat produces higher ablation velocities and enhanced ablative stabilization of the Rayleigh–Taylor instability.[3] The lower adiabat of the main fuel layer allows greater compressibility of the fuel. The picket also reduces the amount of imprint on the target surface from laser nonuniformities.[4] Picket-fence pulses have been used previously as an alternative to continuous pulse shapes.[7] The picket used here has been specifically optimized for the purpose of shaping the adiabat in the fuel.

A comparison between the performance of wetted-foam designs with adiabat shaping and the performance of the baseline "all-DT" design was discussed in Ref. 2. The primary result was that wetted-foam designs achieved target gains typically two to three times higher than the gain for the all-DT target. The higher gain was the result of two factors: increased absorption and adiabat shaping. (1) Increased absorbed energy allowed more-massive targets to be driven with the same incident laser energy. (2) Adiabat shaping allowed the main portion of the fuel to be driven on a lower adiabat without compromising the shell integrity, resulting in higher areal density (ρR). The stability of the wetted-foam target during the acceleration phase of the implosion was examined with 2-D simulations that calculated linear growth factors for different modes of nonuniformity.[8] The largest growth factor was 6.5 *e* foldings for a spherical-harmonic mode of 60, which is comparable to the stability obtained for the baseline x-ray-driven targets.[9]

It is not expected that polar-direct-drive targets will perform as well as "standard" direct-drive designs. In addition to the reduced laser coupling and the reduced hydrodynamic efficiency expected from the more-oblique irradiation near the equator of the target, there will be increased laser nonuniformity because the irradiation configuration has not been optimized for direct drive. For standard direct drive, the optimal irradiation distribution on target is known *a priori*; it must be uniform. For PDD, the irradiation pattern must be made intentionally nonuniform to compensate for the variations in target drive caused by variations in the laser angles of incidence around the target. As a result, PDD is a far more difficult design problem than standard direct drive. The required laser nonuniformity must be determined from computer simulations and confirmed by experiment.

Beam-Pointing Strategy

One possible irradiation strategy for PDD is to point the beams to the direct-drive positions on target, which are located along three latitudes at 23.5°, 44.5°, and 77.5° and corresponding latitudes in the southern hemisphere.[10] (Here, the term *NIF beams* refers to the cluster of four beams that make up a "quad"; the term *ring of beams* refers to those beams that are pointed toward a particular latitude ring on the target and not to a ring of beam ports.) This beam pointing is illustrated in Fig. 96.8: The NIF x-ray-drive beam ports are shown as open circles, and arrows show the places on the initial target surface where each of the corresponding beams is pointed. When the NIF is converted to direct drive, the 30° beams will be relocated to the 77.5° ports (together with the 50° beams). For PDD, rather than pointing the 30° beams directly to the equatorial ring, a two-step procedure was used in order to minimize the angles of incidence near the equator. The four beams at 30° were pointed to direct-drive positions at 44.5°, and four of the eight beams that were already pointed to those positions were directed toward the 77.5° ring near the equator.

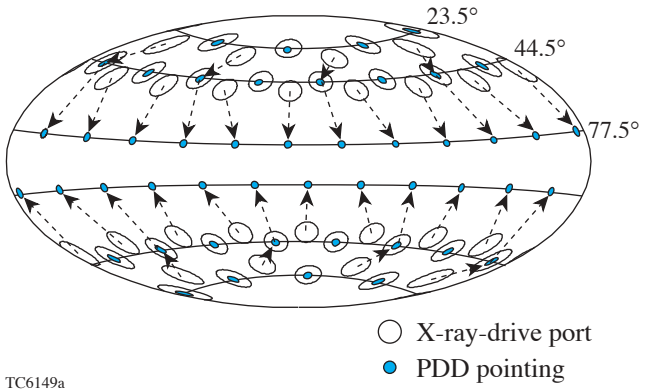

Figure 96.8
PDD repoints some beams from the NIF's x-ray-drive ports toward the target equator. This figure shows the beams being directed to the direct-drive positions corresponding to three rings of beams incident upon the target in each hemisphere.

Simply pointing the beams to the direct-drive positions does not, however, necessarily produce the optimal results for target drive uniformity. There are two main reasons: (1) Since the beam axes are not radially directed, their positions on the target surface will change as the target implodes; optimal uniformity at one time during the implosion may not be optimal at a later time. (2) The distribution of incident beam angles on target is not the same for the polar and equatorial regions; as a result, there will be variations in target drive due to spatial variations in laser absorption and in the density, where absorption occurs.

An example of the different angular distributions of incident rays is shown in Fig. 96.9 for two polar angles: 20° (characteristic of the polar region) and 90°. The normalized distribution of laser energy is plotted as a function of incident ray angle. This represents the simple projection of rays from the x-ray-drive ports onto a sphere, which is the initial size of the target. Each of the distributions has been averaged over all azimuthal angles and ±10° in the polar angle. The width of the distribution is the result of contributions from overlapping beams as well as the averaging. The distribution in the polar region is heavily weighted toward angles below 40° and is typical of the distribution around the target when beams originate from the direct-drive ports. The distribution of rays in the equatorial region is dominated by angles greater than 40°.

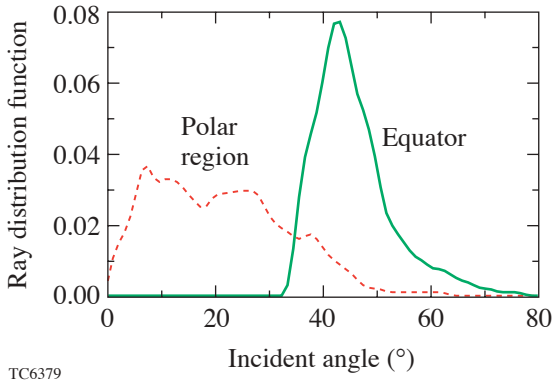

Figure 96.9
The distribution of incident angles for the laser rays is calculated by projecting the beams from the NIF's x-ray-drive ports onto a sphere, using the beam pointing of Fig. 96.8. The distributions have been averaged over all azimuthal angles and ±10° in polar angle.

An indication of the variation in electron densities where the energy would be deposited is given by the turning points of the rays during refraction. Using a planar approximation, the electron density n_e at the turning point of the rays is $n_e = n_c \cos^2\theta$, where n_c is the critical density and θ is the incident angle of the rays. Thus, energy in the polar region is deposited typically above $0.6\,n_c$, and energy near the equator is deposited well below $0.6\,n_c$.

To improve the pointing strategy, absorption physics was added to the analysis. We used a target design (described in the following section) driven by uniform irradiation to obtain the density and temperature profiles at a time near peak laser irradiation. Rays were then tracked from the NIF x-ray-drive ports through the plasma atmosphere to calculate absorption as a function of the incident angle. The relative energy among the beams, the beam pointing, and the beam-spot shapes were varied to find the configuration that gave the lowest rms variation in absorption around the target. Optimal uniformity was found by pointing the beams to latitudes that were closer to the equator than the direct-drive positions in Fig. 96.8, namely 26°, 59°, and 82°. Elliptical spot shapes were used, with the ratio of major to minor axes being 1.0, 1.25, and 1.8, respectively.

Further optimization of the irradiation strategy must take into consideration the differences in hydrodynamic efficiency that result from variations around the target in density where the laser light is absorbed; time-dependent effects resulting from the target implosion and plasma evolution; and multidimensional effects such as lateral heat flow arising from temperature variations in the laser deposition region. The 2-D simulations include all these effects and were used as guidance on how to further improve the uniformity of target drive through the use of beam pointing, laser-focal-spot shapes, and pulse shapes.

One-Dimensional Target Design Considerations

One-dimensional simulations are useful to obtain insight into the sensitivity of target drive to the distribution of incident laser rays. They were used here to obtain a first estimate of the spatial variations in laser intensity that are required to compensate for the variations in incident laser light around the target. The results also identified a realistic target design for the 2-D simulations. These estimates neglect the effect of lateral mass and heat transport, which are included in the full 2-D simulation described in the next section.

A series of 1-D simulations were performed, each corresponding to a different latitude on the target. The distributions of incident laser rays for the different latitudes were estimated as done for Fig. 96.9. In each simulation, the target was uniformly irradiated with the distribution of rays corresponding to a particular latitude. The rays were traced in the spherical plasma profiles, but because of the spherical symmetry of the problem, only the radial location of the ray entered. The goal was to find a pulse shape corresponding to each latitude such that the resulting shock positions and shell positions were similar to those for the 20° latitude, within a few microns.

We used the $CH(DT)_4$, 1.5-MJ design (1.35 MJ absorbed) from Ref. 1 as the starting point. The design was further optimized for a target driven with the distribution of incident laser rays characteristic of the 20° latitude. This became the

baseline for determining pulse shapes at other latitudes. The 1-D simulations showed very little variation in the required pulse shapes for latitudes between 0° and 60°. However, to obtain similar target drive with the equatorial distribution of rays, the energy in the beams had to be increased by about 30%.

These 1-D estimates indicated that a 1.1-MJ target design should be used in the 2-D simulations: this should provide enough "headroom" to increase beam energies by 30% to 50%, if necessary, to compensate for the oblique irradiation near the equator. (This assumes a 1.6-MJ capability for the NIF.) The target and pulse shape were similar to the $CH(DT)_4$ design from Ref. 1, but they were scaled down for the incident energy of 1.1 MJ (see Fig. 96.7). The 1-D results were target gain = 54; absorbed energy = 1.0 MJ; peak implosion velocity = 4.1×10^7 cm/s; and peak $\rho R = 1.2$ g/cm^2. A stability analysis, using a postprocessor[11] to the 1-D code *LILAC*, showed that the mix region was only about 30% of the shell thickness during the acceleration phase of the implosion for this target.

This design was used as a baseline for the 2-D hydrodynamic simulations (see next section). In the 2-D simulations, the pulse shapes for the different rings of beams were adjusted to produce similar shock and shell conditions as achieved in the 1-D baseline simulation. Besides compensating for the reduced laser coupling at the equator, the pulse shapes had to compensate also for the lateral flow of deposited energy from the equator toward the pole. The 1-D estimates showed that coronal electron temperatures should be higher at the equator than in the nearby mid-latitude regions, due to the higher laser intensity required to drive that part of the target. This will result in lateral heat flow in the 2-D simulations.

Two-Dimensional Simulation Results

For the 2-D *DRACO* simulations, the NIF irradiation configuration was described in terms of the beams pointed to three latitude rings in each hemisphere, as shown in Fig. 96.8. The simulations discussed below used the latitudes 26°, 59°, and 82° relative to the initial radius of the target (see **Beam-Pointing Strategy**, p. 213). A ray-trace algorithm with refraction calculated the amount of laser absorption and the location of the deposited energy in the plasma atmosphere around the target. An azimuthal average of the deposition was used. Whereas a full three-dimensional ray-trace algorithm has been developed for PDD simulations in the Eulerian code *SAGE*,[12] an approximate treatment was implemented here for speed during optimization studies. The approximation used only the radial variation in the index of refraction to modify the ray trajectories and ignored lateral variations. An azimuthal average of the laser deposition determined how energy for each ring was distributed on the target. These simulations addressed only the gross nonuniformities in target drive that arise from beam placement and pointing. The effects of target-surface nonuniformities and beam nonuniformities will be examined in future work.

As the target implodes, the energy delivered to the equator changes relative to the pole because the beams are not pointed toward the target center. To compensate for the time-dependent effects, as well as 2-D effects resulting from lateral heat flow, different pulse shapes were used for the three rings of beams. A numerical algorithm was developed to automatically adjust pulse shapes during the simulation to compensate for nonuniform drive. Different tests were used to detect nonuniformities: During the time of shock propagation, variation in the mass-weighted, inward-moving velocity was used. After the time of shock breakout and during acceleration, variation in the outer position of the target shell (as defined by the location of the point at $1/e$ times peak density) was used. The pulse-shape-refinement algorithm adjusted the relative power among the pulses to increase laser deposition in regions where the target was moving too slowly and to decrease deposition in regions that were moving too rapidly. In practice the required variation in laser absorption around the target could be achieved only for long-wavelength nonuniformities because control is limited to only three degrees of freedom corresponding to the three rings of beams.

To adjust the pulse shape in each ring of beams, we calculated the energy deposition pattern for each ring separately on the target. The relative power in each ring was varied until the superposition of all the deposition patterns formed a best fit to the variation required to compensate for drive nonuniformities.

A technique known as proportional–integral–differential (PID) feedback, common in control theory,[13] was used to adjust the pulse shape for each ring of beams on the target. The source of the feedback was the spatial perturbation formed by sampling the nonuniformity during a *DRACO* simulation and then applying the proportional, integral, and differential feedback gain terms. The integral and differential terms act to dampen and stiffen the response function. A simple prescription to find the feedback gain terms can be found in Ref. 14. The Levenberg–Marquardt nonlinear optimization algorithm[15] was employed to find the optimal choice for the relative strengths among the rings of beams such that the combined absorption variation provides a best fit to the feedback perturbation. Spherical-harmonic modal space was used in lieu of physical

space in the algorithm because the Levenberg–Marquardt algorithm allows for the optimization of a predetermined set of modes. For instance, certain modes considered the most dangerous can be given a larger weight during optimization. Note that in the limit of zero feedback gain, the optimization procedure reduces to a minimization of the rms variation of absorbed energy.

The pulse-shape refinement algorithm was not able to respond adequately to nonuniformities that were highly localized around the equator. To compensate for the reduced energy deposition at the equator from the very oblique incident irradiation, it is necessary to substantially increase the relative amount of energy deposited in that region by the equatorial ring of beams. However, if the spot shape were made sufficiently elliptical to localize the energy to the equatorial region, its contribution to uniformity through beam overlap in the mid-latitudes would be reduced. The problem was addressed by using a beam profile that was parameterized as the superposition of two super-Gaussian profiles (illustrated in Fig. 96.10). The main part of the spot shape is a super-Gaussian profile that contributes to beam overlap in the mid-latitudes as well as the equator. Superimposed on this is a highly elliptical super-Gaussian profile that concentrates additional energy only in the equatorial region. The aspect ratio of the ellipse, its relative location, and its relative energy are adjustable parameters that were varied in a series of 2-D simulations to find the optimal drive uniformity. In the simulations below, the ratio of major to minor axes was 5; the center of the superimposed ellipse was offset from the main spot by 10% of the target radius in the direction of the equator; and its peak intensity was 20% of the peak intensity for the main spot. The shape of the main part of the beam was also varied, and a 1.8:1 ellipse was used in the simulations below.

The three pulse shapes generated by the pulse-shape refinement algorithm resulted in the intensity variations shown in Fig. 96.11(a) for the pole and equator. The intensity variation for all polar angles is shown in Fig. 96.11(b) for the times 4.2 ns and 8 ns. At 4.2 ns, the intensity variation is relatively flat, increasing by about 30% only near the equator. This is consistent with the 1-D estimates. At 8 ns, there is a dip in the incident intensity at 45°, followed by a factor-of-2 increase at the equator. This is a 2-D effect. The temperature at the equator becomes larger than in the mid-latitudes due to the increased intensity required to drive that portion of the target. Lateral heat flow moves some of the energy deposited at the equator toward the 45° latitude. Consequently, less laser light needs to be deposited at 45° to obtain the required target drive at that location, but more energy must be deposited at the equator.

The resulting drive uniformity was adequate to achieve a high value of fuel ρR during the implosion, but further improvements in uniformity are required to actually reach ignition. The PDD simulation tracked the corresponding 1-D result up to the onset of hot-spot formation. A comparison between the PDD angularly averaged density profile and the 1-D profile at the end of the acceleration phase of the implosion is shown in Fig. 96.12. At this time, the shell radius has converged by almost a factor of 4. The positions and magnitudes of the peaks are very similar; however, there were density variations of ±20%, pressure variations of ±10%, and a variation in the outer surface of the shell of ±5%. These nonuniformities continued to grow during the deceleration phase of the implosion.

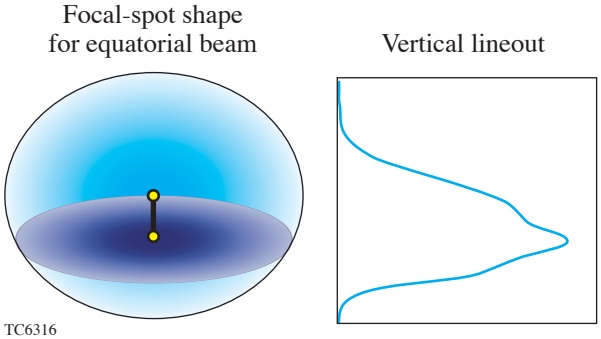

Figure 96.10
The spot shape for the equatorial ring of beams is chosen as the superposition of two super-Gaussian profiles. The larger profile contributes to irradiation uniformity at the mid-latitude regions, as well as near the equator. The highly elliptical profile concentrates additional energy very close to the equator.

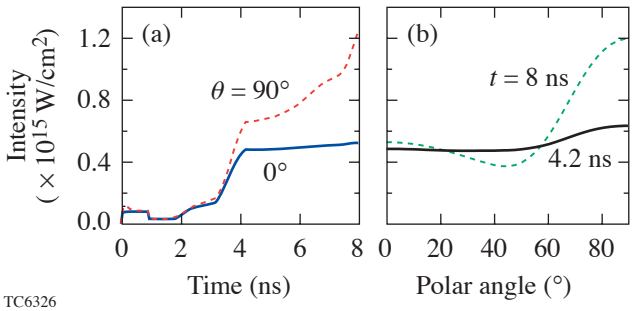

Figure 96.11
The variation in intensities at the pole and equator shows the compensation required for PDD: (a) the temporal variation in intensity at the pole and equator; (b) the angular variation in intensity at times 4.2 and 8.0 ns.

Near the time of hot-spot formation, when the shell had converged an additional factor of 6, the target nonuniformities had grown sufficiently large that the resultant shell distortion prevented further development toward ignition. A density contour plot at this time in the simulation is shown in Fig. 96.13, together with the temperature contours for 10, 8, 6, and 4 keV in the hot-spot region. High-density spikes are starting to penetrate into the hot region. In Fig. 96.14, the angular average of both the temperature and density is compared with 1-D profiles as a function of ρR. The temperature profiles are similar, with the hot region extending to a ρR of ~0.1 g/cm^2. Over the next 100 to 200 ps, the 1-D simulation extends the hot region to a ρR of 0.2 to 0.3 g/cm^2 and ignition occurs. The 2-D simulation failed to continue forming the hot spot beyond this point due to extensive growth of shell distortion. In Fig. 96.14, the contribution of shell distortion is evident in the width of the angularly averaged density profile.

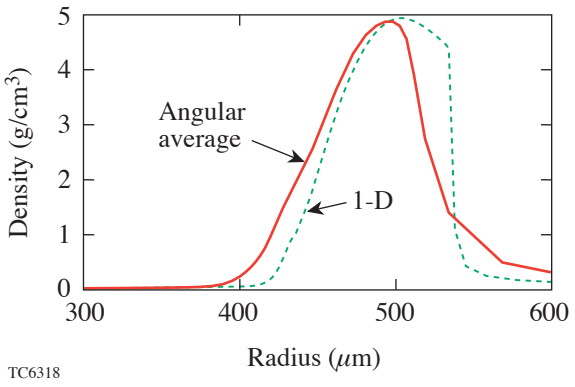

Figure 96.12
The angular average of the density profile from the PDD simulation is compared with the corresponding 1-D density profile at the end of the acceleration phase of the implosion (8.2 ns).

Even though ignition did not occur in this simulation, the conditions achieved during the time of neutron production could be very useful for the development of high-ρR diagnostics and the investigation of fast-ignitor physics.[16] The neutron-averaged ρR was 1.1 g/cm^2, and the neutron yield was 6×10^{16} (corresponding to a target gain of 0.1).

Strategies to improve the uniformity of target drive for PDD are being developed. The automated pulse-shape refinement algorithm is being further optimized to better detect drive nonuniformity and adjust pulse shapes accordingly. For a given set of beam-pointing and spot-shape conditions, it may not be possible to achieve adequate drive uniformity by adjusting the pulse shapes. Thus, the specifications for beam pointing and spot shapes are also being refined. Target "shimming," in which the target shell is made thinner at the equator than at the pole, is another technique that will be examined for improving drive uniformity. Conditions very close to ignition have been achieved here. An additional factor-of-2 improvement in drive uniformity will probably be adequate for the target to ignite.

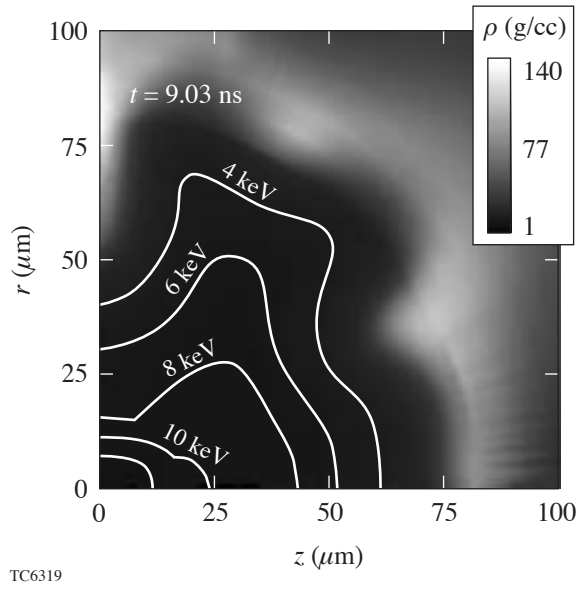

Figure 96.13
Density contour plot at the onset of hot-spot formation (9.03 ns) shows spikes starting to penetrate the hot region. Temperature contours of 10, 8, 6, and 4 keV are shown.

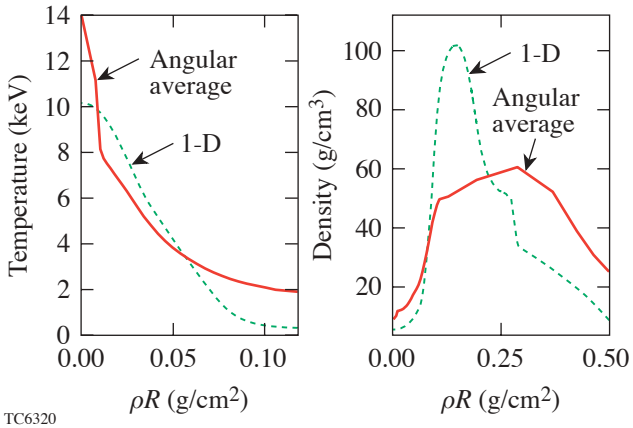

Figure 96.14
The angular averages of temperature and density profiles from the PDD simulation near the onset of hot-spot formation (9.03 ns) are compared with the 1-D results.

The computer simulations used to identify optimal irradiation strategies will be validated by experiments on the OMEGA laser.

PDD Experiments on OMEGA

Three sets of experiments planned for the OMEGA laser over the coming year are designed to validate the computer modeling of target performance driven by oblique irradiation. One set of experiments will investigate shock propagation in planar geometry using cryogenic D_2 and wetted-foam targets. The OMEGA beam geometry can irradiate a planar target with beams at 23°, 48°, and/or 60° angles of incidence. The main diagnostic will be the measurement of the time of shock breakout at the rear of the target.

The second set of experiments will irradiate spherical targets uniformly, but with all the beams repointed to make the beam axes equally oblique to the target surface. The symmetry of the OMEGA irradiation geometry can be maintained by repointing all beams by the same amount. This can be achieved as shown in Fig. 96.15: The beams of the OMEGA laser are configured as 12 pentagonal groups. The angle of incidence of each beam axis on the initial target surface can be changed from normal to 24.8° by pointing each beam to a place on the target that corresponds to the position of a neighboring beam in the pentagon. This tests the modeling of laser absorption and target drive with oblique irradiation, without introducing the complication of large variations in irradiation conditions around the target.

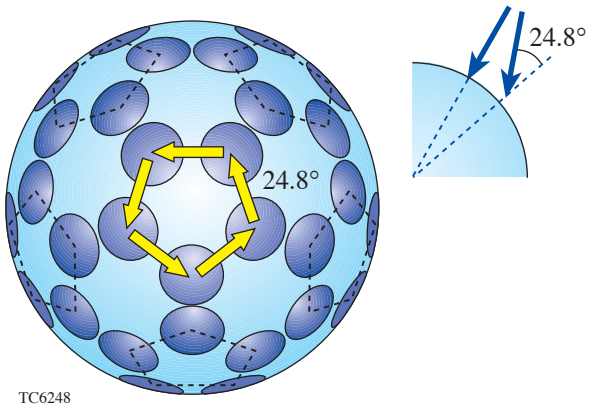

Figure 96.15
One of the PDD experiments planned for the OMEGA laser will repoint all beams by the same amount to maintain irradiation uniformity while driving an implosion with oblique irradiation.

The third set of experiments will be a more direct characterization of PDD on the NIF. In this case, 40 of the 60 OMEGA beams will be used to populate only the beam ports near the polar regions, providing a good approximation to the polar-direct-drive conditions that will occur on the NIF. The beams will then be repointed, and the pulse shapes adjusted (within the limitations of OMEGA), to drive spherical implosions. These will be compared with 2-D simulations.

Summary

The recent progress in direct-drive target design makes the direct-drive approach to inertial confinement fusion a very attractive candidate for achieving high gain on the NIF. Adiabat shaping is a very powerful technique to enhance target stability. When combined with the increased laser absorption possible in wetted-foam targets, 1-D target gains of the order of 80 are possible.

Direct-drive target physics can be examined while the NIF is in the x-ray-drive configuration by pointing some of the beams toward the target equator. This polar-direct-drive approach presents more-difficult design problems than standard direct drive, which uses a beam configuration already optimized for the required level of irradiation uniformity. For PDD, the incident irradiation must be made intentionally nonuniform—higher in the equatorial region than in the polar region—to accurately compensate for the spatial variations in laser absorption and hydrodynamic efficiency. Simulations have not yet demonstrated ignition with PDD, and the optimization process is still in progress. Nevertheless, high values of ρR and high neutron yield have been obtained in the simulations, suggesting that, at the very least, PDD can be an attractive technique for high-ρR diagnostic development and fast-ignitor experiments. PDD might be the best approach for fast-ignitor experiments while the NIF is in the x-ray-drive configuration because of the relatively large amount of energy that can be coupled to the fuel and because the ignitor beams can access the compressed core without passing through a hohlraum.

ACKNOWLEDGMENT

This work was supported by the U.S. Department of Energy Office of Inertial Confinement Fusion under Cooperative Agreement No. DE-FC03-92SF19460 and the University of Rochester. The support of DOE does not constitute an endorsement by DOE of the views expressed in this article.

REFERENCES

1. P. W. McKenty, V. N. Goncharov, R. P. J. Town, S. Skupsky, R. Betti, and R. L. McCrory, Phys. Plasmas **8**, 2315 (2001).

2. S. Skupsky, R. Betti, T. J. B. Collins, V. N. Goncharov, D. R. Harding, R. L. McCrory, P. W. McKenty, D. D. Meyerhofer, and R. P. J. Town, in *Inertial Fusion Sciences and Applications 2001*, edited by K. Tanaka, D. D. Meyerhofer, and J. Meyer-ter-Vehn (Elsevier, Paris, 2002), pp. 240–245.

3. V. N. Goncharov, J. P. Knauer, P. W. McKenty, P. B. Radha, T. C. Sangster, S. Skupsky, R. Betti, R. L. McCrory, and D. D. Meyerhofer, Phys. Plasmas **10**, 1906 (2003).

4. T. J. B. Collins and S. Skupsky, Phys. Plasmas **9**, 275 (2002).

5. S. P. Obenschain *et al*., Phys. Plasmas **9**, 2234 (2002).

6. A short description of the hydrocode *DRACO* is contained in P. B. Radha, V. N. Goncharov, T. J. B. Collins, J. A. Delettrez, P. W. McKenty, and R. P. J. Town, "Two-Dimensional Simulations of Plastic-Shell Implosions on the OMEGA Laser," to be submitted to Physics of Plasmas.

7. J. D. Lindl and W. C. Mead, Phys. Rev. Lett. **34**, 1273 (1975).

8. T. J. B. Collins, S. Skupsky, V. N. Goncharov, R. Betti, P. W. McKenty, P. B. Radha, R. Epstein, A. Poludnenko, A. Frank, and S. Mitran, "High-Gain, Direct-Drive Foam Target Designs for the National Ignition Facility," to be published in *Inertial Fusion Sciences and Applications 2003* (Elsevier, Paris, 2004).

9. M. C. Herrmann, M. Tabak, and J. D. Lindl, Phys. Plasmas **8**, 2296 (2001).

10. S. M. Pollaine and S. W. Haan, *ICF Quarterly Report* **8**, 15, Lawrence Livermore National Laboratory, Livermore, CA, UCRL-LR-105821-98-1 (1997).

11. V. N. Goncharov, P. McKenty, S. Skupsky, R. Betti, R. L. McCrory, and C. Cherfils-Clérouin, Phys. Plasmas **7**, 5118 (2000).

12. R. S. Craxton, Bull. Am. Phys. Soc. **48**, 56 (2003).

13. W. S. Levine, *The Control Handbook* (CRC Press, Boca Raton, FL, 1996).

14. See Ziegler–Nichols tuning rules, in K. Ogata, *Modern Control Engineering*, 3rd ed. (Prentice-Hall, New Jersey, 1997), Chap. 10, pp. 672–674.

15. W. H. Press, *Numerical Recipes in C: The Art of Scientific Computing* (Cambridge University Press, Cambridge, England, 1988), pp. 540–547.

16. M. Tabak *et al*., Phys. Plasmas **1**, 1626 (1994).

Properties of Fluid Deuterium Under Double-Shock Compression to Several Megabars

The equation of state of hydrogen at pressures of a few megabars, temperatures of a few electron volts, and compressions of up to several times liquid density has been a source of ongoing experimental[1–4] and theoretical[5–11] controversy. Understanding the properties of hydrogen under such conditions is fundamental to the modeling of massive planets, brown dwarfs,[12] and inertial confinement fusion. At present, access to these dense, high-pressure states can be achieved only by using shock waves; Hugoniot measurements are thus the primary tool for constraining dense-hydrogen equation-of-state (EOS) models.

Determining the density of a shocked material with a compressibility as large as hydrogen requires high-precision measurements of the primary observables. This is because fractional errors in the inferred compression ratio ρ/ρ_0 are $\rho/\rho_0 - 1$ times greater than fractional errors in the observables U_s (shock speed) and U_p (particle speed). Making a measurement precise enough to discriminate between the various deuterium EOS models thus presents a significant experimental challenge.

The first experiments to study shocked deuterium above 0.2 Mbar on the principal (i.e., single-shock) Hugoniot used laser-driven shock waves and a new, absolute measurement technique—results showed five- to sixfold compression between 1 and 2 Mbar.[1] This was in general agreement with the linear-mixing model of Ross[7] but was in significant disagreement with the original *SESAME* model developed by Kerley.[5] Subsequent experiments using magnetically driven flyer plates and a relative measurement of U_p based on aluminum impedance matching, found slightly over fourfold compression at 0.4 Mbar, which decreased to fourfold compression at 0.7 Mbar and 1 Mbar.[3] These data were consistent with a new *SESAME* model developed by Kerley[8] (which, for clarity, we refer to as the Kerley98 model) and *ab initio* models[10,11] but exhibit slightly higher compressibility than the original *SESAME*[5] and significantly lower compressibility than the Ross model. Although the pressure range of these two experiments overlapped only slightly, a clear discrepancy emerged near 1 Mbar. This discrepancy may indicate a lack of understanding of the fundamental processes in hydrogen. ICF target designs can readily accommodate these differences because they occur at relatively low pressures encountered early in the implosion. Astrophysical models, however, depend greatly on the precise details of EOS models to extrapolate conditions of large planetary bodies. This small difference can have huge effects.

The first experiment to study deuterium under double-shock conditions at megabar pressures was performed by Mostovych *et al.*,[2] who used shocks reflected from an aluminum anvil. They recognized that the expected differences between EOS model predictions for the experimental observables are greater in a reflected-shock measurement than in a single-shock measurement. Reflected shocks thus provide a more-sensitive experimental platform for discriminating between the various models; they do, however, probe not only the principal Hugoniot but also the re-shock Hugoniots and thus are a complementary, rather than an equivalent, probe of the equation of state. The data of Mostovych *et al.*,[2] taken up to single-shock pressures of 1.3 Mbar, had significant uncertainties, with error bars on a single point spanning the difference between the various models; on average, however, results agreed with the more-compressible linear-mixing model of Ross.

In this study we examine the behavior of fluid deuterium shocked initially to 0.7 to 2.5 Mbar and then double shocked to 2.5 to 9 Mbar. We cover a wider range of pressures than Mostovych *et al.*[2] and significantly improve upon the precision of those experiments by using α-quartz—a transparent re-shock anvil material—rather than aluminum. This allows us to use a high-precision, line-imaging optical interferometer to record the shock-front velocity continuously as it transits the deuterium–quartz interface. Such an approach also minimizes any systematic errors due to shock unsteadiness and nonplanarity since the measurements are localized to essentially one point in space and time. Our results are consistent with path-integral Monte Carlo (PIMC)[10] models and the Kerley98

EOS at single-shock pressures less than 1 Mbar and above 2 Mbar but deviate at intermediate pressures; the Ross model does not agree with our data over the entire range under study.

This experiment was performed on LLE's OMEGA laser, a neodymium-doped phosphate glass system that operates with frequency-tripled, 0.35-μm light.[13] To generate the shock pressures explored in these experiments, laser energies of 440 to 3100 J were delivered using a 3.7-ns-duration square pulse. The laser focal region was smoothed using distributed phase plates (DPP's), producing a uniformly irradiated 800-μm-diam spot. Targets consisted of a z-cut, α-quartz anvil mounted on the upper step of a diamond-turned aluminum pusher that was attached to a copper cell filled with cryogenic deuterium (see Fig. 96.16). A plastic ablator was used to reduce hard-x-ray generation. Three thicknesses were used for the ablator–pusher combination: 20 μm of CH on a 90- to 130-Al step (90-μm lower step and 130-μm upper step); 20 μm of CH on a 50- to 85-μm Al step, and 20 μm of CH plus 80 μm of CH-Br (plastic with 2% Br by atomic weight) on a 50- to 85-μm Al step. The quartz anvil was glued to the upper step with a glue thickness of ~1 μm and hung over the lower step as shown in Fig. 96.16. The deuterium sample explored in this experiment is trapped within the 35- to 40-μm region between the quartz anvil and the thin Al plate. By observing the solid–liquid transition in deuterium and using the well-known properties of deuterium on the saturation line,[14] we determined that the deuterium density was 0.174 g/cm^3. At this density and at the probe laser wavelength of 532 nm, the index of refraction was calculated to be 1.1381.[14] The density of the quartz was measured to be 2.65 g/cm^3. The index of refraction of quartz along its c axis at 532 nm was measured to be 1.547.

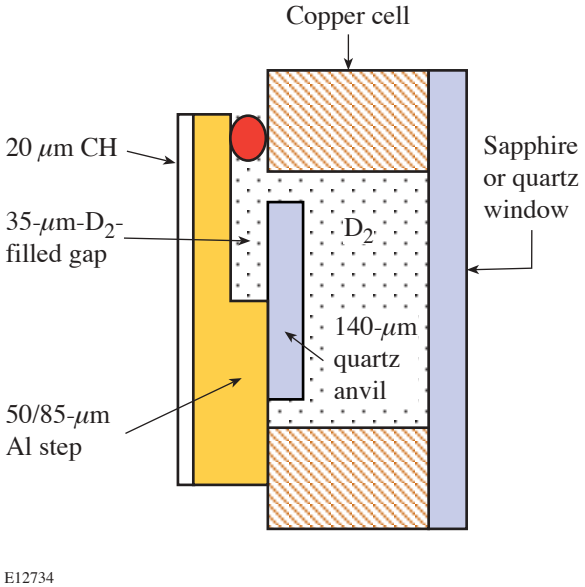

Figure 96.16
Characteristic cryogenic deuterium target design. Dimensions are for one of the three types of target.

The shock diagnostic was a line-imaging velocity interferometer system for any reflector (VISAR),[15,16] which measures the Doppler shift of a moving reflector. Two VISAR's with different velocity sensitivities were used to resolve 2π phase-shift ambiguities that occur at shock breakout from the aluminum and upon transit of the shock front from deuterium into quartz. The velocity sensitivities for the two VISAR instruments were 6.069 and 14.138 μm/ns/fringe for deuterium and 4.465 and 10.400 μm/ns/fringe for quartz. Post-processing of the VISAR images can determine the fringe position to ~5% of a fringe; since the measured shock velocities are 25 to 45 μm/ns in deuterium and 14 to 24 μm/ns in quartz, multiple fringe shifts allow the precision of the shock-velocity measurement to be ~1%. The probe source was an injection-seeded, Q-switched, yttrium–aluminum garnet laser, operating at a wavelength of 532 nm with a pulse length of ~25 ns. Streak cameras with temporal windows of ~3 ns were used to detect the reflected probe signal. The time resolution of the VISAR and streak camera system was about 40 ps.

A sample VISAR trace is shown in Fig. 96.17(a), and the resulting velocity profile inferred from the fringe positions is given in Fig. 96.17(b). The three clear events observed in these records are marked by fringe (and, hence, velocity) shifts: The first shift represents the velocity jump that occurs when the shock crosses the aluminum–deuterium interface; the second shift, at time t_x, corresponds to the drop in shock velocity as the shock moves across the deuterium–quartz interface. Shock velocities immediately before and after the shock crosses the D_2–quartz interface are the primary observables used in this work. The third shift is the jump in velocity observed in quartz when the first shock, reverberating in the compressed deuterium gap, catches the leading shock front in quartz.

To extract the velocity profile, we average the phase information at each time over a 20- to 30-μm region. To determine shock velocities at the deuterium–quartz interface, we take linear fits a few hundred picoseconds before and after t_x and extrapolate them to t_x. This eliminates ambiguities due to slight blurring of the measured velocity in a ±25-ps time window centered on t_x caused by the resolution of the VISAR and

streak camera system. Figure 96.18 plots the results in terms of the primary experimental observables: the shock speed in deuterium and quartz.

To compare these observations with EOS models it is necessary to know the high-pressure U_s–U_p relation for quartz. This relation was determined by performing extensive laser-driven shock measurements on quartz,[17] complementing data (reported in early Russian work) obtained using nuclear explosives,[18] and found that $U_s = 3.915 + 1.297\ U_p$. Taking into account the errors in the fit coefficients, this is in excellent agreement (~1%) with the relation found in the early Russian work ($U_s = 4.200 + 1.280\ U_p$)[19] over the range of pressures in our study. Our measurements were performed using impedance matching with an aluminum standard for which we utilized the experimentally derived aluminum Hugoniot relation given by $U_s\,(\text{Al}) = 6.541 + 1.158\ U_p\,(\text{Al})$;[19] because quartz and aluminum are closely impedance matched, the release was accurately calculated from the reflected Hugoniot.[20] The results change very little—and only then at the very highest pressures—if we instead use a *SESAME* EOS for aluminum.[21]

Silica is known to possess a number of polymorphic phase transitions in the solid regime below 1 Mbar.[22] Above ~1 Mbar, where silica is a fluid, quartz Hugoniot measurements have shown no indication of a subsequent structural change.[18] Our data begin at ~2.5 Mbar and closely follow a linear fit in U_s–U_p.

Using this fit and the impedance-matching conditions at the deuterium–quartz interface, we calculate the reflected shock curves for the different EOS models. These are shown in Fig. 96.18, where the uncertainty in the linear fit to the quartz Hugoniot is the thickness of the thick blue line (for clarity, the PIMC results, which are close to the Kerley98 predictions, are shown as squares). Plotting the data in terms of the experimental observables thus allows uncertainties in the quartz Hugoniot

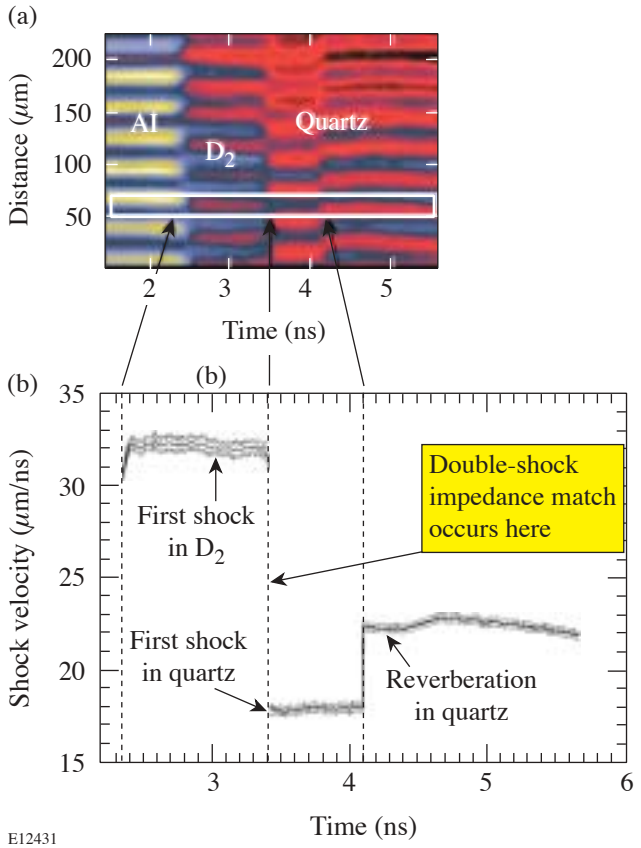

Figure 96.17
(a) Sample VISAR trace showing the signal from the reflecting shock front in deuterium and quartz. (b) Resulting velocity profile extracted from the VISAR trace in (a). Dotted lines above and below the main trace indicate the error at each time step. The shock traverses the deuterium–quartz interface at time t_x.

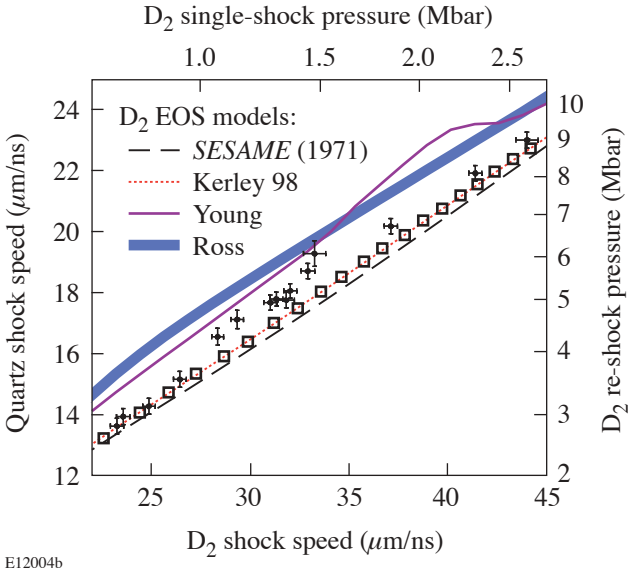

Figure 96.18
Double-shock data for fluid deuterium obtained using an α-quartz anvil (dark circles with error bars). Predictions for different equations of state are shown: *SESAME*[5] (long dashed), Kerley98[8] (red dotted), Young[9] (solid), Ross' linear-mixing model[7] (thick blue), and PIMC[10] (squares). The measured uncertainty in the quartz Hugoniot is about the thickness of the lines. The estimated D_2 single-shock and re-shock pressures on the top and right axes are based on the PIMC model for D_2 and the measured quartz Hugoniot, respectively.

to be separated from measurement errors in the deuterium re-shock experiments (which are given by the error bars on the data points). We note that the difference in expected quartz shock velocities between the softer Ross model and the stiffer Kerley98 model is close to 10% over much of the range of study. Our experimental precision of ~±1% allows us to readily discriminate between these models. The results indicate that double-shock compression of deuterium from single-shock pressures between 0.7 and 2.5 Mbar cannot be adequately described over this range by any of the models shown. Between single-shock pressures of 0.7 and 1.0 Mbar, the PIMC[10] and Kerley98[8] predictions are consistent with our data; in the regime between 1.0 and 1.3 Mbar the data approach the predictions of the Young model[9] but disagree with all models between 1.3 and 2.0 Mbar; above 2 Mbar, the results are again consistent with the stiffer PIMC and Kerley98 calculations, while at higher pressures the measurements are in agreement with the stiffer models.

A number of potential systematic effects that could compromise our data have been considered and are addressed below. The steadiness of shock-wave velocities in our experiments varied from shot to shot, depending on the laser drive, ranging from fractions of a percent to several percent over a few nanoseconds. Our new technique of determining shock velocities at essentially a single point in time using continuous measurements is not affected by such variations, unlike the transit-time measurements that were used in the earlier re-shock experiments.[2] To establish this, we performed extensive hydrodynamic simulations of our experimental arrangement using shock waves with a wide range of unsteadiness—rising and decaying. We saw no deviations from the steady shock case if the velocities were extrapolated to time t_x. This is confirmed experimentally where we observe no difference between the shots that were essentially steady and those that had several-percent unsteadiness.

Shock nonplanarity is also a potential problem, especially for an experiment that requires measurement of a breakout event at spatially separated positions. Since our measurement is performed at a localized point in space, we are not subject to such errors. Nonplanarity could affect our measurements if the wave is incident on the deuterium–quartz interface at an angle large enough to undergo significant refraction. Based on our measurement of the small curvature observed at the deuterium–quartz interface, we infer that the largest incident angles present in our experiments are 3° to target normal. The resulting change in the projected shock speed is less than 0.1% and can be neglected.

X-ray preheating of our target system is a process that would tend to make our data look less compressible. Using an etalon sensitive to motions as low as 0.1 μm/ns, we observed no expansion of the aluminum pusher prior to shock breakout. In addition, for targets shot at similar laser energies, we saw no difference in the results whether we used a 50-μm-thick or 90-μm-thick aluminum pusher. Since the attenuation length for a 1.55-keV x ray (just below the *K* edge of aluminum) is 10 μm, the extra 40 μm of Al would be expected to reduce the x-ray fluence by a factor of 50. The absence of any difference between results from these two targets indicates that x-ray preheat is negligible for these experiments.

In conclusion, we have performed the highest-precision re-shock experiments to date on deuterium shocked to initial pressures between 0.7 and 2.5 Mbar. Below 1 Mbar and above 2 Mbar, the results are in approximate agreement with predictions based on the PIMC and Kerley98 models—models that have near-fourfold compression on the principal Hugoniot—but disagree with these theories between 1 and 2 Mbar. In contrast to earlier re-shock results,[2] our higher-precision measurements are not consistent with the Ross linear-mixing model. At present, no theory adequately accounts for our observed re-shock results over the entire range under study. We emphasize that there is no model-independent way to compare re-shock measurements with principal Hugoniot measurements since second-shock pressures are affected not only by the density of the first shock but also by the sound speed (or isentropic compressibility) of the compressed states. Given that shock experiments on deuterium above 0.4 Mbar have yielded a wide range of results, the equation of state of hydrogen at megabar pressures and electron-volt temperatures remains an open question. Ultimately a variety of different experimental techniques performed over a broad region of phase space will be required before a consistent picture can emerge.

ACKNOWLEDGMENT

We thank G. I. Kerley, B. Militzer, and D. A. Young for providing model calculations and the LLE Mechanical Engineering, target fabrication, and OMEGA operations staff for their efforts during these experiments. This work was performed under the auspices of the U.S. Department of Energy by LLNL under Contract No. W-7405-ENG-48 and by the University of Rochester under Cooperative Agreement No. DE-FC03-92SF19460.

REFERENCES

1. L. B. Da Silva *et al.*, Phys. Rev. Lett. **78**, 483 (1997); G. W. Collins *et al.*, Science **281**, 1178 (1998); G. W. Collins *et al.*, Phys. Plasmas **5**, 1864 (1998).

2. A. N. Mostovych *et al.*, Phys. Rev. Lett. **85**, 3870 (2000); A. N. Mostovych *et al.*, Phys. Plasmas **8**, 2281 (2001).

3. M. D. Knudson *et al.*, Phys. Rev. Lett. **87**, 225501 (2001); M. D. Knudson *et al.*, Phys. Rev. Lett. **90**, 035505 (2003).

4. S. I. Belov *et al.*, JETP Lett. **76**, 433 (2002).

5. G. I. Kerley, Los Alamos National Laboratory, Report LA-4776 (1972); J. Chem. Phys. **73**, 469 (1980); J. Chem. Phys. **73**, 478 (1980); J. Chem. Phys. **73**, 487 (1980).

6. D. Saumon and G. Chabrier, Phys. Rev. A **46**, 2084 (1992); D. Saumon, G. Chabrier, and H. M. Van Horn, Astrophys. J., Suppl. Ser. **99**, 713 (1995).

7. M. Ross, Phys. Rev. B, Condens. Matter **58**, 669 (1998).

8. G. I. Kerley, Lawrence Livermore National Laboratory, private communication (2002). This model has also been referred to as the *SESAME* model (Ref. 3) but shows softer behavior than the original *SESAME* (Ref. 5) referred to in earlier publications (Ref. 1).

9. D. A. Young, in *Shock Compression of Condensed Matter–1999*, edited by M. D. Furnish, L. C. Chhabildas, and R. S. Hixson (American Institute of Physics, Melville, NY, 2000), pp. 53–56.

10. B. Militzer and D. M. Ceperley, Phys. Rev. Lett. **85**, 1890 (2000); B. Militzer *et al.*, Phys. Rev. Lett. **87**, 275502 (2001).

11. T. J. Lenosky *et al.*, Phys. Rev. B, Condens. Matter **61**, 1 (2000); L. A. Collins *et al.*, Phys. Rev. B, Condens. Matter **63**, 184110 (2001).

12. R. Smoluchowski, Nature **215**, 691 (1967); W. B. Hubbard, Science **214**, 145 (1981); W. B. Hubbard *et al.*, Phys. Plasmas **4**, 2011 (1997); G. Chabrier *et al.*, Astrophys. J. **391**, 817 (1992); G. Chabrier and I. Baraffe, Astron. Astrophys. **327**, 1039 (1997).

13. T. R. Boehly, D. L. Brown, R. S. Craxton, R. L. Keck, J. P. Knauer, J. H. Kelly, T. J. Kessler, S. A. Kumpan, S. J. Loucks, S. A. Letzring, F. J. Marshall, R. L. McCrory, S. F. B. Morse, W. Seka, J. M. Soures, and C. P. Verdon, Opt. Commun. **133**, 495 (1997).

14. P. C. Souers, *Hydrogen Properties for Fusion Energy* (University of California Press, Berkeley, 1986).

15. L. M. Barker and R. E. Hollenbach, J. Appl. Phys. **43**, 4669 (1972).

16. P. M. Celliers *et al.*, Appl. Phys. Lett. **73**, 1320 (1998).

17. D. G. Hicks *et al.*, "Measurements of the Equation of State of Quartz," in preparation.

18. L. V. Al'tshuler, R. F. Trunin, and G. V. Simakov, Izv. Acad. Sci. USSR Phys. Solid Earth, No. 1, 657 (1965); R. F. Trunin *et al.*, Izv. Acad. Sci. USSR Phys. Solid Earth, No. 1, 8 (1971); R. F. Trunin, Phys.-Usp. **37**, 1123 (1994).

19. R. F. Trunin, ed. *Experimental Data on Shock Compression and Adiabatic Expansion of Condensed Matter* (Russian Federal Nuclear Center–VNIIEF, Sarov, 2001).

20. R. F. Trunin, *Shock Compression of Condensed Materials* (Cambridge University Press, Cambridge, England, 1998).

21. The *SESAME* table for aluminum compared in this case was #3718, given in S. P. Lyon and J. D. Johnson, Los Alamos National Laboratory, Los Alamos, CA, Report LA-UR-92-3407 (1992). For our analysis, differences between the various *SESAME* tables for aluminum are negligible.

22. See, for example, J. A. Akins and T. J. Ahrens, Geophys. Res. Lett. **29**, 31-1 (2002) and references therein.

Independent Phase and Amplitude Control of a Laser Beam Using a Single-Phase-Only Spatial Light Modulator

Laser-beam shaping is a rapidly developing field of research driven by both technological improvements of beam-shaping devices and the ever-increasing demands of applications. In high-energy laser chains, efficient beam shaping is successfully achieved in the front ends by passive methods such as beam apodization[1] or intracavity mode shaping;[2] however, these static techniques are unable to correct dynamic laser-beam profiles caused by alignment drifts or thermal problems.

Spatial light modulators (SLM's) are versatile devices that can modulate the polarization or the phase of laser beams at high refresh rates. It has been demonstrated that a SLM can be used to compensate for the thermal phase distortion occurring in high-energy glass amplifiers.[3] Similarly, SLM's have been used in high-energy laser applications, such as intracavity beam shaping[4] or focal-spot control.[5] In all these applications, only the phase-modulation capability of the SLM was used; however, there are numerous applications where phase-only modulation can be achieved differently. For instance, deformable mirrors are more attractive when it comes to wavefront correction of a large, high-energy, laser beam. Their scale and damage threshold allow them to be used within the power amplifier, while SLM's are confined to the front end because of their modest size and low damage threshold. Nevertheless, a corrective device that would address both phase and amplitude simultaneously may be successfully used in high-energy lasers to significantly reduce the alignment procedure time, to improve the amplifier fill factor by injecting a more-adapted beam shape, to reduce the risk of damage in the laser chain by removing hot spots, and to improve the on-target characteristics of the beam by better control of the phase.

Several techniques have been proposed to produce complex modulation of an electromagnetic field with an SLM for encoding computer-generated holograms.[6,7] In both cases, two neighboring pixels with a single-dimension modulation capability are coupled to provide the two degrees of freedom required for independent phase and amplitude modulation. In our work, we use a similar approach, but our requirements differ from that of the hologram generation. First, the number of modulation points across the beam does not need to be high because spatial filtering imposes a low-pass limit on the spatial frequencies allowed in the system. Second, a high-efficiency modulation process is required to minimize passive losses. Lastly, the required amplitude-modulation accuracy should be better than measured shot-to-shot beam fluctuations for the correction to be fully beneficial.

In this article, we propose a new method to modulate both the phase and amplitude of a laser beam, with a single-phase-only SLM using a carrier spatial frequency and a spatial filter. As a result, the local intensity in the beam spatial profile is related to the amplitude of the carrier modulation, while its phase is related to the mean phase of the carrier. In the first part of this article, we show the simple relation between the transmitted intensity and the phase-modulation amplitude, and in the second part, we experimentally verify this scheme and use it to demonstrate beam shaping in a closed-loop configuration.

The principle of the modulation is depicted in Fig. 96.19 for the case of a plane wave. The SLM is used as a phase-only device that applies a one-dimensional phase grating to the electric field. As a consequence, the two-dimensional propagation integral reduces to a one-dimensional one. In such a case, the electric field transmitted—or reflected—through the modulator accumulates a phase ϕ given by

$$E' = E_0 \exp\left[j\phi(x)\right], \tag{1}$$

where E_0 can be complex and ϕ is a periodic square phase modulation, of period Λ, oscillating between the values ϕ_1 and ϕ_2. After propagation through a lens, in an *f-f* configuration and under the Fraunhofer approximation, the electromagnetic field distribution at the focus of the lens is proportional to the Fourier transform of Eq. (1). To calculate the Fourier transform of E', one can consider, for instance, the initial electromagnetic field as a sum of two square waves defined by

$$E_1 = E_0 \sum_n \delta(x - n\Lambda) \otimes \mathrm{rect}_{\Lambda/2}(x) \exp(j\phi_1), \quad (2)$$

$$E_2 = E_0 \sum_n \delta(x - n\Lambda) \otimes \mathrm{rect}_{\Lambda/2}(x - \Lambda/2) \exp(j\phi_2), \quad (3)$$

where δ is the Dirac function and $\otimes$ denotes the convolution product. After some algebra, the electromagnetic field distribution at the focus, given as the sum of the Fourier transforms of E_1 and E_2, can be written as

$$\tilde{E} \propto E_0 \sin c\left(\pi \frac{\Lambda \nu}{2}\right) \cos\left(\frac{\Delta\phi}{2} + \pi \frac{\Lambda \nu}{2}\right)$$

$$\times \exp\left[j\left(\frac{\phi_1 + \phi_2}{2} - \pi \frac{\Lambda \nu}{2}\right)\right] \sum_n \delta(\nu - n/\Lambda), \quad (4)$$

where n is the spatial frequency, and the Dirac comb function represents the diffraction pattern created by the SLM phase grating. Removing the higher-order terms $(|n| > 0)$ in this diffraction pattern with a spatial filter results in an electric field given by Eq. (5), where the amplitude is determined by the phase difference $\Delta\phi$ and the phase is equal to the average of ϕ_1 and ϕ_2:

$$\tilde{E}(0) \propto E_0 \cos\left(\frac{\Delta\phi}{2}\right) \exp\left(j \frac{\phi_1 + \phi_2}{2}\right). \quad (5)$$

This result is still true for finite beams, provided the amplitude and phase of the initial beam slowly vary with respect to the modulation frequency. If the electromagnetic field spatially varies at higher frequencies, then the imaging system will act as a spatial filter and will modify the spatial distribution of light regardless of the application of a phase modulation on the SLM.

In the experimental setup shown in Fig. 96.20, the light source is a pulsed, 300-Hz laser, the beam of which is uncollimated so that it overfills the SLM area and is linearly polarized. It is reflected off the SLM and then imaged on an 8-bit charge-coupled-device (CCD) camera (Cohu 4910 series) or to a Hartmann–Shack wavefront sensor (Wavefront Sciences CLAS-HP). The camera was used mainly for system alignment and diagnostic or whenever high-spatial-resolution beam amplitude measurement was required. The wavefront sensor was used for simultaneous phase and amplitude measurements. We use a non-pixelated, 256-level, phase-only SLM from Hamamatsu (Model X8267) with a 20 × 20-mm^2 active area, optically addressed by a 768 × 768-pixel liquid crystal display (LCD) screen. Thanks to a slight defocus of the imaging system, a continuous phase modulation can be achieved on the SLM at the expense of a slight reduction in the resolution.

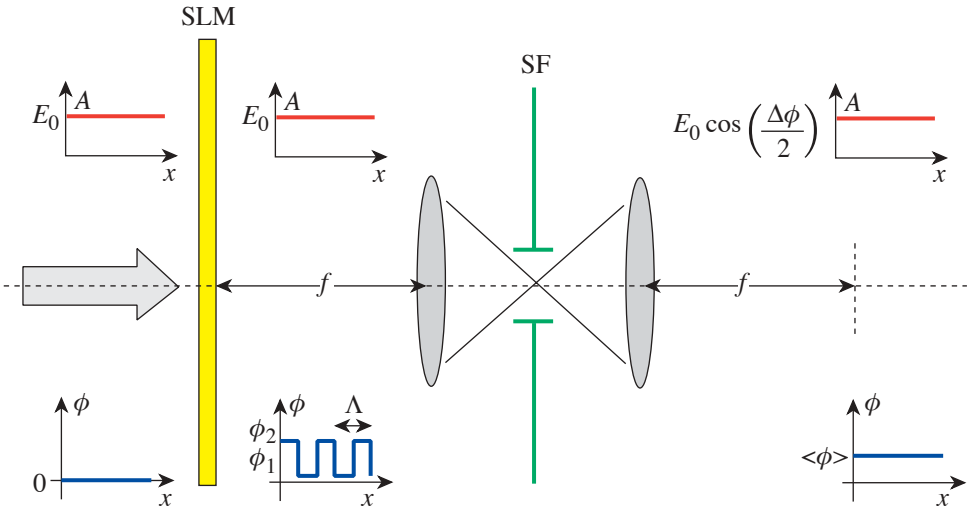

Figure 96.19
Independent phase- and amplitude-modulation scheme. The input beam is modulated in phase by the phase-only SLM and then propagates through a spatial filter (SF). The SLM is placed at a focal distance from the SF lens so the electromagnetic field distribution at the SF pinhole is proportional to the Fourier transform of the electromagnetic field distribution at the SLM location.

Although the SLM was designed for normal-incidence use, we believe that a small angle of incidence does not affect the system's performance. Only a 768 × 768 matrix is used in the imaging. The advantages of using a non-pixelated SLM are (1) its absence of loss due to the fill factor and diffraction of pixelated SLM and (2) its high damage threshold, which we tested to be 680 (±130) mJ/cm^2 with a 1-ns, 1053-nm Gaussian beam. This value is nearly two times better than that of the pixelated SLM that we tested.

To be relevant to beam shaping in a high-energy laser facility, such as the OMEGA laser, the pass band of the beam-shaping spatial filter must be at least as large as the spatial filters in the main laser power amplifier, which are as large as 30 times the diffraction limit. To ensure removal of the SLM carrier spatial frequency, the minimum spatial frequency must then be at least 30 times the fundamental spatial frequency of the beam. Practically, this means the minimum number of pixels required for that application is 60 across the beam (two per period). The beam f number in the spatial filter is 25, which means that the diffraction-limited focal spot is roughly 25 μm and the pinhole should be at least 750 μm in diameter. We used a 1-mm pinhole and a modulation frequency 64 times that of the fundamental beam frequency. In the SLM plane, this corresponds to a period of 12 pixels. For lower numbers of pixels per period, the finite slope between two nearby pixels degrades the modulation profile. For larger periods, up to 24 pixels, the beam is efficiently modulated by the SLM, but the system becomes more sensitive to the pinhole alignment.

Figure 96.21 demonstrates a linear amplitude-modulation scheme, as well as high contrast and arbitrary spatial shaping. In the upper part, Eq. (5) is inversed to obtain the phase-modulation amplitude corresponding to a linear amplitude modulation, while the lower part of the image shows nearly complete extinction for a π-rad modulation and ~100% transmission when the phase modulation is 0 rad. The low-contrast speckle, seen in Fig. 96.21, limits the achievable extinction ratio that we measured varying from 50:1 to 10:1 across the beam. It should be noted that the extinction is achieved while only half of the dynamic range of the SLM was used (128 levels), which leaves at least half of the SLM dynamic range free for phase modulation, in the worst case.

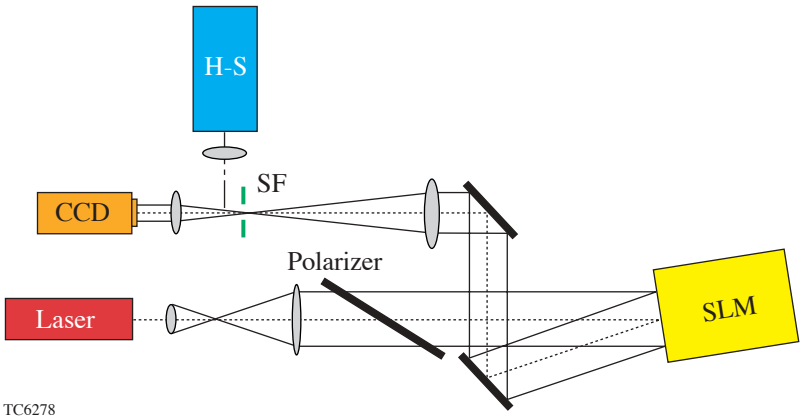

Figure 96.20
Experimental setup. SF: spatial-filter pinhole; H–S: Hartmann–Shack wavefront sensor. The SLM is used in reflection and a flip-in mirror is used to measure either the intensity or phase profiles.

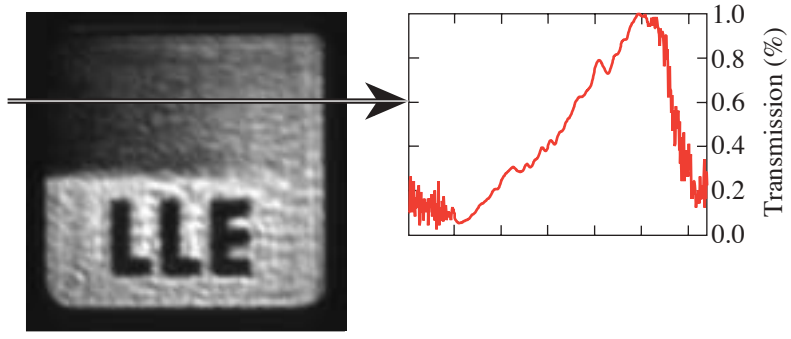

Figure 96.21
A modulated beam demonstrates the amplitude control offered by the combined SLM/spatial-filter system. The lineout in the upper portion demonstrates the effective transmission function, while the lower part demonstrates high-contrast modulation with as much as a 50:1 extinction ratio.

Figure 96.22 demonstrates simultaneous amplitude and wavefront-shaping performance of this system by summing two one-dimensional patterns with spatial frequencies below and above the cutoff frequency of the spatial filter, as shown by the mask in Fig. 96.22(a). Figure 96.22(b) shows the beam amplitude measured with the Hartmann–Shack sensor, while Fig. 96.22(c) illustrates the measured wavefront. Both images display data dropout near the center because the measured intensity falls below the detection threshold of the wavefront sensor. Little phase-to-amplitude coupling is observed, demonstrating that the phase information is conserved through the filter while the intensity modulation is achieved.

Figure 96.23 illustrates the performance of this beam-shaping scheme in an iterative, closed-loop configuration. A single convergence scheme is applied in which less amplitude modulation is applied where not enough transmission is achieved and more where too much is measured. For demonstration purposes, we propose to correct the pixels for which the measured intensity on a 8-bit gray scale is higher than 80 counts. After mapping the SLM to the CCD using a fiducial image, the required transmission at each location of the SLM and the corresponding phase-modulation amplitude are calculated. The first step correction result is shown by the image in Fig. 96.23(b) along with its corresponding lineout, which

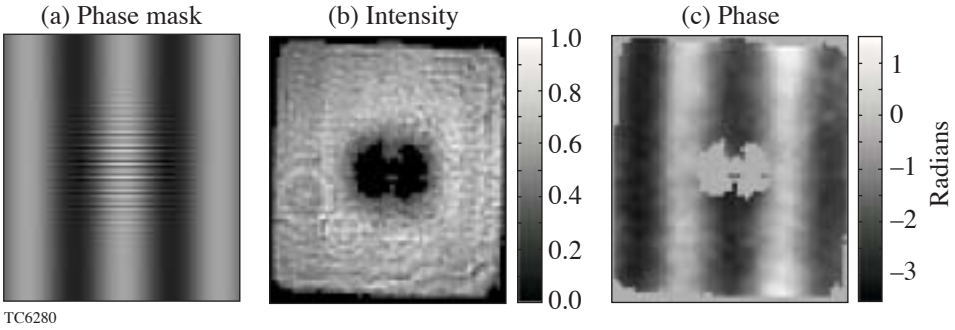

Figure 96.22
Independent phase and amplitude modulation is demonstrated. The mask (a) leads to a beam that exhibits simultaneous amplitude (b) and phase (c) modulation.

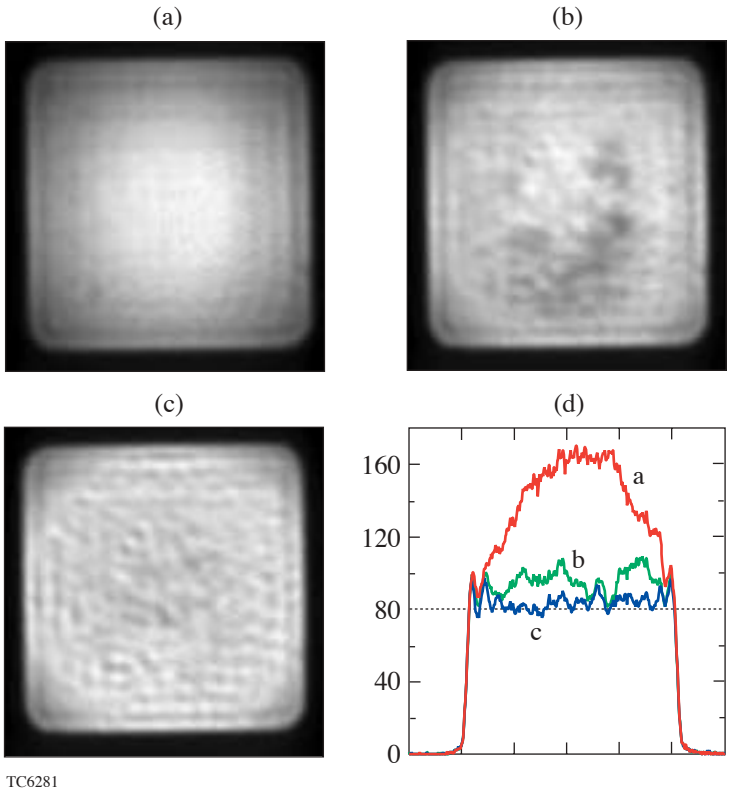

Figure 96.23
Dynamic amplitude beam control. The initial beam (a) is shaped into top-hat beams (b) and (c). The lineouts show the typical error to the intensity goal.

shows that most of the correction factor has been underestimated since the average intensity is above 80 counts. Similarly, the correction does not lead to a uniform beam because of the spatially dependent transfer function of the SLM. Nevertheless, the error, defined as the difference between the real intensity and the goal intensity, in an rms sense, for those points initially higher than 80, is reduced from 60% to 16%. Using image (b), the error signal is reduced by changing the modulation to achieve the goal. The result of a second correction is shown in Fig. 96.23(c), where the error signal has been reduced to 8.5%, which is dominated by the speckle noise discussed earlier.

We have shown a dynamic modulation scheme that addresses simultaneously both the phase and the amplitude of a laser beam. By modulating the phase of a laser beam at high spatial frequencies, one can couple the phase-modulation amplitude to the transmission of a spatial filter in a straightforward way. Following that, we have demonstrated that this scheme can be used for beam correction.

ACKNOWLEDGMENT

This work was supported by the U.S. Department of Energy Office of Inertial Confinement Fusion under Cooperative Agreement No. DE-FC03-92SF19460, the University of Rochester, and the New York State Energy Research and Development Authority. The support of DOE does not constitute an endorsement by DOE of the views expressed in this article.

REFERENCES

1. J. M. Auerbach and V. P. Karpenko, Appl. Opt. **33**, 3179 (1994).
2. V. Bagnoud, J. Luce, L. Videau, and A. Rouyer, Opt. Lett. **26**, 337 (2001).
3. B. Wattellier *et al*., in *OSA Trends in Optics and Photonics (TOPS) Vol. 56, Conference on Lasers and Electro-Optics (CLEO 2001)*, Technical Digest, Postconference Edition (Optical Society of America, Washington, DC, 2001), pp. 70–71.
4. J. Bourderionnet *et al*., Opt. Lett. **26**, 1958 (2001).
5. B. Wattellier *et al*., Opt. Lett. **27**, 213 (2002).
6. J. A. Davis, K. O. Valadéz, and D. M. Cottrell, Appl. Opt. **42**, 2003 (2003).
7. P. Birch *et al*., Opt. Lett. **26**, 920 (2001).

Proton Temporal Diagnostic for ICF Experiments on OMEGA

Introduction

In an inertial confinement fusion (ICF)[1] experiment, a capsule filled with deuterium (D_2) or a deuterium–tritium (DT) fuel is heated by either direct laser illumination or soft-x-ray radiation in a laser-heated hohlraum. The target is compressed to conditions under which thermonuclear fusion occurs. The fusion burn begins with spark ignition of the central hot spot[2] that is created by shock convergence (shock burn). A burn wave then propagates into the compressed dense fuel regions, releasing energy through fusion reactions (compressive burn).[2] Both a high-temperature hot spot and high areal density are necessary in cryogenic DT implosions to ignite the target and achieve high gain.[1–3]

Experimental information about implosion dynamics is crucial for understanding capsule fuel assembly and validating numerical simulations. Areal-density evolution measurements in cryogenic D_2 or DT implosions are complicated by the lack of simple and reliable diagnostic techniques that are available with plastic-shell targets. Therefore, many experimental studies in ICF are performed with hydrodynamically equivalent "cryogenic surrogates" such as thick plastic shells filled with D^3He or D_2 fuel. The primary fusion reactions that occur in imploding capsules fueled with D^3He gas are

$$\mathrm{D} + \mathrm{D} \rightarrow p\,(3.0\ \mathrm{MeV}) + \mathrm{T}\,(1.01\ \mathrm{MeV}), \tag{1}$$

$$\mathrm{D} + \mathrm{D} \rightarrow n\,(2.45\ \mathrm{MeV}) + {}^3\mathrm{He}\,(0.82\ \mathrm{MeV}), \tag{2}$$

and

$$\mathrm{D} + {}^3\mathrm{He} \rightarrow p\,(14.7\ \mathrm{MeV}) + \alpha\,(3.6\ \mathrm{MeV}). \tag{3}$$

From reactions (1)–(3) one can see that with D^3He both neutron diagnostics and charged-particle spectroscopy[4] can be used on OMEGA[5] to probe the plasma conditions during the shock and compressive burn phases of an implosion.

The capsule burn history is an important measure of target performance and implosion dynamics and is directly comparable with numerical models. The neutron burn history is measured on OMEGA (and previously on the Nova laser at LLNL) using the streak camera–based neutron temporal diagnostic (NTD)[6,7] with a time resolution of ~50 ps for DD neutrons and ~25 ps for DT neutrons. The neutron burn history contains valuable information about the capsule implosion close to the peak of compression. Since the neutron yield at shock convergence is about 100 times smaller than the yield at peak compression, it is difficult to measure the neutron shock signal using the NTD. On the other hand, the primary proton shock and compression yields are comparable in a typical D^3He implosion on OMEGA.[8] To use this unique feature of the D^3He fuel, a proton temporal diagnostic (PTD), based on the NTD concept, has been developed for implosion studies at OMEGA. The PTD allows us to record the proton-production history and simultaneously measure shock bang time and compression bang time in a D^3He implosion. Protons emitted from the D^3He reaction lose energy when passing through the compressed capsule shell. The areal density of target material through which the protons pass determines the amount of energy loss. Therefore, by measuring the proton-production history with the PTD and simultaneously a time-integrated proton-energy spectrum by charged-particle spectroscopy, the temporal evolution of target areal density is inferred. The areal-density evolution in D^3He implosions was first studied in Ref. 9 with the assumption that the D^3He-proton-production history is proportional to the D_2-neutron-production history. With the development of the PTD, areal-density evolution can now be inferred using the proton-production history.[10]

The PTD was developed primarily for D^3He implosions; however, the PTD is also sensitive to secondary protons and primary neutrons from D_2-fueled implosions. The PTD reactions of interest in a D_2 implosion are the following:

$$\mathrm{D} + \mathrm{D} \rightarrow n\,(2.45\ \mathrm{MeV}) + {}^3\mathrm{He}\,(0.82\ \mathrm{MeV}), \tag{4}$$

$$\mathrm{D} + {}^3\mathrm{He}\,(\le 0.82\ \mathrm{MeV}) \rightarrow p\,(12.6 - 17.5\ \mathrm{MeV}) + \alpha\,(6.6 - 1.7\ \mathrm{MeV}), \tag{5}$$

where reaction (4) is the primary reaction and (5) is the secondary. An average areal density can be inferred from the time difference of the secondary proton and primary neutron signals in the PTD.

The PTD Detector System

The PTD detector system was developed as a modification of the existing OMEGA neutron temporal diagnostic—the cryoNTD.[7] This diagnostic was designed to operate in one of the OMEGA ten-inch manipulators (TIM's). The PTD system, shown schematically in Fig. 96.24, is based on a fast scintillator (BC-422) that acts as a proton-to-light converter shielded by a thin (100- to 200-μm) foil against x-ray and direct laser illumination. The optical system, consisting of 11 lenses and 2 mirrors, is described in detail in Ref. 7. It transfers the scintillator light though the TIM and the vacuum window along a 3.5-m optical path to a high-speed optical streak camera[11] for recording. The front end of the optical system is mounted in the TIM and inserted close to the target. Since the PTD uses the existing cryoNTD optics and mechanical assembly, the current PTD scintillator is located 9 cm from the target, which is the required standoff distance for OMEGA cryogenic target operations. With additional optics, the PTD scintillator can be placed closer to noncryogenic targets. A simultaneously recorded optical fiducial provides a reference for accurate timing with respect to the incident laser pulse. Figure 96.25 shows a sample image recorded by a charge-coupled-device (CCD) camera attached to the streak camera for a D^3He implosion with a proton yield of 5.7×10^7. The horizontal axis in the image corresponds to time. The fiducial train is seen on top of the image and the scintillator output in the center. The PTD signal is averaged across the central portion of the scintillator, and the CCD background from the bottom portion of the image is subtracted to create the final temporal trace. The streak camera flat-field and geometric distortions are included in the signal processing.

The PTD Nose Cone

The nose cone is the main difference between the PTD and the cryoNTD.[7] The design of the PTD nose cone must satisfy several criteria: it must (1) be light tight to prevent direct laser illumination; (2) be able to sustain ablation, target debris, and the thermal impulse from the target implosion; (3) be transparent to protons with energies larger than 10 MeV; and (4) absorb as much of the soft-x-ray radiation as possible. The last requirement leads to a filter made from a high-Z material. Tantalum was chosen as the PTD filter material because of its strength and hardness and because 25-mm-diam tantalum foil disks are available commercially.[12] To avoid scintillator melting, a 0.3-mm-thick ultem plastic spacer ring was inserted between the filter foil and the scintillator. Without the spacer ring, the BC-422 scintillator is subject to a thermal impulse and may melt as a consequence. The final design of the PTD nose cone is shown in Fig. 96.26. The threaded retainer ring accommodates filter foils and scintillators of different thicknesses. The PTD nose cone itself is attached to the front end of the PTD

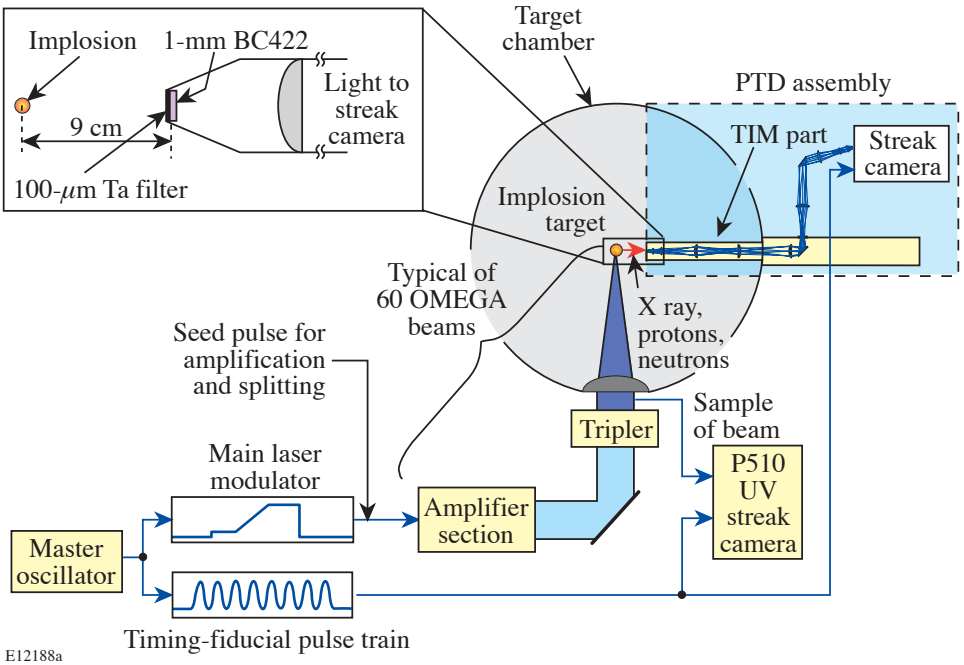

Figure 96.24
Block diagram of the PTD detector system integrated into the OMEGA facility. The fiducial system provides cross-timing between the neutron and proton signals and the incident laser pulse, which is recorded on the P510 UV streak camera.

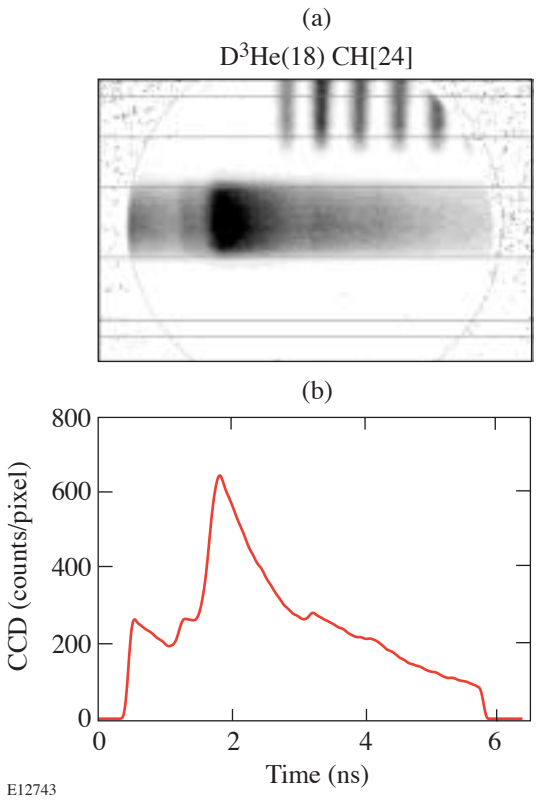

Figure 96.25
(a) The PTD streak camera image from shot #29962 in which a 24-μm-thick plastic shell filled with 18 atm of D^3He was imploded on OMEGA with a 1-ns pulse shape and 23 kJ of energy; (b) the PTD signal averaged across the central portion of the scintillator with the CCD background subtracted and the streak camera flat-field and geometric distortions taken into account.

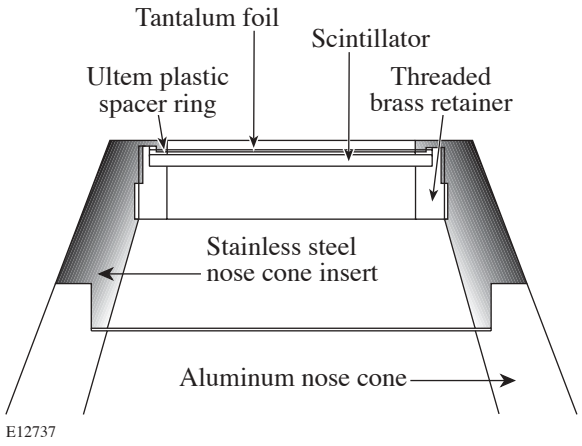

Figure 96.26
A cross-section schematic of the PTD nose cone.

mechanical assembly by two latches. It is possible to change the PTD nose cone to the cryoNTD nose cone or to change the PTD filter foil/scintillator within the 45-min OMEGA shot cycle. Tests done with 100-μm Ta foils placed 9 cm from the target show that these foils can survive more than 50 direct-drive OMEGA shots without damage.

The PTD Background

Several sources of background affect the PTD measurements. The soft and hard x rays from a target implosion reach the PTD scintillator at 9 cm from the target about 1.4 ns before the D^3He protons. The BC-422 scintillator has a very fast rise time (<20 ps) and a decay time of ~1.2 ns. The scintillator decay from x rays creates a background for the proton signal. Suprathermal electrons from the two-plasmon-decay (TPD) instability are another source of background in the PTD.[13] These electrons create hard x rays by bremsstrahlung interactions in the target and in the PTD filter foil. Since it is difficult to calculate the PTD background level, the filter thickness was optimized experimentally. The PTD background depends on many parameters such as the laser energy, pulse shape, and target design. The filter-thickness optimization required a series of identical shots where all parameters except the filter thickness were fixed. Figure 96.27 shows the PTD signal for

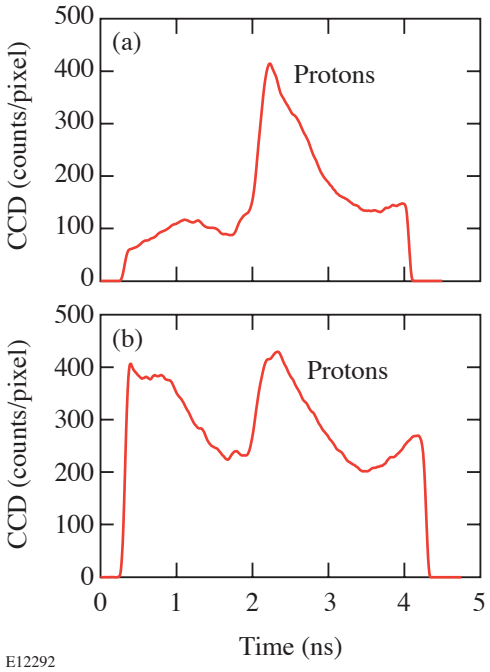

Figure 96.27
The PTD signals from two identical D^3He implosions. Minimum x-ray background is observed with the 100-μm Ta filter in (a), while the background increases significantly with the thinner 50-μm Ta filter in (b).

two identical D^3He implosions and tantalum-filter thicknesses of 100 and 50 μm. The PTD background level with the 50-μm Ta filter is about four times higher than with the 100-μm Ta filter. This means that a Ta thickness of 50 μm is not adequate to absorb the soft x rays from target implosions. Figure 96.28 shows the PTD signal for two identical D_2 implosions and 100- and 200-μm tantalum-filter thicknesses. As expected, the area under the neutron peak remained unchanged, the area under the secondary proton peak decreased (indicating that the thicker filter was stopping some fraction of the proton spectrum), and the background level decreased only marginally. A 100-μm-thick filter appears to absorb the bulk of the soft-x-ray contribution, while the hard-x-ray contribution from TPD is only minimally affected by the thicker filter; therefore, the 100-μm tantalum filter is close to the optimal for PTD operation.

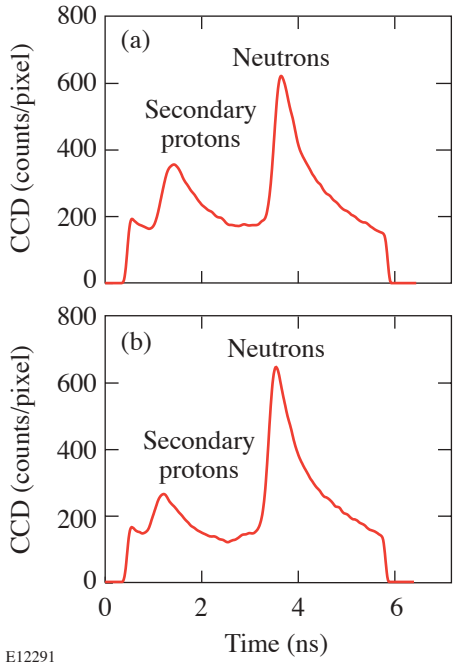

Figure 96.28
The PTD signals from two identical D_2 implosions. The background level decreases only marginally with filter-thickness increase from 100 μm Ta in (a) to 200 μm Ta in (b), while the secondary-proton signal decreases substantially.

The filter-thickness optimization discussed above was based on OMEGA operations prior to June 2003, when new distributed phase plates (DPP's) were installed and the standard spherical target diameter was reduced from 940 to 880 μm. As a result of this change, the total overlapping-beam intensity on a spherical target increased from 8.0×10^{14} W/cm^2 to 9.4×10^{14} W/cm^2, and, as was shown in Ref. 13, suprathermal electrons generated from TPD increased by approximately a factor of 4. Following this change, the PTD background level increased by factor of 4, as can be seen in Fig. 96.29, where the PTD signal is shown for two OMEGA implosions using 19-μm-thick CH shells and 15-atm-D_2 fills: (a) one before the new DPP's were installed and (b) one after installation. Tests showed that suprathermal electrons hitting the Ta filter were the main contributor to the background increase. To decrease the background level, an additional 100-μm aluminum filter was added in front of the 100-μm Ta filter. The low-Z aluminum filter absorbs suprathermal electrons before they produce hard x rays in the Ta foil. The additional aluminum filter decreased the background level by about a factor of 4, as shown in Fig. 96.30 where the PTD signal is shown for two OMEGA implosions using 27-μm-thick CH shells and 15-atm-D_2 fills: one with 100 μm of Ta and one with a sandwich of 100 μm of Al and 100 μm of Ta. The additional aluminum filter also decreases the proton signal by 10% to 20% depending on the proton energy. A 100-μm beryllium filter was also tested and found to be less effective at background reduction than the aluminum. The current PTD filter used on OMEGA consists of a sandwich of 100 μm of Al and 100 μm of Ta.

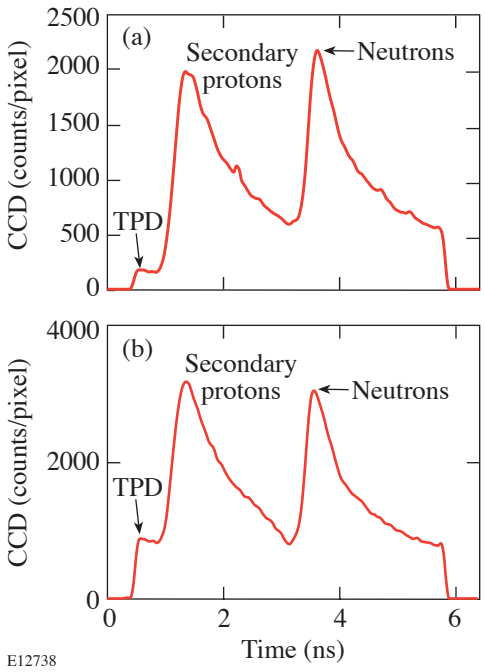

Figure 96.29
The PTD signals from two implosions of 19-μm-thick plastic shells filled with 15 atm of D_2. The PTD background level is four times smaller in (a), where the overlapping beam intensity is 8.0×10^{14} W/cm^2 in comparison with (b), where the overlapping beam intensity is 9.4×10^{14} W/cm^2.

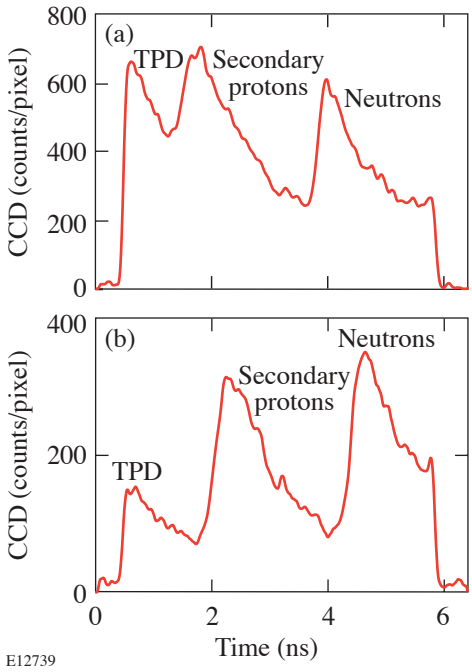

Figure 96.30
The PTD signals from two implosions of 27-μm-thick plastic shells filled with 15 atm of D_2. Overlapping beam intensity is 9.4×10^{14} W/cm^2. The PTD background level is four times higher with the 100-μm Ta filter in (a) than with a filter consisting of a 100-μm Al foil + 100-μm Ta foil in (b).

Data Analysis and Calibration

The time history of the scintillator signal is the convolution of the proton temporal distribution with the scintillator response. The actual proton burn history in the PTD is obtained by deconvolving the effect of the long scintillator decay from the recorded signal as described in Ref. 7.

Absolute timing is established using the OMEGA fiducial system. The OMEGA fiducial consists of a series of eight pulses spaced 548 ps apart and is synchronized to the shaped OMEGA laser pulse with a jitter of less than 20 ps. The optical fiducial is amplified separately from the main laser pulse, split, and distributed to various diagnostic instruments for precision timing. The fiducial pulse train is also recorded on the P510 ultraviolet streak cameras,[14] which record the laser pulse shapes of each beam. The common optical fiducial serves as a reference for both the proton signal and the laser pulse, thus enabling very accurate timing of the PTD signals relative to the laser pulse. The recorded fiducial pulse is fitted by a pulse train of eight Gaussian pulses spaced at a well-characterized period of 548 ps. This reduces the influence of noise on the determination of the timing reference.

Since the cryoNTD[7] was designed to measure only D_2 neutrons from cryogenic implosions at a fixed standoff distance, the fiducial requires only a single fiber delay to align the pulse train with the neutron signal. The PTD, on the other hand, is designed for multiple fusion reaction products and multiple standoff distances. Therefore, the PTD fiducial has ten delay fibers with nominal delays from 1 ns to 10 ns with a step of 1 ns. The delay fibers were characterized at LLNL with an accuracy less than 3 ps. Using the delay fibers, the PTD fiducial train position can be adjusted for x rays, D^3He protons, DD and DT neutrons, and a change of the PTD standoff distance.

The PTD streak camera has 3×, 5×, and 10× sweep cards that create approximately 3-ns, 5-ns, and 10-ns time windows with pixel resolutions of 7.5 ps, 13 ps, and 23 ps, respectively. The streak camera was carefully flat fielded with OMEGA fiducial pulses for each sweep card using the procedure described in Ref. 14. The streak camera flat-field and geometric distortions are included in the signal processing.

The PTD timing calibration was performed with a 100-μm aluminum filter using a 100-ps laser pulse on a spherical gold target to generate a short, intense x-ray pulse. The typical PTD calibration signal at 9 cm from the target is shown in Fig. 96.31(a), and the NTD[6] calibration signal with a similar aluminum nose cone at 2 cm from the target is shown in Fig. 96.31(b). Comparison of the PTD and the NTD signals confirms the presence of hot electrons with energies of 100 to 300 keV in the calibration shots. The time-of-flight difference between x rays and hot electrons with 100-keV energy is 55 ps for the NTD standoff distance of 2 cm and 245 ps for the PTD standoff distance of 9 cm. This time-of-flight difference explains the falling-edge pulse shape differences between the NTD and the PTD in the calibration shots. In three shots, the PTD was calibrated relative to the OMEGA laser with an rms accuracy of ~5 ps.

The PTD in D^3He Implosions

The main purpose of the PTD is to measure shock-time and areal-density evolution in D^3He implosions. A series of direct-drive implosions were conducted on OMEGA with 60 beams of frequency-tripled (351-nm) UV light in a 1-ns square pulse and a total energy of 23 kJ. Full smoothing of the laser beams was used,[15] and beam-to-beam energy imbalance was typically <5% rms. Three types of capsule designs were used, all with nominal diameters of 940 μm and plastic (CH)-shell thicknesses of 20 μm, 24 μm, and 27 μm. All of the capsules were filled with 6 atm of D_2 and 12 atm of ^3He. A typical PTD image of one of the imploded capsules with a 24-μm-thick

plastic shell is shown in Fig. 96.25. The deconvolved proton burn history for this shot is compared in Fig. 96.32 with the burn histories from implosions using 20-μm- and 27-μm-thick shells. With a 5-ns time window, the PTD pixel time resolution of 13 ps is sufficient to resolve the shock coalescence and compression peaks in these D^3He implosions. It is evident from Fig. 96.32 that the ratio of the shock yield to the compression yield in a D^3He implosion is a function of shell thickness and increases with shell thickness. A comparison of the PTD data with wedged-range-filter (WRF) spectrometer data[4,8] shows that the shock peak is much more evident in the PTD data than in the WRF spectrometers.

The primary D^3He proton yield is inferred by integrating the area under the proton shock and compression peaks. The number of CCD counts in the PTD for the 1-mm BC-422 scintillator and the filter configuration of 100 μm of Al + 100 μm of Ta is plotted against the absolute yield from the WRF spectrometers in Fig. 96.33. The PTD can measure primary D^3He proton yields and proton bang time above 1×10^7.

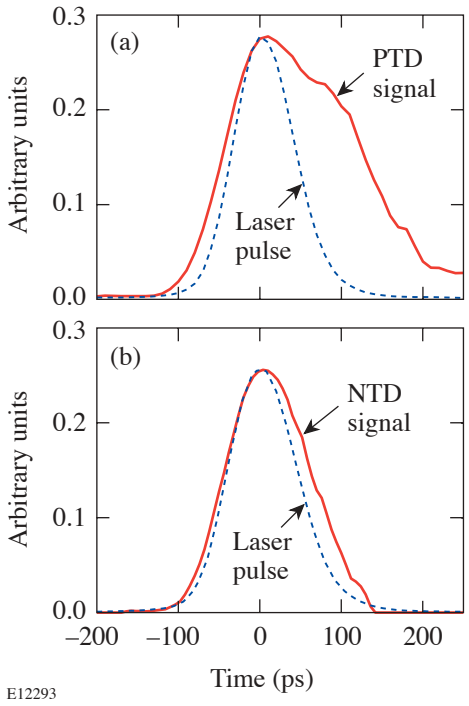

Figure 96.31
The PTD and NTD calibration signals with a 100-ps laser pulse (dashed line): (a) PTD signal (solid line) at 9 cm from a target; (b) NTD signal (solid line) at 2 cm from a target.

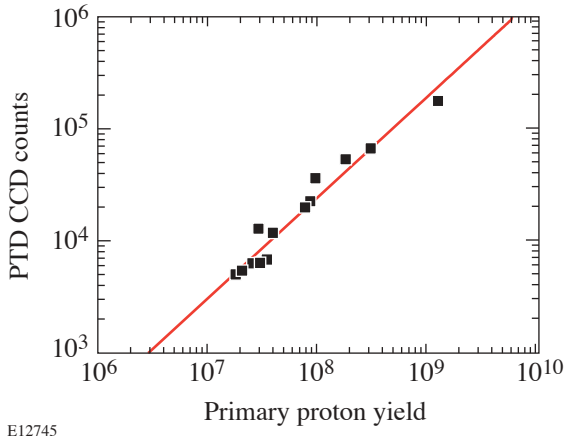

Figure 96.33
Primary D^3He proton yield measured (CCD counts) by the PTD as a function of yield measured by WRF spectrometers.

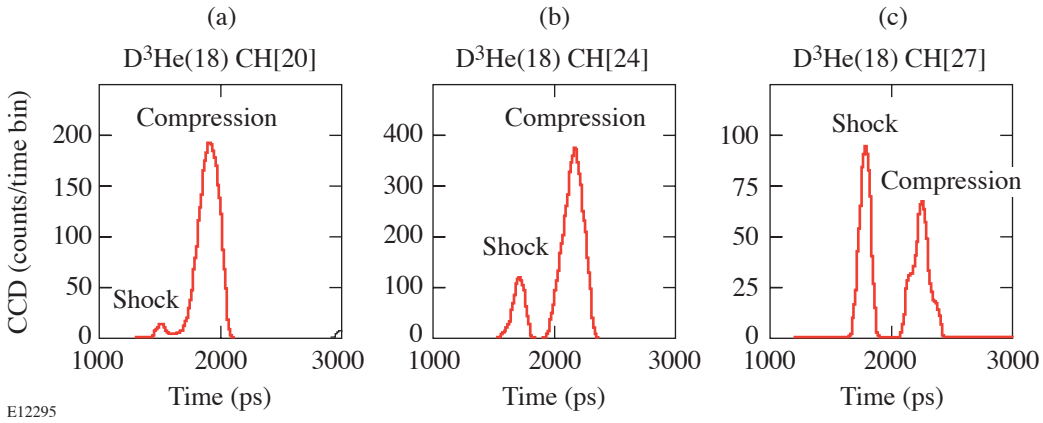

Figure 96.32
The PTD signal from implosions of plastic shells filled with 18 atm of D^3He: (a) 20-μm shell thickness; (b) 24-μm shell thickness; (c) 27-μm shell thickness.

The time accuracy of the shock and compression burn history in a D^3He implosion is mainly determined not by the detector itself, but by Doppler and geometrical broadening and ρR evolution of the fuel and shell during the implosion.[9,10] The study of ρR evolution requires data analysis from many diagnostics and is beyond the scope of this article. A more-detailed study of shock-bang timing and ρR evolution is presented in Ref. 10.

The PTD in D_2 Implosions

A typical PTD streak camera image of a D_2 implosion with a neutron yield of 1.3×10^{11} is shown in Fig. 96.34(a) and the deconvolved PTD signal in Fig. 96.34(b). In a D_2 implosion, the first PTD peak is the signal from secondary protons with energies of 12.6 to 17.5 MeV, and the second peak is the signal from the DD neutrons with an energy of 2.45 MeV. Although the yields of secondary protons and primary neutrons differ by a factor of 1000, the PTD signals are comparable due to the different interaction mechanisms of protons and neutrons with the scintillator.

The PTD neutron signal from a D_2 implosion can be used to determine the peak of neutron production (bang time) similar to NTD.[6] Figure 96.35 shows a comparison of the neutron bang time measured by PTD and NTD. The error bars on this plot are 25 ps for NTD and for PTD. The bang times measured by PTD are very close to the bang times from NTD, showing only a 28-ps rms spread. Although temperature broadening of the neutron signal in the PTD is much higher than in the NTD due to different standoff distances (9 versus 2 cm), the PTD bang time is as accurate as the NTD bang time, but the neutron burn width is systematically larger in the PTD than in the NTD due to temperature (or Doppler) broadening.

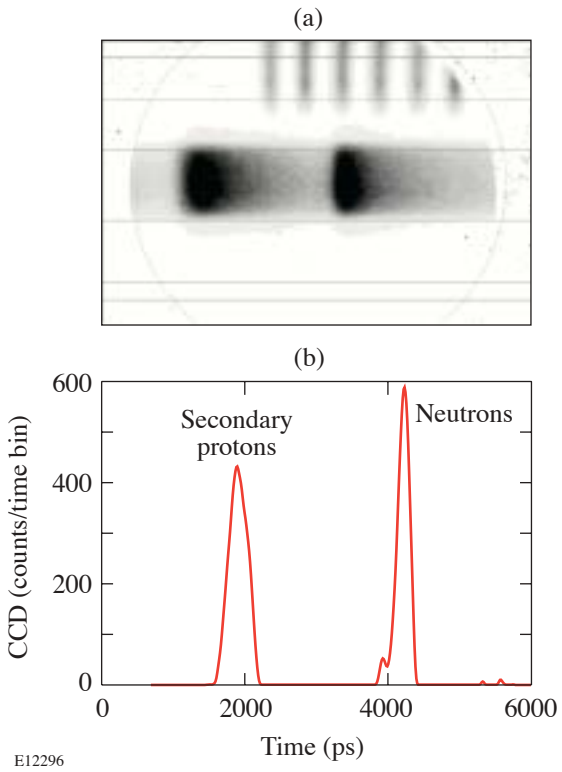

Figure 96.34
(a) The PTD streak camera image from a shot in which a 20-μm-thick plastic shell filled with 15 atm of D_2 was imploded on OMEGA with a 1-ns pulse shape and 23-kJ energy; (b) the PTD signal in this D_2 implosion. From the time-of-flight difference between the secondary-proton and the primary-neutron peaks, the average energy downshift of the secondary protons can be inferred.

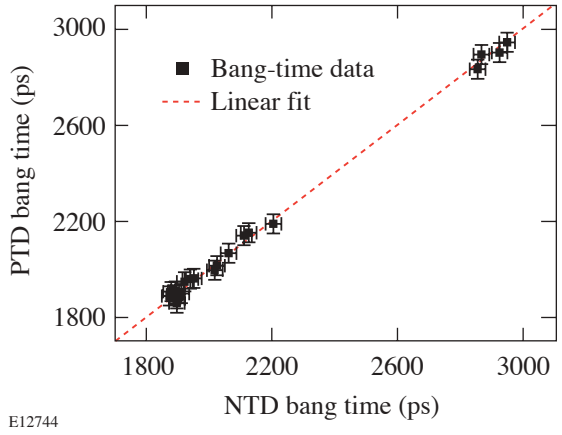

Figure 96.35
Comparison between the neutron bang times measured by the PTD and by the NTD in D_2 implosions on OMEGA.

The secondary proton peak in the PTD signal can be used to measure the secondary-proton yield in D_2 implosions. The number of CCD counts in the PTD for the 1-mm BC-422 scintillator and the filter configuration of 100 μm of Al + 100 μm of Ta is plotted against the secondary proton yield from the WRF spectrometers in Fig. 96.36. The PTD can measure the secondary proton yields in D_2 implosions above 1×10^7.

The average energy downshift of the secondary protons from a D_2 implosion is routinely used on OMEGA to measure the total areal density of the capsule.[16] The average energy downshift of the secondary protons can be inferred from the PTD based on the time-of-flight difference between the sec-

ondary proton and the primary neutron peaks [see Fig. 96.34(b)]. From the secondary proton's energy downshift, the total areal density can be calculated by using plasma-stopping formulas[17] in the same way as done with the WRF data.[16] Figure 96.37 compares the total-areal-density data inferred from the charged-particle spectrometers and the PTD. The comparison is not as favorable as that between the neutron bang times in the NTD and PTD due likely to known areal-density asymmetries[18] on OMEGA.

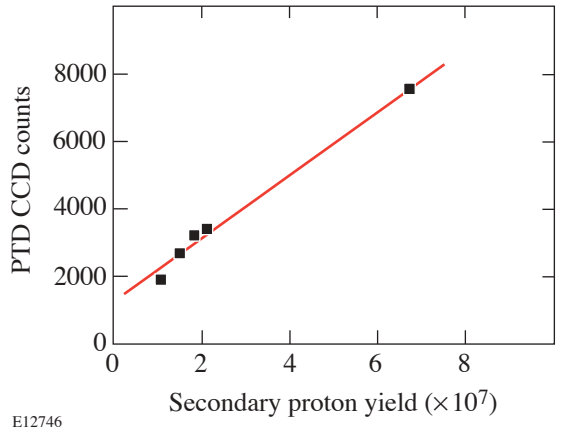

Figure 96.36
Secondary D^3He proton yield measured (CCD counts) by the PTD as a function of yield measured by WRF.

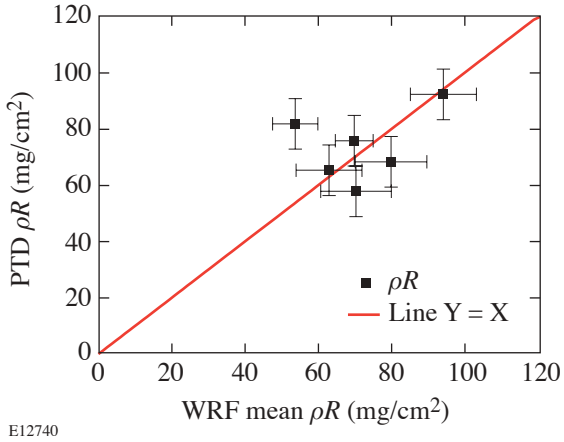

Figure 96.37
Comparison between average total ρR measured by the PTD and by the WRF in D_2 implosions.

Conclusions and Outlook

A new proton temporal diagnostic (PTD) has been developed to measure the proton burn history in ICF implosions on OMEGA. The PTD nose cone consists of a filter foil sandwich, a scintillator, and the front end of the optical relay system. This hardware is mounted in a TIM and inserted close to the target. The back end of the optical system with an optical streak camera to record the light emitted from the scintillator is mounted outside the vacuum of the target chamber. The OMEGA fiducial system is used to cross-time the x-ray, proton, and neutron signals to the incident laser pulse. An absolute timing accuracy of better than 10 ps has been achieved during the PTD calibration with 100-ps laser pulses. The PTD is able to measure the proton burn history at yields above 5×10^5 for D^3He implosions and resolve shock and compression yields. In D_2-filled-capsule implosions including cryogenic targets, the PTD can simultaneously measure neutron bang time, neutron yield, secondary-proton yield, and average total areal density.

This article has described the first implementation of the PTD on OMEGA. The PTD standoff distance can be minimized to decrease the thermal broadening and to better fit the requirements of an experiment. Future optimization of the PTD x-ray filter is also possible. In retrospect, the choice of a Ta filter does not appear to be optimal since Al is now needed in front to absorb suprathermal electrons. A sandwich of aluminum and gold foils will probably be superior. The PTD optimization on OMEGA will be continued in the future.

ACKNOWLEDGMENT

This work was supported by the U.S. Department of Energy Office of Inertial Confinement Fusion under Cooperative Agreement No. DE-FC03-92SF19460, the University of Rochester, and the New York State Energy Research and Development Authority. The support of DOE does not constitute an endorsement by DOE of the views expressed in this article.

REFERENCES

1. J. Nuckolls *et al.*, Nature **239**, 139 (1972).
2. J. D. Lindl, Phys. Plasmas **2**, 3933 (1995).
3. P. W. McKenty, V. N. Goncharov, R. P. J. Town, S. Skupsky, R. Betti, and R. L. McCrory, Phys. Plasmas **8**, 2315 (2001).
4. F. H. Séguin, J. A. Frenje, C. K. Li, D. G. Hicks, S. Kurebayashi, J. R. Rygg, B.-E. Schwartz, R. D. Petrasso, S. Roberts, J. M. Soures, D. D. Meyerhofer, T. C. Sangster, J. P. Knauer, C. Sorce, V. Yu. Glebov, C. Stoeckl, T. W. Phillips, R. J. Leeper, K. Fletcher, and S. Padalino, Rev. Sci. Instrum. **74**, 975 (2003).

5. T. R. Boehly, D. L. Brown, R. S. Craxton, R. L. Keck, J. P. Knauer, J. H. Kelly, T. J. Kessler, S. A. Kumpan, S. J. Loucks, S. A. Letzring, F. J. Marshall, R. L. McCrory, S. F. B. Morse, W. Seka, J. M. Soures, and C. P. Verdon, Opt. Commun. **133**, 495 (1997).

6. R. A. Lerche, D. W. Phillion, and G. L. Tietbohl, Rev. Sci. Instrum. **66**, 933 (1995).

7. C. Stoeckl, V. Yu. Glebov, S. Roberts, T. C. Sangster, R. A. Lerche, R. L. Griffith, and C. Sorce, Rev. Sci. Instrum. **74**, 1713 (2003).

8. R. D. Petrasso, J. A. Frenje, C. K. Li, F. H. Séguin, J. R. Rygg, B. E. Schwartz, S. Kurebayashi, P. B. Radha, C. Stoeckl, J. M. Soures, J. Delettrez, V. Yu. Glebov, D. D. Meyerhofer, and T. C. Sangster, Phys. Rev. Lett. **90**, 095002 (2003).

9. V. A. Smalyuk, P. B. Radha, J. A. Delettrez, V. Yu. Glebov, V. N. Goncharov, D. D. Meyerhofer, S. P. Regan, S. Roberts, T. C. Sangster, J. M. Soures, C. Stoeckl, J. A. Frenje, C. K. Li, R. D. Petrasso, and F. H. Séguin, Phys. Rev. Lett. **90**, 135002 (2003).

10. J. A. Frenje, "Measuring Shock-Coalescence Timing and ρR Evolution of D^3He Implosions on OMEGA," to be published in Physics of Plasmas.

11. R. A. Lerche and R. L. Griffith, in *High Speed Photography, Videography, and Photonics V*, edited by H. C. Johnson (SPIE, Bellingham, WA, 1987), Vol. 832, pp. 266–274.

12. Goodfellow Corporation, Berwyn, PA 19312-1780.

13. C. Stoeckl, R. E. Bahr, B. Yaakobi, W. Seka, S. P. Regan, R. S. Craxton, J. A. Delettrez, R. W. Short, J. Myatt, A. V. Maximov, and H. Baldis, Phys. Rev. Lett. **90**, 235002 (2003).

14. W. R. Donaldson, R. Boni, R. L. Keck, and P. A. Jaanimagi, Rev. Sci. Instrum. **73**, 2606 (2002).

15. D. D. Meyerhofer, J. A. Delettrez, R. Epstein, V. Yu. Glebov, V. N. Goncharov, R. L. Keck, R. L. McCrory, P. W. McKenty, F. J. Marshall, P. B. Radha, S. P. Regan, S. Roberts, W. Seka, S. Skupsky, V. A. Smalyuk, C. Sorce, C. Stoeckl, J. M. Soures, R. P. J. Town, B. Yaakobi, J. D. Zuegel, J. Frenje, C. K. Li, R. D. Petrasso, D. G. Hicks, F. H. Séguin, K. Fletcher, S. Padalino, M. R. Freeman, N. Izumi, R. Lerche, T. W. Phillips, and T. C. Sangster, Phys. Plasmas **8**, 2251 (2001).

16. F. H. Séguin, C. K. Li, J. A. Frenje, S. Kurebayashi, R. D. Petrasso, F. J. Marshall, D. D. Meyerhofer, J. M. Soures, T. C. Sangster, C. Stoeckl, J. A. Delettrez, P. B. Radha, V. A. Smalyuk, and S. Roberts, Phys. Plasmas **9**, 3558 (2002).

17. C. K. Li and R. D. Petrasso, Phys. Rev. Lett. **70**, 3059 (1993).

18. F. H. Séguin, C. K. Li, D. G. Hicks, J. A. Frenje, K. M. Green, R. D. Petrasso, J. M. Soures, D. D. Meyerhofer, V. Yu. Glebov, C. Stoeckl, P. B. Radha, S. Roberts, C. Sorce, T. C. Sangster, M. D. Cable, S. Padalino, and K. Fletcher, Phys. Plasmas **9**, 2725 (2002).

Polishing PMMA and Other Optical Polymers with Magnetorheological Finishing

Introduction

Polymer optics are typically manufactured by injection molding (thermoplastics, high volume, economical), compression molding (thermosets, higher precision, and larger sizes), or diamond turning. Once formed by these techniques, polymer components are used "as manufactured," usually without further cold working to improve surface finish or figure. This is because optical polymers are soft and possess high linear expansion coefficients and poor thermal conductivities.[1] Attempts to improve surface finish and figure using conventional grinding and polishing processes usually result in scratching, the embedding of abrasive particles, the formation of "orange peel,"[2] and degradation to surface figure. There are circumstances when it would be desirable to perform a classical polishing operation on a polymer surface. In some instances it is desirable to drive rms surface roughness values below 2 to 4 nm in preparation for deposition of a coating. In other applications, reduced surface form errors are required. It is advantageous to eliminate the unwanted flare from diamond-turning marks on polymer optics in order to test prototype imaging system designs.

Magnetorheological finishing (MRF) is a new polishing process that was invented and developed by an international group of collaborators at the Center for Optics Manufacturing (COM) in the mid-1990s[3] and commercialized by QED Technologies, Inc. in 1997.[4] MRF is based on a magnetorheological (MR) fluid consisting of nonmagnetic polishing abrasives (typically CeO_2 or nanodiamonds[5]) and magnetic carbonyl iron (CI) particles in water or other carriers. With the appropriate MR fluid, MRF has successfully polished a variety of materials to subnanometer rms surface-roughness levels with peak-to-valley (p–v) form accuracies to better than 20 nm. Polished materials include optical glasses (fused silica, BK7, SF6, LaK9), hard crystals and polycrystalline glass-ceramics (silicon,[6] sapphire,[7] Zerodur, and Nd: YLF[8]), soft UV and IR materials (CaF_2,[9] AMTIR-1,[10] polycrystalline ZnS,[10] and soft phosphate laser glass), and soft, water-soluble potassium dihydrogen phosphate (KDP) frequency-conversion crystals.[11]

A normal force of the order of 0.01 N between the abrasive particle and the part is the key to removal in most classical polishing processes. In MRF, however, there is almost no normal load.[12] Figure 96.38 shows a schematic of a part being placed into a ribbon of MR fluid. Shear stresses in the converging gap and the lateral motion of polishing abrasives across the part surface cause material removal without subsurface damage, leaving extremely clean, pit- and scratch-free surfaces. This has been shown to minimize the embedding of polishing powders,[13] and it suggests that MRF is an excellent candidate for polishing polymer optics.

The following sections describe our work to polish optical polymers with MRF. Materials of interest include polymethylmethacrylate (PMMA), cyclic olefin polymer (COP), polycarbonate (PC), and polystyrene (PS). Goals for removal rate, surface form error reduction, and surface microroughness reduction are established; materials of interest and forms of supply are identified; metrology instrumentation and testing protocols are given; and MRF platforms are briefly reviewed. No single MR fluid was found to be entirely successful in smoothing all polymers tested; therefore, results are presented for several MR fluid and polymer combinations. Variations in the type of nonmagnetic polishing abrasive were seen to make a difference in the ability to polish. Surface degradation observed for some polymers was overcome by changing the polishing abrasive in the MR fluid. Encouraging results for PMMA are described in detail. It was possible to demonstrate both surface figure correction and smoothing in the same processing sequence. Diamond-turning marks were eliminated. Finally, the thermalization issue in cold working of optical polymers is discussed within the context of experiments that encountered long metrology cycle times and long-term figure instability.

Methodology

1. Polymer Materials and Forms of Supply

Polymers used in this work and their trade names are identified in Table 96.I, where they are rank ordered by

hardness.[14] Forms of supply consisted of molded plano coupons, used as received, and/or rod stock that was subsequently diamond turned into plano pucks prior to use. Initial roughness values for the surfaces of the molded coupons (areal, 250 μm by 350 μm; see **Metrology and Testing Protocols**, p. 241, for metrology protocols) were in the range of 300 nm to 1600 nm p–v and 2 nm to 11 nm rms. Molded-coupon surfaces were not sufficiently flat to allow for interferometric form metrology. Initial roughness values for the surfaces of the diamond-turned pucks were in the range of 50 nm to 1500 nm p–v and 4 nm to 17 nm rms. Flatness values for the diamond-turned pucks were less than 5 μm p–v (95% aperture).

2. MRF Machine Platforms and Screening Experiments

Three MRF platforms were used to carry out experiments. The principal author and her lab partner[18] conducted an initial screening experiment in late 2001 on the permanent magnet machine (PMM),[19] a test bed primarily intended for undergraduate training in the basics of MRF. The goal of this work was to examine only the smoothing capability of nanodiamond abrasives contained in one of the commercial MR fluids, although the exact MR fluid formulation used was experimental and not entirely aqueous-based. A 60-s-duration circle was polished into a molded coupon at a part rotation rate of 200 rpm. Results for the four polymers listed in Table 96.I were

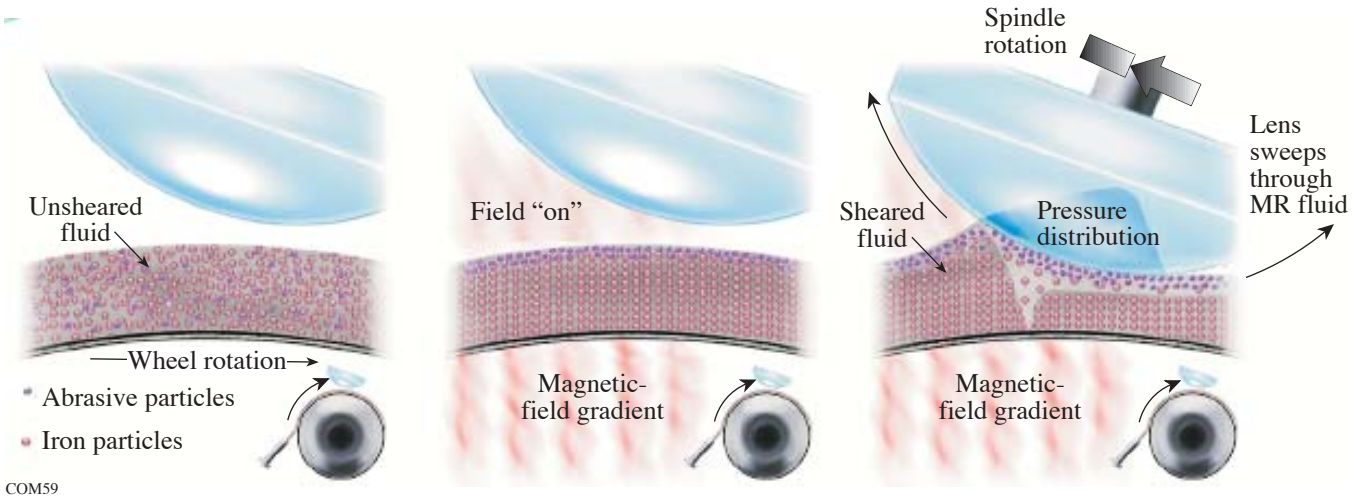

Figure 96.38
Polishing with MRF. (a) The rotating wheel carries the MR fluid ribbon under the part. (b) With the application of a magnetic field, the carbonyl iron particles form an organized structure and are pulled down toward the increasing gradient in magnetic field. Water and the polishing abrasive remain at the surface of the ribbon. (c) A converging gap is formed by placing the part into the ribbon. Solid cores of magnetic fluid form before and under the part, forcing the abrasive particles into a thin, ~150-μm channel with high velocity. Shear against the part surface causes material removal with negligible normal force.

Table 96.I: Polymer materials, forms of supply, and sizes.

Polymer	Trade Name	Rockwell (M hardness)	Form	Size (mm diameter × thickness)	Ref.
PMMA	Acrylic	97	Molded coupons Rod stock for pucks Rod stock for pucks	50 × 2.5 48 × 25 38 × ~8	(15) (16) (17)
PS	Dow Styrene	90	Molded coupons	50 × 2.5	(15)
COP	Zeonex	89	Molded coupons Rod stock for pucks	50 × 2.5 75 × 25, 50 × 8	(15) (16)
PC	Lexan	70	Molded coupons	50 × 2.5	(15)

encouraging, showing that rms roughness levels of the order of 1 to 3 nm could be achieved.

In early 2002, a series of experiments were conducted on diamond-turned PMMA and COP pucks using an MRF research platform called the spot-taking machine (STM). As previously described,[11] the STM is used to take spots on stationary part surfaces; it cannot be used to polish out a surface. The STM is intended for evaluating long-term MR fluid stability, material-removal rates for new MR fluids and/or new materials, spot shapes, and in-spot roughness. (In-spot roughness is higher than that achieved with polishing on a rotating part.) Results for experimental MR fluids revealed differences between the two materials under identical test conditions. Peak removal rates as large as 10 μm/min and 20 μm/min were obtained for COP and PMMA, respectively. These results did not correlate with material hardness. In-spot roughness values for both materials were reduced to 3 nm rms (COP) and 6 nm rms (PMMA). Diamond-turning marks were eliminated inside a spot taken on the COP part.[20]

Most of the experiments reported in this article were conducted during 2002 and 2003 on the QED Technologies Q22Y[21] machine used in rotational mode and programmed for uniform removal of material and/or for figure correction. Commercial CeO_2-based and nanodiamond-based MR fluids, as well as a number of experimental MR fluid formulations, were used under normal and "gentle" operating conditions. Experiments were performed with either the standard 150-mm-diam wheel installed in the machine or a smaller 50-mm-diam wheel. Wheel size affected spot size and removal rate, but it was assumed not to be an issue in evaluating smoothing of surfaces for different abrasives. Parts were mounted in the Q22Y work spindle using vacuum chucks and adapters provided with the machine. This facilitated easy removal of parts for in-process and post-process metrology, without the need for blocking and deblocking with waxes.

3. Metrology and Testing Protocols

The purpose of the work in 2002 and 2003 was to evaluate the potential of using MRF to process optical polymers. Specific objectives were to establish material-removal rates and to demonstrate reductions in surface roughness (white-light interference microscopy[22]) and in surface form errors (phase-shifting laser interferometry[23]). Metrology was performed in a room (T = 68±1°F) separated from the Q22Y, which was located on the shop floor (T = 71±1°F). Spotting was done on designated parts to determine removal rates for a given MR fluid on each polymer. For this, the Q22Y was automatically programmed to take a series of four individual spots on the part surface. The spots were then evaluated interferometrically and reprocessed by the Q22Y software to calculate average peak removal rates.

Surface roughness was evaluated in either of two ways: Polymer coupons not previously spotted were rotated and polished with uniform removal runs. Five sites, randomly distributed over the part surface, were sampled after polishing for rms roughness. Standard instrument settings[22] were employed. For some experiments with ZrO_2, the data were processed with an 80-μm high-pass filter. Diamond-turned pucks were evaluated for roughness in the same manner after 0.5-μm uniform removal runs, and/or after figure correction runs based upon interferometrically determined surface form error maps and removal spot data. Single-surface polishing experiments and one experiment to polish out both sides of a puck were performed.

Several adjustments were made in the metrology lab as a result of mounting and thermalization issues that were encountered. Metal sample-mounting clamps in the interferometer were covered with pads to broaden and reduce zones of high contact pressure on the part barrel. Thermal equilibration of a puck was performed each time it was returned to the metrology lab for testing by covering it with lens tissue and placing it between copper plates for 30 min.

4. Nonmagnetic Polishing Abrasives

Two magnetorheological (MR) fluids are currently in widespread industrial use: One composition consists of micron-sized CeO_2 powder in an aqueous suspension of magnetic carbonyl iron (CI) powder, which has been found appropriate for almost all soft and hard optical glasses and low expansion glass-ceramics. Preparation of this standard MR fluid and its performance have been described previously.[24] The second composition uses nanodiamond powder as the polishing abrasive, which is appropriate for calcium fluoride, IR glasses, hard single crystals like silicon and sapphire, and very hard polycrystalline ceramics[5,11,24] like silicon carbide. Both of these MR fluids were evaluated in this work, even though the abrasives in them are not commonly used for polishing polymers. Considerations leading to a choice of alternative polishing abrasives[25] are complex. Not only do the hardness and chemistry of the abrasive grains need to be appropriate to soft polymers, but the type of abrasive (e.g., crystal structure, purity, median size, friability, and surface chemistry) can appreciably affect MR fluid rheology and polishing efficiency.

It has been documented that MR fluid properties in the circulation system of an MRF machine remain constant over a 12-h work day to better than ±1% with either of the standard mixtures, resulting in removal rates that are constant to the same level.[26] Alternative abrasives must be capable of forming stable suspensions at high solids concentrations without agglomeration and with good redispersibility. Due to the high concentration and high density (e.g., 7.5 g/cm^3) of CI particles, the MR fluid must be designed to also protect against sedimentation (both static and dynamic) and corrosion. MR fluid pH levels must be kept alkaline when developing new polishing abrasive formulations, again in order to prevent sedimentation and corrosion. A serious reduction in the corrosion resistance was documented for an MR fluid made with a commercial cerium oxide powder that had been milled with an acid during manufacture.[27] Another consideration is the potential for abrasive milling by the CI particles, which are known to be harder than most polishing abrasives.[28] If this occurs at all, rapid attrition of abrasive median particle size might be preferred to attrition that occurs over a long time period. That said, it has been possible to develop and examine stable aqueous-based MR fluids containing a wide variety of metal oxide polishing abrasives.

All abrasives used in this work were obtained from commercial sources as dry powders, except for the second CeO_2 sample, which was provided as a suspension. Descriptive information for each abrasive is given in Table 96.II without any specific commercial product designations. Use of SnO_2,[29] ZrO_2,[30] Al_2O_3,[29,31] and SiO_2[31] was motivated by the existence of these as commercial formulations intended specifically for conventional polishing of polymers. Particle size and the availability of abrasive composition data from the vendor were also important considerations. As shown in the table, many agglomerated micron-size powders were broken down with time into smaller submicron aggregates[32] as a result of milling by the MR fluid. This was not the case for the TiO_2 sample, which appeared to be strongly aggregated.

Results

1. Peak Removal Rates and rms Roughness

The forms of supply limited the experiments that could be conducted. Because of their poor surface form quality, coupons of PS and PC were polished with uniform runs, removing an indeterminate amount of material, to yield roughness data. [No spots could be taken on these parts to interferometrically determine removal rates, and therefore spot data from PMMA

Table 96.II: Abrasive particles incorporated into MR fluids for polishing polymers.

Dry abrasive	Purity[(b)]	pH in DI water	Primary particle size[(b),33]	Median size[(c)]	Comments
CeO_2[(a)]	>95% rare earths	7.5	N/A	1.6 μm	Milling in MRF machine[(d)] increased vol % of particles <0.6 μm from 3 (3 h) to 15 (48 h); size distribution unchanged for next 10 days
CeO_2 (solution)	91%	N/A	40 nm	96 nm	[(b)]Provided as 20.9-wt% solids in pH7.4 solution; size distribution unchanged after milling in MRF machine[(d)] for 7 days
Diamond[(a)]	with graphite	2.5	4 nm	1.4 μm	Milling in MRF machine[(e)] increased vol % of particles <0.6 μm from 0.5 to 21 in 7 days
SnO_2	99%	4.7	N/A	370 nm	Large agglomerates broken up with intensive sonication
ZrO_2	98%	7.5	200 nm	1.8 μm	Milling in MRF machine[(d)] increased vol % of particles <300 nm from 2 to 11 (4 days) to 72 (11 days)
Al_2O_3	99% γ phase	4.7	33 nm	93 nm	Milling in MRF machine[(e)] increased vol % of particles <225 nm from 0 to 75 in 24 h
TiO_2	99.5% rutile	10.2	10 × 40 nm needles	2.8 μm	Milling in MRF machine[(d)] increased vol % of particles <1.0 μm from 2 to 8 in 14 days; aggregates remained
SiO_2	99.8%	4.7	40 nm	N/A	[(b)]Amorphous, fumed, crystalline-free, hydrophilic
[(a)]Standard MR fluid constituent; [(b)]information supplied by vendor; [(c)]powder dispersed in DI water with a surfactant and intensively sonicated prior to sizing;[33] [(d)]peristaltic pump system on Q22Y—less aggressive; [(e)]centrifugal pump system on STM—more aggressive.					

was used as input to the machine for performing (estimated) 0.5-μm uniform removal runs.] Spots were taken on diamond-turned pucks of PMMA and COP, thus enabling (precise) 0.5-μm uniform removal runs. Roughness data were obtained from these or from figure correction runs.

Table 96.III gives results for peak removal rate and lowest achieved rms roughness for the four polymers tested. Results are displayed separately for data obtained on diamond-turned pucks and coupons. Selected observations for each polymer are given as follows:

PMMA: Peak removal rates for most abrasives were between 4 μm/min and 6 μm/min, showing relatively little sensitivity to CI concentration. The higher rates for CeO_2 (solution), TiO_2, and SiO_2 were obtained with the gentlest machine-processing conditions (lower magnetic field strength and smaller wheel rpm) and were judged to be too aggressive for use. Removal rates of about 4 μm/min are entirely adequate for polishing PMMA. For example, using the standard wheel on the Q22Y under normal operating conditions with either the standard CeO_2-based or nanodiamond-based MR fluid, a 0.5-μm uniform removal run on a 50-mm-diam part would require ~20 min. Lowest achieved rms roughness values were between 1 nm and 3 nm. Results for nanodiamonds were the highest (5 nm), and those for ZrO_2 were clearly the lowest (0.5 nm). As noted in the table, the CI used with ZrO_2 had a smaller median particle size than that used with the other abrasives, and this may have contributed in part to this excellent result. As also noted, all roughness results reported in the table for ZrO_2 were obtained with an 80-μm high-pass filter. Unfiltered data for the smoothest surfaces were 0.1 nm higher.

Table 96.III: Peak removal rates and lowest achieved rms roughness values for polymers with different abrasives in MRF.

Polishing Abrasive (vol % CI)	PMMA Acrylic		PS Dow Styrene	COP Zeonex		PC Lexan
	Puck	Coupon	Coupon	Puck	Coupon	Coupon
	[peak removal rate, μm/min][d] lowest rms roughness (nm)[e]					
CeO_2[a,b] (36)	[4.0] 1.6±0.1			[3.5] 1.9±0.7[f]	1.45±0.06	
CeO_2 solution[c] (45)	[13.6]	3.9±1.1	157±27	[4.2]	13.3±9.5	3.6±0.7
Diamond[a,c] (45)	[3.7] 4.8±2.1		90±60	[2.6] 2.8±1.0	3.7±0.9	3.2±0.7
SnO_2[b] (36)	[6.3] 1.4±0.4			[2.7] artifacts		
ZrO_2[b,g] (36)	[3.6] 0.50±0.06[h]	0.58±0.07[h]	61±6[h]	[0.8] 62±8[h,i]	80±3[h]	71±3[h]
Al_2O_3[c] (45)	[4.0] 1.5±0.1		6.1±0.2		4.1±0.9	3.1±0.7
TiO_2[c] (45)	[14.6] 3.3±0.2[i]			[7.2] 6.9±2.0		
SiO_2[c] (44)	[11.6] 2.8±0.2[i]			[4.6] 116±5[i]		

[a]standard MR fluid; [b]standard 150-mm-diam wheel; [c]small 50-mm-diam wheel; [d]standard dev. est. @ ±2%, average of four spots; [e]after uniform ~0.5-μm removal runs for PMMA and COP, amounts of material removed for PS and PC not determined due to lack of spot data; [f]0.2-μm removal run, measured in areas avoiding artifacts that appeared on surface; [g]smaller CI particles used in MR fluid; [h]80-μm high-pass filter; [i]inside a spot.

PS: Coupons of this material were difficult to polish without increasing the surface roughness. Figure 96.39 shows the result of polishing with ZrO_2. Due to the evolution of surface artifacts rms roughness increased by nearly four times. Worse results were obtained for nanodiamonds. The best results were obtained with Al_2O_3. Initial areal p–v roughness of 1 μm was reduced to 56 nm, and the initial rms roughness of 6 nm was unchanged. No surface artifacts were generated.

COP: Under identical conditions, peak removal rates using most abrasives were two to four times lower than those measured for PMMA, except for the standard CeO_2-based and nanodiamond-based MR fluids. For these, removal rates were 13% (3.5 μm/min) and 30% (2.6 μm/min) lower, respectively. The removal rate for ZrO_2 (~0.8 μm/min) was too low to be practical, and there were other problems (see Fig. 96.39). Smoothing the surface without introducing artifacts was difficult. The values of rms roughness achieved with the standard CeO_2-based and nanodiamond-based MR fluids were lower (2 nm to 3 nm) than those measured with CeO_2 (solution), ZrO_2, TiO_2, or SiO_2, but significant numbers of surface artifacts were still generated. An artifact-free surface was obtained on a coupon using Al_2O_3, and the rms roughness was reduced from 9 nm (initial) to 4 nm (final).

PC: ZrO_2 degraded the coupon surface as seen in Fig. 96.39. Moderate numbers of artifacts developed after processing with the CeO_2 (solution) abrasive. The standard nanodiamond-based MR fluid was seen to reduce initial rms surface roughness from ~11 nm to ~3 nm. Similar results were observed for the Al_2O_3-based MR fluid (8 nm to 3 nm). The Al_2O_3-processed surface appeared to be the best.

2. Polishing COP (Zeonex) with the Standard CeO_2-Based MR Fluid

A 75-mm-diam by 25-mm-thick diamond-turned plano puck of COP (Zeonex) was processed on the Q22Y using the standard CeO_2-based MR fluid under gentle machine conditions. The spot removal rate was ~3.8 μm/min. Figure 96.40 shows areal roughness maps. The rms roughness (averaged over five sites) was reduced from ~23 nm to ~2 nm. Two figure-correction runs were also performed on the part. Over 90% of the aperture, p–v surface wavefront error was reduced from 1.53 μm to 0.39 μm. Inspection of the part after processing revealed a moderate number (~5/mm^2) of artifacts on the part surface (see Fig. 96.41).

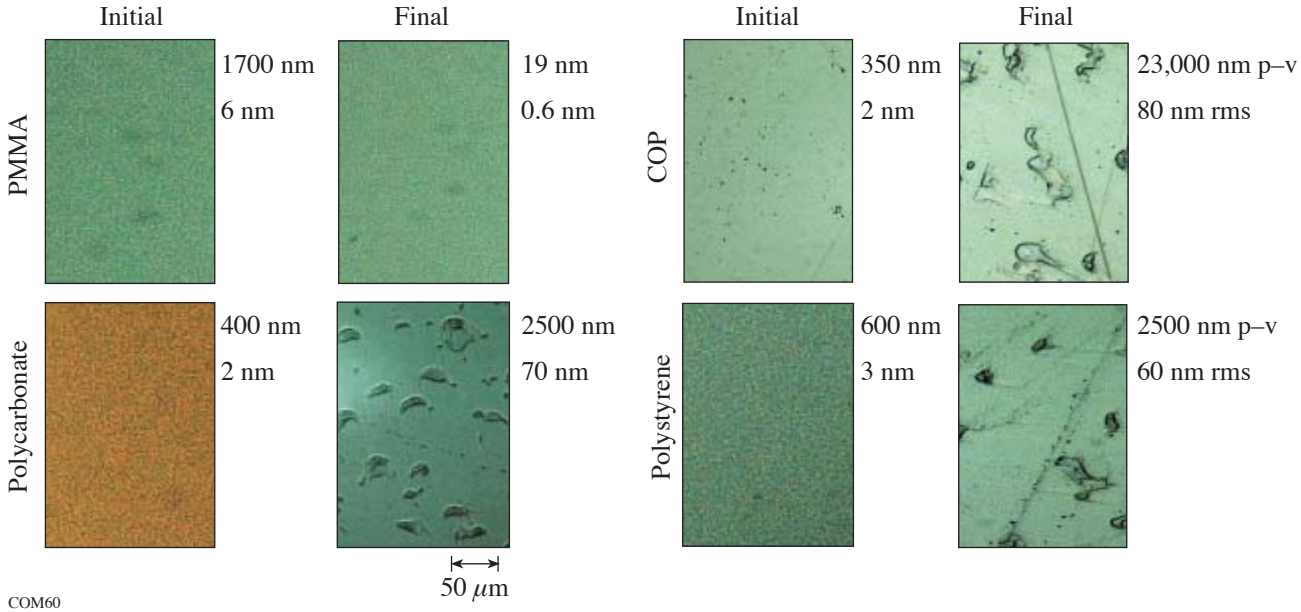

Figure 96.39
Optical microscopy of polymer surfaces after uniform 0.5-μm polishing runs with a ZrO_2-based MR fluid. Excellent results were observed for PMMA, but surface artifacts were created in PC, COP, and PS. Switching to an Al_2O_3-based MR fluid eliminated the artifact problem. (All photographs are to the scale indicated in the figure.)

3. Figure Correction and Removal of Diamond-Turning Marks on a PMMA Puck

Two 38-mm-diam by 7.8-mm-thick diamond-turned plano pucks of PMMA were processed in the Q22Y machine. One part was used to determine removal rates. White-light profilometry and laser interferometry were used to characterize one surface of the second puck for microroughness and figure (over 95% of the hard aperture) before and after each processing run. The backsides of these pucks were fine ground to simplify the metrology. Strategies were employed (described later) to minimize the time required for the pucks to come to thermal equilibrium prior to figure measurement. A ZrO_2-based MR fluid was used under standard machine conditions. This MR fluid showed excellent stability, and the experiment was conducted 9 days after the fluid had been loaded into the machine and used for other work.

The initial surface figure error of the diamond-turned PMMA puck was 4.45 μm p–v. The initial average microroughness values for this surface were 35±3 nm p–v and 3.8±0.3 nm rms. A power spectral density plot of the surface showed a strong peak at 300 lines per mm, indicating a 3-μm lateral diamond-turning groove spacing. Two figure correction runs were performed to bring down the figure error. The peak removal rate for run #1 was 3.62 μm/min and the run time was 170 min. The resulting figure error after run #1 was about 1.2 μm p–v. This value varied over time as the part recovered from the effects of handling, cleaning, and moving between the shop floor and the metrology lab. Placing the part between copper blocks in the metrology lab for 60 min and inserting padding between the part and the metal clamps in the interferometer mount helped to reduce thermal equilibration times, but ultimately the part was left in the metrology lab overnight.

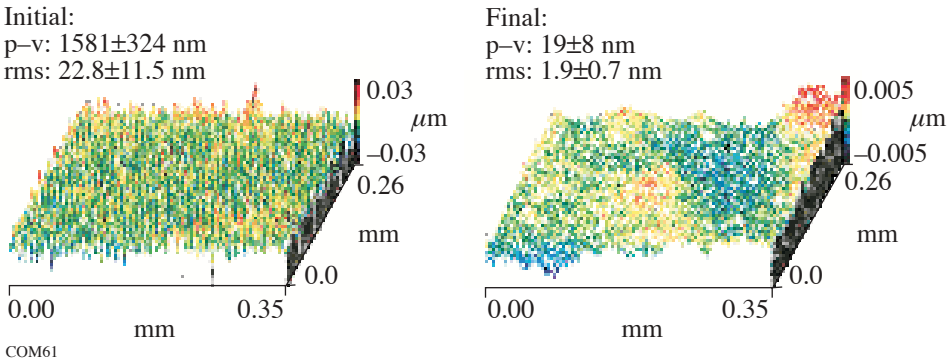

Figure 96.40
Example of areal roughness on COP surface before/after a 0.2-μm uniform removal run using a standard CeO_2-based MR fluid under "gentle" processing conditions. Numerical values given in the figure are averages of five sites.[22]

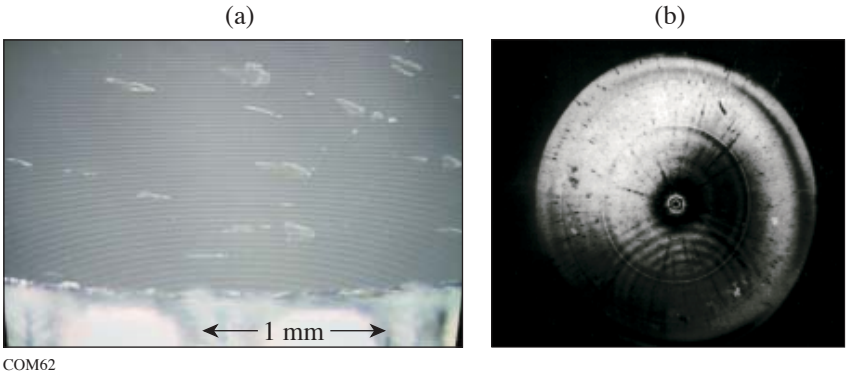

Figure 96.41
Artifacts in the surface of the COP puck at the conclusion of the polishing process: (a) view under microscope between crossed polarizers; (b) thermal printout of interferogram.

The peak removal rate for run #2 on day 2 was remeasured and found to be virtually unchanged at 3.63 μm/min. Upon completion of this second 40-min correction run, the figure error was further reduced from 1.2 μm p–v to ~0.35 μm p–v. Final surface microroughness values were 18.5±6.8 nm p–v and 0.47±0.05 nm rms. Power spectral density (PSD) plots confirmed that all diamond-turning marks had been eliminated. The PSD signature at 300 lines/mm was reduced in amplitude by over 1300×.

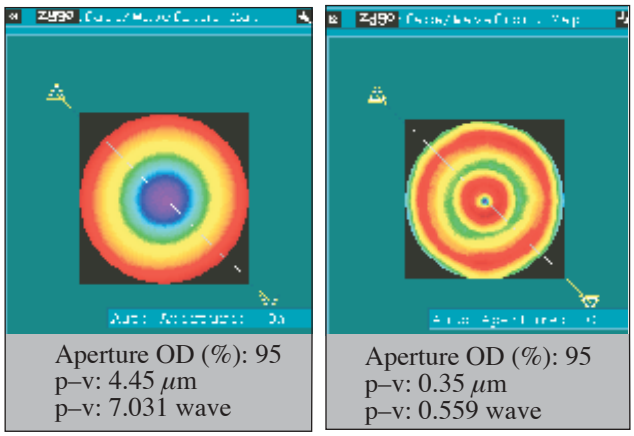

COM63

Figure 96.42
Initial and final wavefront maps for the PMMA puck (95% aperture).

Metrology results supporting the experimental findings are shown in Figs. 96.42 and 96.43. Figure 96.42 shows the initial and final wave-front maps for surface figure. Figure 96.43 shows initial and final oblique plots for surface roughness at a typical site, and Fig. 96.44 shows the initial and final power spectral density plots at the same site shown in Fig. 96.43.

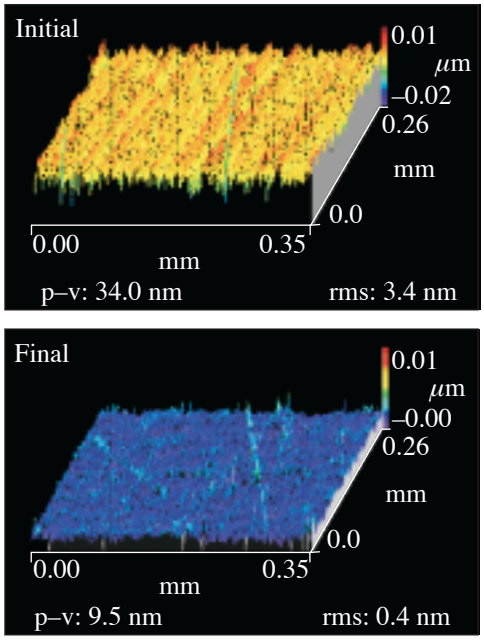

COM64

Figure 96.43
Initial and final surface-roughness values for the PMMA puck at one typical site.

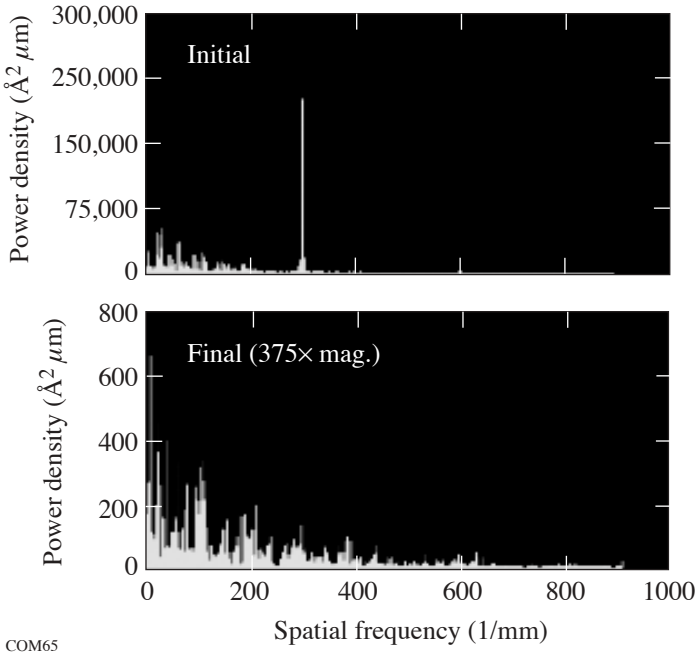

COM65

Figure 96.44
Initial and final PSD plots for the PMMA puck at the same site examined in Fig. 96.43. The diamond-turning mark signature at 300 lines/mm was reduced by more than 1300×. (The ordinate scale has been magnified by 375× to show the signature after MRF.)

4. Thermal Effects

Polymers require a longer time to thermalize than glasses, ceramics, or metals. This may be examined in two ways. The time ϕ (in minutes) required for a temperature gradient across the thickness t of a disk to decay to 10% of its initial value (heat being removed from only one side) is given as[34] $\phi = 1.67\,\rho C_p t^2/k$, where ρ, C_p, and k are density, specific heat, and thermal conductivity, respectively. Table 96.IV gives a calculation of ϕ for 8-mm-thick pucks of PMMA and COP compared to the borosilicate glass BK7. The initial thermalization time for either of these polymers is four to five times longer than that for glass of equal thickness. Table 96.IV also gives a calculation of the sag S (in microns) of a part surface due to a linear temperature gradient through the thickness t as[34] $S = \alpha\Delta T r^2/2t$, where α, ΔT, and $2r$ are the coefficient of thermal expansion, the temperature difference across the part, and the part diameter (38 mm), respectively. A gradient of less than 0.2°C across a glass part is negligible, but for a polymer puck it is still sufficient to cause a 0.3-μm distortion.

Interferometry over 95% of its aperture was periodically performed on the 8-mm-thick PMMA puck used in the two figure correction runs previously described. The puck was "soaked" between two copper blocks for 30 min in the metrology lab and then monitored for p–v figure error after the first polishing run. Figure 96.45 shows that the initial figure error of 1.2 μm decayed to 1.0 μm after an additional 60 min. A similar measurement on the part at the conclusion of the second figure correction run showed that the same equilibration protocol was necessary to stabilize the surface figure at 0.4-μm p–v. Infrared thermometry[35] performed on the puck during polishing did not detect any rise in temperature above the ambient within the machine enclosure. This equilibration time is quite lengthy compared to the calculations shown above, suggesting that temperature fluctuations within the puck may have been prolonged by the heavy traffic into and out of the metrology lab during the day. Precise interferometric testing is difficult to perform during the cold working of polymer optics.

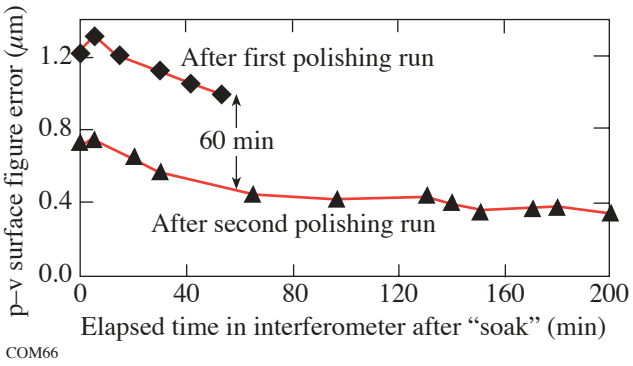

Figure 96.45
Wavefront metrology for an ~8-mm-thick PMMA puck as a function of elapsed time in the interferometer after a 30-min "soak" between copper plates. Stabilization required an additional 60 min (lines to guide the eye).

5. Long-Term Figure Instability in a PMMA Puck Polished on Both Sides

An experiment was conducted to polish out diamond-turned side 1 (S1) and side 2 (S2) of a plano PMMA puck. Puck dimensions and processing conditions were identical to those described above for the removal of diamond-turning marks. S1 was polished out on day 1 to a surface figure error of 0.33 μm p–v. S2 was polished out on day 2 to a surface figure error of 0.4 μm p–v. S1 was then monitored. Figure 96.46 shows the change in surface profile that was observed over 40 days. The center of the puck surface became concave, and by day 25 the surface figure error of S1 had degraded by almost 5× to 1.48 μm p–v. This had relaxed to 1.11 μm p–v by day 34, and to 1.09 μm p–v by day 40. We seek an explanation.

Table 96.IV: Thermal calculations for polymer and glass pucks 8 mm thick by 38 mm in diameter.

	Time to reduce temperature gradient across part to 10% of initial value					Sag in part surface from temperature gradient remaining across part (μm)			
	ρ (g/cc)	C_p (J/g°C)	t (cm)	k (W/m°C)	ϕ (min)	α (10^{-5} cm/cm°C)	$\Delta T = 5.0$°C	$\Delta T = 1.0$°C	$\Delta T = 0.2$°C
Acrylic[14,36]	1.19	1.5	0.8	0.23	8	6.7	7.7	1.54	0.3
Zeonex[14,37]	1.01	1.35	0.8	0.14	10	6.5	7.5	1.50	0.3
BK-7[38]	2.51	0.86	0.8	1.11	2	0.7	0.8	0.16	0.03

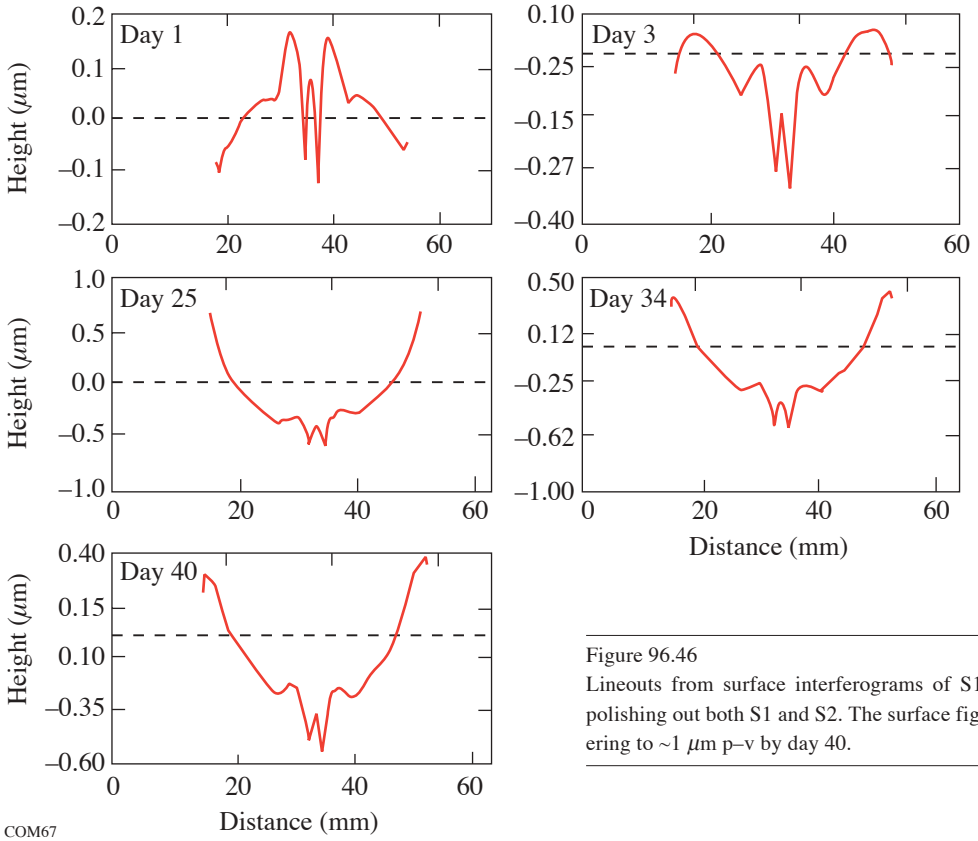

Figure 96.46
Lineouts from surface interferograms of S1 on a diamond-turned PMMA puck after polishing out both S1 and S2. The surface figure error degraded by 5× in 25 days, recovering to ~1 μm p–v by day 40.

Conclusions

Experiments were conducted with conventional and experimental MR fluids to polish four optical polymers. A ZrO_2-based MR fluid was successfully used on a Q22Y MRF machine to smooth and figure correct the plano surface of a diamond-turned PMMA part to 0.5 nm rms and 0.4 μm p–v, respectively. The diamond-turning marks were eliminated. Of the other abrasive/polymer combinations tested, Al_2O_3 showed the greatest potential for processing COP, PS, and PC without roughening or introducing surface artifacts. Issues of part thermalization for metrology were encountered. It was found that 90 min were required to stabilize the surface figure of an 8-mm-thick PMMA puck between runs and at the conclusion of a polishing experiment. Long-term surface figure instabilities were also observed for a PMMA puck after cold working both sides of the part.

ACKNOWLEDGMENT

Support for this work is provided by the Center for Optics Manufacturing. J. DeGroote is supported by the Frank J. Horton Graduate Fellowship Program.

REFERENCES

1. V. E. Sabinin and S. V. Solk, J. Opt. Technol. **69**, 48 (2002).
2. J. D. Lytle, "Polymetric Optics," in *Handbook of Optics*, 2nd ed., edited by M. Bass (McGraw-Hill, New York, 1995), Chap. 34, Vol. II, p. 34.13.
3. S. D. Jacobs, D. Golini, Y. Hsu, B. E. Puchebner, D. Strafford, Wm. I. Kordonski, I. V. Prokhorov, E. Fess, D. Pietrowski, and V. W. Kordonski, in *Optical Fabrication and Testing*, edited by T. Kasai (SPIE, Bellingham, WA, 1995), Vol. 2576, pp. 372–382.
4. D. Golini, S. Jacobs, W. Kordonski, and P. Dumas, in *Advanced Materials for Optics and Precision Structures*, edited by M. A. Ealey, R. A. Paquin, and T. B. Parsonage, Critical Reviews of Optical Science and Technology (SPIE, Bellingham, WA, 1997), Vol. CR67, pp. 251–274.
5. S. D. Jacobs, Finer Points **7**, 47 (1995).
6. S. R. Arrasmith, S. D. Jacobs, J. C. Lambropoulos, A. Maltsev, D. Golini, and W. I. Kordonski, in *Optical Manufacturing and Testing IV*, edited by H. P. Stahl (SPIE, Bellingham, WA, 2001), Vol. 4451, pp. 286–294.

7. I. Kozhinova, S. R. Arrasmith, J. C. Lambropoulos, S. D. Jacobs, and H. J. Romanofsky, in *Optical Manufacturing and Testing IV*, edited by H. P. Stahl (SPIE, Bellingham, WA, 2001), Vol. 4451, pp. 277–285.

8. J. D. Zuegel, V. Bagnoud, I. A. Begishev, M. J. Guardalben, J. Keegan, J. Puth, and L. J. Waxer, presented at CLEO, Baltimore, MD, 1–6 June 2003, invited paper CME3.

9. D. Golini *et al*., Laser Focus World **37**, S5 (2001).

10. S. D. Jacobs, F. Yang, E. M. Fess, J. B. Feingold, B. E. Gillman, W. I. Kordonski, H. Edwards, and D. Golini, in *Optical Manufacturing and Testing II*, edited by H. P. Stahl (SPIE, Bellingham, WA, 1997), Vol. 3134, pp. 258–269.

11. S. R. Arrasmith, I. A. Kozhinova, L. L. Gregg, A. B. Shorey, H. J. Romanofsky, S. D. Jacobs, D. Golini, W. I. Kordonski, S. J. Hogan, and P. Dumas, in *Optical Manufacturing and Testing III*, edited by H. P. Stahl (SPIE, Bellingham, WA, 1999), Vol. 3782, pp. 92–100.

12. A. B. Shorey, S. D. Jacobs, W. I. Kordonski, and R. F. Gans, Appl. Opt. **40**, 20 (2001).

13. J. A. Menapace *et al*., in *Laser-Induced Damage in Optical Materials: 2001*, edited by G. J. Exarhos *et al*. (SPIE, Bellingham, WA, 2002), Vol. 4679, pp. 56–68.

14. Data from *Specifications of Optical Grade Plastics*, G-S Plastic Optics, Rochester, NY 14603-1091.

15. Coupons were provided by Mr. William S. Beich, G-S Plastic Optics, Rochester, NY 14603-1091.

16. Diamond-turned pucks supplied by Mr. Paul Tolley, Syntec Technologies, Inc., Pavilion, NY 14525. Additional diamond turning of Zeonex pucks performed by Rochester Tool and Mold, Inc., Rochester NY 14611.

17. Extruded rod stock purchased from McMaster-Carr, New Brunswick, NJ 08903-0440; subsequently diamond turned by Rochester Tool and Mold, Inc., Rochester NY 14611.

18. This work was conducted by J. DeGroote and J. Watson as an independent laboratory experiment, in partial fulfillment of the requirements for the course Optics 256: Senior Lab, The Institute of Optics, University of Rochester, Rochester, NY, Fall 2001.

19. The permanent magnet machine was designed and fabricated for the Center for Optics Manufacturing in 1998 by Dr. I. Prokhorov and colleagues, Luikov Institute, Minsk, Belarus. It's capabilities and limitations are described in J. E. DeGroote, S. D. Jacobs, and J. M. Schoen, in *Optical Fabrication and Testing*, OSA Technical Digest (Optical Society of America, Washington, DC, 2000), pp. 6–9.

20. J. E. DeGroote, "Initial MRF Spotting Experiments on Optical Polymers," research project submitted in partial fulfillment of the requirements for Optics 443: Optical Fabrication and Testing, The Institute of Optics, University of Rochester, Rochester, NY, Spring 2002.

21. Q22, QED Technologies, LLC, Rochester, NY 14607.

22. Zygo NewView™ 5000 white-light optical profiler, Zygo Corporation, Middlefield, CT 06455. The instrument was set for areal mapping over 0.25 mm × 0.35 mm; 20× Mirau; FDA resolution: high; 20-μm bipolar scan; min/mod: 5.

23. Zygo GPI xpHR phase-shifting laser interferometer, Zygo Corporation, Middlefield, CT 06455.

24. S. D. Jacobs, S. R. Arrasmith, I. A. Kozhinova, L. L. Gregg, A. B. Shorey, H. J. Romanofsky, D. Golini, W. I. Kordonski, P. Dumas, and S. Hogan, in *Finishing of Advanced Ceramics and Glasses*, edited by R. Sabia, V. A. Greenhut, and C. G. Pantano, Ceramic Transactions, Vol. 102 (The American Ceramic Society, Westerville, OH, 1999), pp. 185–199.

25. A. B. Shorey, S. D. Jacobs, W. I. Kordonski, and R. F. Gans, Appl. Opt. **40**, 20 (2001).

26. W. I. Kordonski and D. Golini, J. Intell. Mater. Syst. Struct. **10**, 683 (1999).

27. I. Kozhinova, S. Jacobs, S. Arrasmith, and L. Gregg, in *Optical Fabrication and Testing*, OSA Technical Digest (Optical Society of America, Washington, DC, 2000), pp. 151–153.

28. A. B. Shorey, K. M. Kwong, K. M. Johnson, and S. D. Jacobs, Appl. Opt. **39**, 5194 (2000).

29. Technical product literature, Universal Photonics, Inc., Hicksville, NY 11801-1014.

30. Technical product literature, Salem Distributing Company, Winston-Salem, NC 27103.

31. Technical product literature, Buehler Ltd., Lake Bluff, IL 60044-1699.

32. *Primary particle*: homogeneously ordered, single domain, single crystal; *aggregate*: two or more primary particles, strongly bonded together and difficult to separate; *agglomerate*: ensembles of primary particles or aggregates, loosely bonded together and easily separated. Definitions taken from "Fundamentals of Particle Sizing," Technical Notes (7/94) from Nanophase Technologies Corporation, Burr Ridge, IL 60521.

33. Horiba LA-900 Particle Size Analyzer, Horiba Instruments, Inc., Irvine, CA 92714.

34. F. Cooke, N. Brown, and E. Prochnow, Opt. Eng. **15**, 407 (1976).

35. Minitemp® IR thermometer from Raytek, Inc., Santa Cruz, CA 95061-1820.

36. G. W. C. Kaye and T. H. Laby, *Tables of Physical and Chemical Constants and Some Mathematical Functions*, 15th ed. (Longman, London, 1986), p. 289.

37. Data from product literature, Zeon Corporation, Tokyo, Japan 100-8323.

38. Data from *Optical Glass Catalog-1994*, Schott Glass Technologies, Inc., Duryea, PA 18642.

LLE's Summer High School Research Program

During the summer of 2003, 15 students from Rochester-area high schools participated in the Laboratory for Laser Energetics' Summer High School Research Program. The goal of this program is to excite a group of high school students about careers in the areas of science and technology by exposing them to research in a state-of-the-art environment. Too often, students are exposed to "research" only through classroom laboratories, which have prescribed procedures and predictable results. In LLE's summer program, the students experience many of the trials, tribulations, and rewards of scientific research. By participating in research in a real environment, the students often become more excited about careers in science and technology. In addition, LLE gains from the contributions of the many highly talented students who are attracted to the program.

The students spent most of their time working on their individual research projects with members of LLE's technical staff. The projects were related to current research activities at LLE and covered a broad range of areas of interest including laser optics modeling, laser-beam alignment, analysis of OMEGA implosion experiments, plasma physics modeling, cryogenic target physics, liquid crystal chemistry, molecular modeling, and the development and control of laser fusion diagnostics (see Table 96.V).

The students attended weekly seminars on technical topics associated with LLE's research. Topics this year included lasers, fusion, holographic optics, atomic force microscopy, experimental error analysis, computer-controlled optics manufacturing, and microcontrollers and their applications. The students also received safety training, learned how to give scientific presentations, and were introduced to LLE's resources, especially the computational facilities.

The program culminated on 27 August with the "High School Student Summer Research Symposium," at which the students presented the results of their research to an audience including parents, teachers, and LLE staff. The students' written reports will be bound into a permanent record of their work that can be cited in scientific publications. These reports are available by contacting LLE.

One hundred and sixty high school students have now participated in the program since it began in 1989. This year's students were selected from approximately 60 applicants.

In 2003, LLE presented its seventh William D. Ryan Inspirational Teacher Award to Mr. Michael Carges, a former physics teacher at Pittsford-Mendon High School and currently at Greece Athena High School. This award, which includes a $1000 cash prize, was presented at the High School Student Summer Research Symposium. Alumni of the Summer High School Student Research Program were asked to nominate teachers who had played a major role in sparking their interest in science, mathematics, and/or technology. Mr. Carges was nominated by Joy Yuan and Siddhartha Ghosh, participants in the 2002 Summer Program.

Mr. Ghosh wrote: "The knowledge he imparts to them [his students] set him aside from many other teachers I have had in the past. Mr. Carges strives to inspire those around him in many ways….. Mr. Carges' instruction in class was truly one of the most exemplary models I have encountered in high school."

Ms. Yuan wrote: "It takes a special kind of person to be a superior teacher. This person must have a passion for teaching and demonstrate dedication toward his job as the molder of our minds. He must have a thorough understanding of the material and knowledge….. Mr. Carges was one of the few teachers who knew what they were talking about. He was able to translate [to his students] what physicists have spent centuries doing."

Table 96.V: High School Students and Projects—Summer 2003.

Name	High School	Supervisor	Project Title
Christine Beaty	Livonia High School	C. Stoeckl	Controlling Scientific Instruments Using JAVA on LINUX
Ryan Blair	Canandaigua Academy	R. Boni/ M. Millechia	Characterization of the OMEGA UV Spectrometer
George Dahl	Allendale Columbia	M. Guardalben	Pulse-Shaping Effects in Optical Parametric Amplification
Margot Epstein	Sodus Central High School	W. Bittle/ J. Depatie	Automated Laser-Beam Steering
Wen-Fai Fong	Pittsford Sutherland	R. Epstein	Non-LTE Effects on the Speed of Sound in Plasmas
Christopher Forbes	Eastridge Senior High	P. Jaanimagi	Energy and Angular Distributions of Secondary Electrons Under High Electric Field
Nathaniel Gindele	Brighton High School	J. Knauer	Deconvolution and Calibration of Diamond PCD Detectors
Rohan Kekre	McQuaid Jesuit	S. Craxton	Tuning Multiple Triplers Using the UV Spectrometer
Kathryn Knowles	Churchville-Chili	J. Delettrez	Analysis of the Ablation Process in Rayleigh–Taylor Unstable Implosions
Nadine Lippa	Byron-Bergen	A. Schmid	Single-Molecule Fluorescence in Liquid Crystal Hosts
Anthony Noto	Greece Athena	K. Marshall	Development of Weighted Chiral Indices: Their Use in Modeling Nickel Dithiolene Systems
Benjamin Schmitt	Greece Arcadia	F. Marshall	X-Ray Microscope Mirror Characterization
Nicole Toscano	Greece Arcadia	V. Smalyuk	Compressed Core Characterization of a Cryogenic D_2 Target at Peak Neutron Production
Cam Tran	Wilson Magnet	K. Marshall	Photochemically Induced Alignment of Liquid Crystals on a Polymer Surface
Michael Wozniak	Greece Athena	D. Harding/ S. Craxton	The Effects of Nonuniform Illumination on the Shape of Deuterium Ice Layers

FY03 Laser Facility Report

User demand was met in FY03 by continuing to operate extended shifts during select weeks. Over 95% of planned target shots were executed for a total of 1381 shots (see Table 96.VI). Shaped-pulse cryogenic implosions highlighted the ongoing development of direct drive cryogenic capability. A total of 20 spherical and 51 planar cryogenic D_2 shots were performed. Pulse-shape performance improved dramatically with the addition of diode-pumped regenerative amplifiers. Target irradiation uniformity was improved by implementing several changes, including a new set of distributed phase plates (DPP's) and improvements to beam-pointing precision. Highlights of other achievements and active projects as of the end of FY03 include the following:

- Installation of LLE-built diode-pumped regenerative amplifiers on all three laser drivers improved pulse shape and energy stability. Production-model regens were installed on both the main and backlighter drivers, replacing flashlamp-pumped units. Additionally, the prototype diode-pumped regen on the SSD driver was replaced with a production model. A concomitant increase in pulse-shape effectiveness from 93% in FY02 to 98% in FY03 resulted.

- Adiabat shaping using picket pulses improved the performance of direct-drive ICF targets. Picket-pulse development continued with the application of new techniques for improving picket-pulse quality and stability. Improved picket-pulse prediction routines and IR streak cameras resulted in improved picket-pulse performance.

- Laser-driver timing system modifications provided the capability to more precisely delay individual drivers with increased range. All drivers are now capable of being delayed or advanced hundreds of nanoseconds with ~100-ps precision. This new capability has been utilized extensively to improve the effectiveness of experimental campaigns.

- The implementation of a new set of DPP's provided improved irradiation uniformity for direct-drive spherical capsules. The new DPP's, designated SG4, produce a flatter intensity distribution on target than the previous set (SG3). In addition to producing a larger effective beam area on target, the SG4 DPP's have a smaller beam-to-beam shape variation than their predecessors.

- Distributed polarization rotators (DPR's) continued heavy use in FY03. All DPR's were modified for remote retraction and reinstallation, improving flexibility for reconfiguring to indirect-drive setups. Nonlinear losses in the UV were observed due to DPR reconversion. This phenomena was investigated and corrective action initiated.

- The overall OMEGA irradiation uniformity on target was improved by using active repointing. Active repointing consists of evaluating the actual beam positions on target using x-ray images of the beam spots on a 4-mm, Au-coated pointing target and then repointing individual beams. Subsequent pointing shot offsets have been reduced from ~23 μm rms to 11 μm rms.

- To allow lower beam energy while preserving pulse shape, the use of frequency-conversion-crystal doubler detuning has been implemented; it was used extensively in FY03 on limited beam sets.

- Scientists and engineers from Lawrence Livermore National Laboratory along with LLE collaborators successfully implemented a 4ω (fourth harmonic, 263 nm) target irradiation capability on one of the 60 OMEGA beams. Experiments utilizing the 4ω capability were conducted in FY03, and more extensive use is planned for FY04.

- Shot operations continued in parallel with construction of the new OMEGA EP building, which commenced in July 2003. Building construction activities were carefully monitored to ensure the stability of target positioning and beam pointing at shot time. An EP beam transport opening was also created in the east target bay wall for propagating future EP beamlines into the OMEGA target chamber.

Table 96.VI: The OMEGA target shot summary for FY03.

Laboratory	Planned Number of Target Shots	Actual Number of Target Shots
LLE	744	648
LLNL*	415	390
LANL**	124	158
SNL	25	30
NLUF	121	123
CEA	30	32
Total	1459	1381
LLE ISE		222
LLE SSP		168
LLE DD		72
LLE LPI		61
LLE RTI		45
LLE Cryo		31
LLE Astro		28
LLE PB		21
LLE Total		648

*Includes 39 shots in collaboration with LANL.
**Includes 8 shots in collaboration with LLNL.

National Laser Users' Facility and External Users' Programs

During FY03, the number of target shots dedicated to external users of OMEGA continued to increase as 733 target shots were provided. This represents 53% of the total target shots produced by OMEGA in the last year. External users' experiments were carried out by collaborative teams under the National Laser Users' Facility (NLUF) Program as well as by teams led by scientists from Lawrence Livermore National Laboratory (LLNL), Los Alamos National Laboratory (LANL), Sandia National Laboratory (SNL), and the Commissariat à l'Énergie Atomique (CEA) of France.

FY03 NLUF Experiments

Seven of the nine NLUF programs approved in the last NLUF Review carried out a total of 123 target shots on OMEGA in FY03. Approved experimental NLUF Programs on OMEGA include the following:

Experimental Astrophysics on the OMEGA Laser
Principal Investigator: R. P. Drake (University of Michigan)

This project involves experiments in compressible hydrodynamics and radiation hydrodynamics, relevant to supernovae and supernova remnants. The experiments produce phenomena in the laboratory that are believed to be important to astrophysics but have not yet been directly observed in either the laboratory or in an astrophysical system. During FY03, the work focused on demonstrating techniques that can be used to explore the onset of turbulence in the three-dimensional, deeply nonlinear evolution of the Rayleigh–Taylor instability at a decelerating, embedded interface and on studies of collapsing radiative shocks. These experiments required strong compression and decompression, strong shocks (Mach ~10 or greater), flexible geometries, and very smooth laser beams, which means that the 60-beam OMEGA laser is the only facility capable of carrying out this program. During the past year, 2.5 shot days on OMEGA were allotted to this campaign, resulting in 25 target shots.

The exciting nature of this work has motivated the development of a collaborative effort that couples a core experimental team to theoretical groups at several institutions. Simulations guide the experimental planning to enable the acquisition of high-quality data and to provide for a comparison of several codes against the experimental data. Because they are complex and explore deep nonlinear effects, these experiments are excellent for verification and validation (V&V) of complex computer codes, including those produced by the ASCI Alliance Center at the University of Chicago. This program is also a critical steppingstone toward the use of the National Ignition Facility (NIF) both for fundamental astrophysics and as a critical component of ASCI V&V.

1. Development of Turbulence in Rayleigh–Taylor (RT) Instability at a Decelerating, Embedded Interface

As the scaling analysis in the paper by Robey *et al.*[1] indicates, it should be possible to observe the transition to a turbulent state in the evolution of the Rayleigh–Taylor instability that develops from a 3-D initial condition in the OMEGA experiments. Prior experiments on OMEGA indicated that several improvements in experimental technique were required to clearly observe the turbulent transition. During the past year, three such improvements were implemented:

a. An iodine-doped plastic that can be used for the tracer layers in the OMEGA targets was developed. Iodine has a higher x-ray opacity than the bromine that was used previously; this enhances the contrast of the x-ray images and extends the time over which the growth of the instabilities can be observed.

b. X-ray radiography using a backlit pinhole was implemented. Figure 96.47 shows the geometry of the initial targets using this technique. Laser beams irradiated a spot in the middle of the rear surface of a Ti foil, producing K_α x rays. Some of these x rays passed through a 10-μm pinhole in a Ta substrate, irradiating the target. A detector behind the target recorded the image. This technique produces much brighter images, and correspondingly improved signal-to-noise ratios, than the technique of area backlighting used previously.

c. A second x-ray-backlighting view of the target is being developed, which can look along the tracer strip (see Fig. 96.47). In this view, the strip itself is very opaque, but it will be possible to detect the lateral transport of material from the strip. The development of rapid lateral transport is a signature of the "mixing transition" that occurs with the onset of turbulence. In the initial attempt to implement the second view, the two views were not shielded well enough from one another. An improved design is currently being tested.

The first two improvements worked well and produced greatly improved data, as shown in Fig. 96.48. To demonstrate the improved techniques, targets with split perturbations were used: a single 2-D perturbation on half the interface (50-μm wavelength, 5-μm peak-to-valley amplitude) and a second, short-wavelength mode (5-μm wavelength, 0.5-μm peak-to-valley amplitude) on the other half. This provided worthwhile data regarding the effects of a second mode to compare with simulations. In addition, it is now possible to obtain reasonable-quality data as late as 37 ns after the start of the laser pulse, which is much later than could be obtained previously. Analysis continues, but the preliminary conclusion is that the second mode has a much smaller effect than is predicted by the simulations.

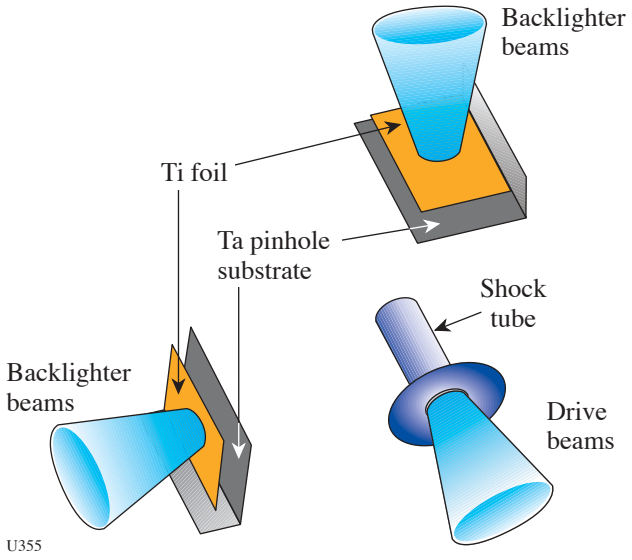

Figure 96.47
Target geometry for the Rayleigh–Taylor experiments using a backlit pinhole.

2. Collapsing Radiative Shocks

Astrophysical shocks, when they become cool enough, enter a radiatively collapsing phase in which their density can increase by several orders of magnitude. All supernova remnants eventually pass through this phase; blast waves emerging from supernovae pass through this phase, and such shocks arise in a number of other contexts. Using targets filled with xenon gas is expected to produce shocks that radiatively collapse on OMEGA. The goal is to produce such shocks, diagnose their properties, and study their evolution. This may include the development of structure due to the Vishniac instability.

Figure 96.49 shows a drawing of one of the targets that were used in these experiments. The laser beams irradiate the target from above, accelerating the thin (50 μm Be or 82 μm CH) solid layer to more than 150 km/s. This drives a shock down the tube, strong enough that it is predicted to collapse. The shock has been diagnosed using radiography (from left to right) or VISAR (through the lateral tubes). Simulations predict that x-ray radiographs should observe a collapsed xenon layer that is much narrower than the xenon layer that would be seen without the effects of radiation, as illustrated in Fig. 96.50.

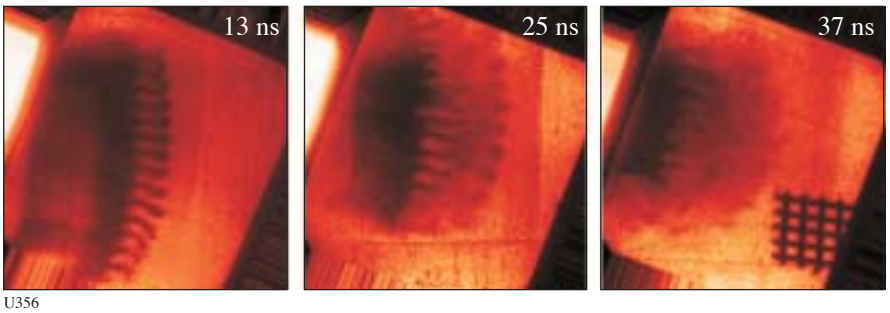

Figure 96.48
Radiographs using a backlit pinhole and an iodine-doped tracer layer.

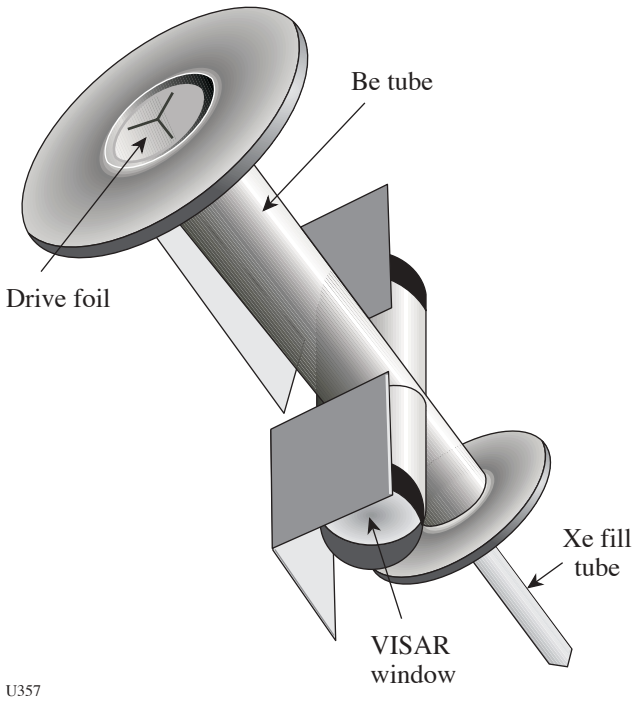

Figure 96.49
Drawing of a target used for radiative shock experiments.

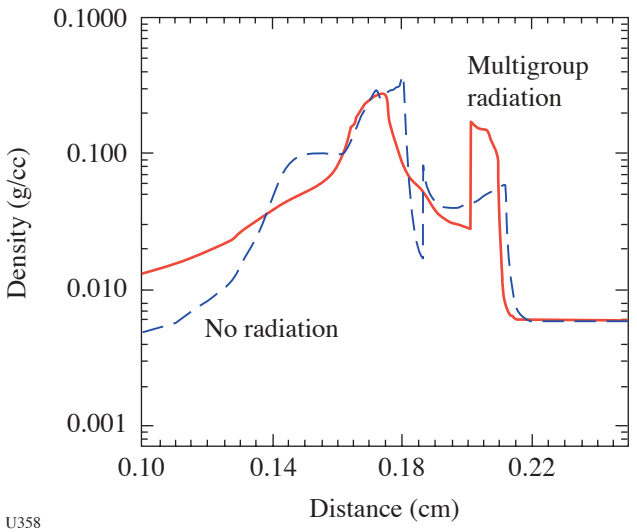

Figure 96.50
The effect of radiation should be to produce a thin, dense layer of xenon. The width of the layer in the simulation is just under 100 μm.

An actual radiograph, obtained using area backlighting, is shown in Fig. 96.51. A layer of xenon whose thickness is roughly consistent with the predictions of the simulation can be seen in this photograph. Since an improved signal-to-noise ratio is also required here, an attempt was made to employ a backlit pinhole for this application. Despite the similarity of the pinhole structure to those used previously with success, the specific pinhole design used for this experiment created shrapnel that damaged the imaging diagnostic. The next experiments will employ a modified backlit pinhole design; improved radiography is expected. The achievement of stronger shocks using a thinner initial layer, driven with SSD-smoothed laser beams, is also anticipated.

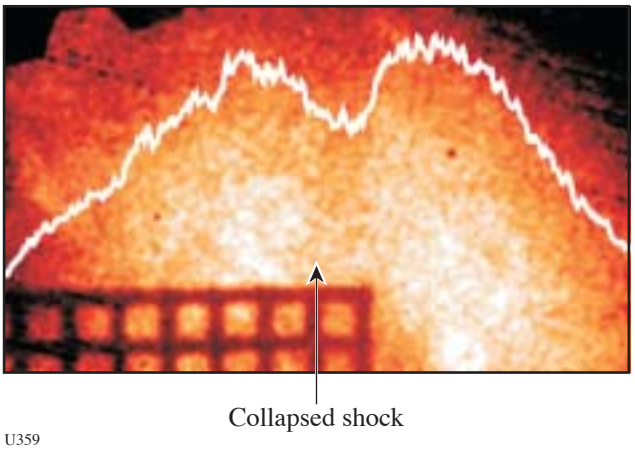

Figure 96.51
Radiograph of a shocked layer in xenon gas. The squares in the grid are 63 μm from wire center to wire center, so the observed layer is ~80 μm thick.

Several publications on experimental astrophysics were published by this group during the past year (see Refs. 1–5).

Optical-Mixing–Controlled Stimulated Scattering Instability V (OMC SSI V)

Principal Investigator: B. B. Afeyan (Polymath Research Inc.)

The principal aim of this program is to investigate the evolution of backscattering instabilities of a witness beam in the presence of optical-mixing–generated plasma waves created by beating a blue pump beam with a green probe beam. This experiment was allotted 1.5 days of OMEGA time in FY03 and a total of 21 target shots were taken. In FY03, crossed blue- and green-beam experiments were conducted in exploding foil targets for the first time on OMEGA using a wide-enough DPP-generated spot so as not to be overwhelmed with excessive green-beam filamentation. A new phenomenon was observed that not only confirms that energy was success-

fully transferred from the blue beam to the green beam, but also confirms that a significant increase in the Raman backscattering of the green beam was triggered due to its interaction with the blue. A 15-fold increase in peak energy reflected by SRS (stimulated Raman scattering) was observed at an incident green-beam energy level of 100 J, while the crossing blue beam was at 500 J as compared to the same energy in green with the blue beam off as shown in Fig. 96.52. Figure 96.52(a) shows the SRS signal from the green beam alone, while Fig. 96.52(b) shows the backscattering of the green beam when the crossing blue beam is near 500 J. Figure 96.53 shows the same phenomenon for different target illumination conditions that gave rise to a hydrodynamic expansion that reached the necessary resonant density for energy transfer between the blue and green beams later in time and at colder temperatures. The same phenomenon is observed later in time, confirming the validity of the interpretation and the exceptional reproducibility of this instability energy transfer result, where incident blue-beam energy ends up becoming SRS-reflected energy from the green beam. This is a new wavelength conversion process where long wavelengths are produced by a controlled two-step process. It implies that the interpretation of the physics of laser–plasma interactions based on single interaction-beam experiments may be incomplete when extrapolated to predict the behavior of multiple beams crossing in a plasma. The results may not be strictly additive but highly nonlinear and multistep in nature. These new phenomena are being studied using parallel Vlasov–Maxwell simulations. Transmitted-beam diagnostics on the green probe beam confirm these findings by showing that the energy transfer from the blue to the green crossing beam was approximately a factor of 2.

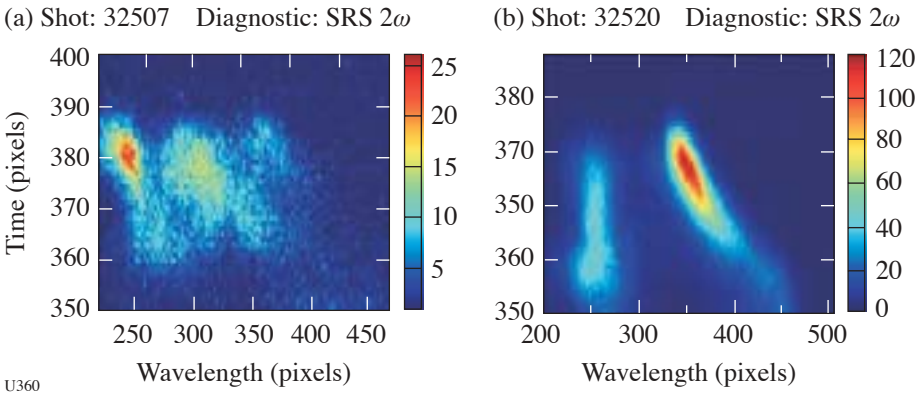

Figure 96.52
SRS reflectivity of a green beam in the absence (a) and presence (b) of a blue crossing beam. The peak reflectivity is increased by a factor of 15 or more when the signature of the peak of the exploding foil is considered (long-wavelength feature).

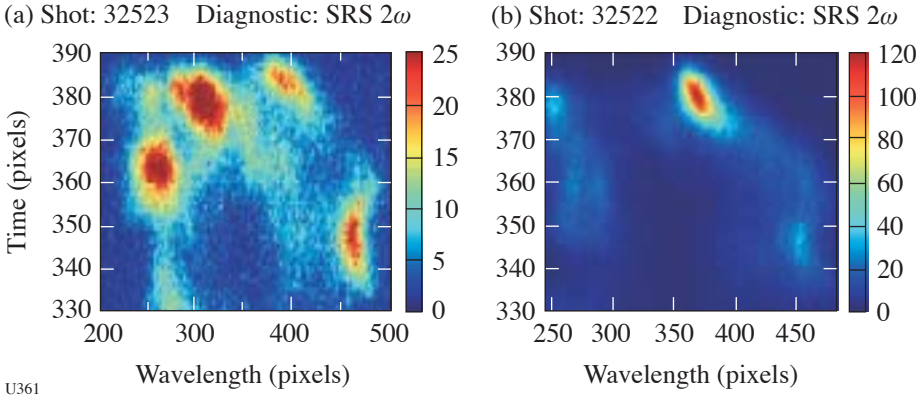

Figure 96.53
Same as Fig. 96.52 except that the plasma expansion is now delayed due to the elimination of two of the plasma heater beams. Note how Fig. 96.53(b) is very similar to Fig. 96.52(b) except for the time delay and subsequent reduction in the temporal extent of the green-beam SRS backscattering.

Time Evolution of Capsule ρR and Proton Emission Imaging of Core Structure

Prinicpal Investigator: R. D. Petrasso (Plasma Science and Fusion Center, MIT)

This program is aimed at the use of charged-particle measurements to address important issues in inertial confinement fusion (ICF) and high-energy-density physics. During FY03, 1.5 OMEGA shot days were allotted to this program, and 18 target shots were taken. The experiments were in two main areas: proton core imaging and studies of ρR asymmetry growth.

1. Proton Core Imaging Spectroscopy (PCIS) for OMEGA Implosions

Penumbral proton imaging was used to study the spatial distributions of DD and D^3He reactions in imploded D^3He-filled capsules on OMEGA.[6,7] The imaging was performed with a pinhole camera in which the recorder consisted of stacked sheets of CR-39 nuclear track detector separated by ranging filters, which resulted in efficient detection of 14.7-MeV D^3He protons on one sheet [see Fig. 96.54(a)] and 3-MeV DD protons on another. Measurements of the nuclear burn region are important for investigating the extent of the burn, the presence of burn asymmetries, the effects of mix and thermal conduction on the burn region, and the accuracy of code predictions. When target capsules have thin shells (e.g., 1.8 μm SiO_2), allowing both proton types to escape at burn time, the images on separate sheets of CR-39 can be used to reconstruct simultaneous radial profiles of DD and D^3He burn. These can in turn be used to determine the fuel ion temperature (T_i; see Fig. 96.54) and the density (n_i). When capsules have thick shells (e.g., 20 μm CH), only the 14.7-MeV proton can escape through the capsule ρR at bang time and the measured D^3He burn profile reflects the effects of compression and mix; but DD protons do escape at the earlier time of first shock coalescence, when ρR is far below its peak value, and the DD burn profile at that time can be studied. Since mix has been experimentally shown to be inconsequential at this instant, mean-ingful comparisons of 1-D simulations with experiments can be made.

2. Studies of ρR Asymmetry Growth Rates and the Relationship Between Laser Drive Asymmetry and ρR Asymmetry

During 2003, a series of shots were undertaken to study the implications of laser drive asymmetry for implosion dynamics and capsule performance, and several important conclusions were drawn from the resultant data. The series included six implosions of room-temperature capsules with 26-μm-thick CH shells and 18 atm of D^3He gas fill, using 60 laser beams with full beam smoothing and ~23 kJ of total laser energy. Illumination asymmetry was introduced in a controlled way by offsetting the capsules from target chamber center (TCC) by specific amounts, resulting in deviations of the on-target laser intensity $\delta I(\phi)$ from the mean $\langle I \rangle$ that are dominated by mode numbers 1 and 2. Diagnostics used to record crucial data included six wedged-range-filter (WRF) proton spectrometers, the proton temporal diagnostic (PTD), x-ray framing cameras, pinhole cameras, and the GMXI framing camera. Figure 96.55 illustrates sample proton spectra recorded during implosions with three different target offset amounts, showing how the spectra are dramatically different at different angles and for different offsets. Each spectrum can be decomposed into two parts representing proton emissions at the time of first shock coalescence and at bang time (these times occur roughly 1.7 and 2.1 ns after the onset of the 1-ns laser pulse, respectively).

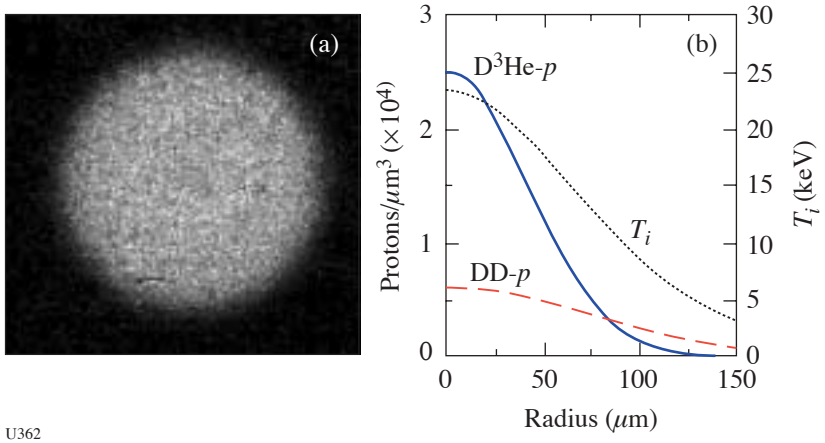

U362

Figure 96.54
PCIS data from OMEGA shot 27456, in which the capsule consisted of 18 atm of D^3He in a 1.8-μm SiO_2 shell. (a) An image of D^3He protons made behind a 600-μm-diam pinhole. Since the pinhole is much larger than the compressed capsule, all structural information is contained in the penumbra. (b) Radial profiles of proton emissivity in the imploded capsule, inferred from five pinhole images of D^3He protons and five pinhole images of DD protons. Since the local ratio of the two reaction rates is a function of ion temperature T_i, the radial profile $T_i(r)$ can be inferred.

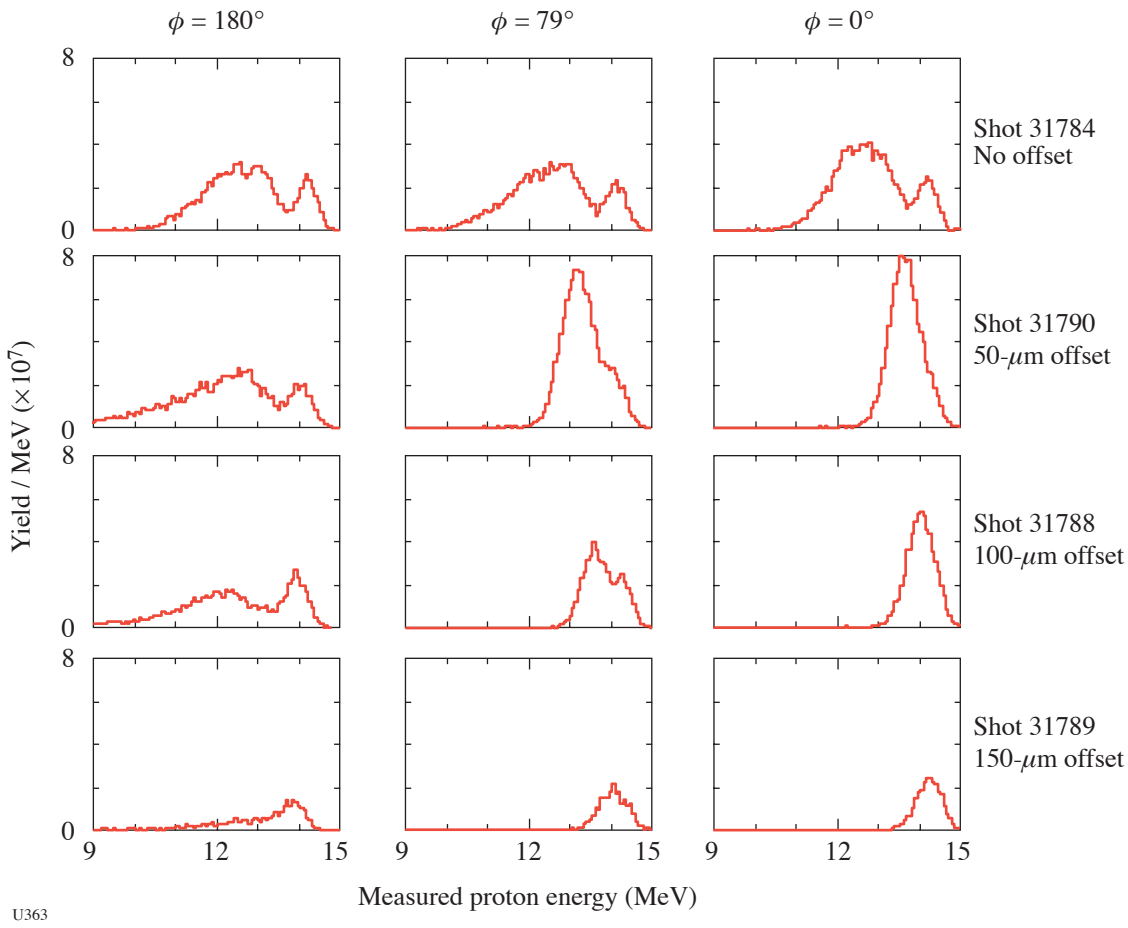

Figure 96.55
Proton spectra recorded at three important angles with respect to the direction of offset of the capsule from target chamber center. Offsets produce an asymmetric laser drive intensity on the capsule surface, with the maximum value at 180° and the minimum at 0° (see Fig. 96.56 for an example). With no offset, the spectra are all very similar, indicating an implosion that was quite symmetric. As the offset gets larger, ρR asymmetries get progressively larger and the size of the lower-energy peak (due to emission at compression time) becomes progressively smaller while the shock-time peak maintains a relatively constant size (see Fig. 96.57).

The energy spectra of the D^3He protons were used to characterize the areal density (ρR) as a function of angle at shock time and at bang time using spectrometers at different angles. It was found that the angular shape of the drive asymmetries is imposed on the ρR variations and maintained with no phase change through shock and bang times, as shown in Fig. 96.56. The growth in amplitude was roughly consistent with that recently predicted for Bell-Plesset–like convergence effects.[8] At each time, $\delta\rho R(\phi)/\langle\rho R\rangle \approx 0.4(C_r - 1)\delta I(\phi)/\langle I\rangle$, where C_r is the radial compression ratio at that time and $\delta I(\phi)/\langle I\rangle$ is averaged over the laser pulse. The mean ρR at each time can also be used to estimate C_r, which turns out to be essentially independent of offset at shock time but a decreasing function of offset at compression time.

Considering the fuel, the data provide information about the dynamics of shock coalescence and the state of the fuel at bang time. The character of the shock coalescence is particularly important because simulations predict that asymmetrically launched shocks will not coalesce coherently enough to heat the hot spot. It was found in the experiments that, although the shock coalescence for offset targets was smeared out in time and space, the number of D^3He protons emitted at this time was less sensitive to drive asymmetry than expected (Fig. 96.57). In fact, simulations had indicated that there would be no shock yield at all for the largest capsule offsets used. The yield at bang time, on the other hand, did diminish with increasing offset. This is qualitatively consistent with the finding from the ρR studies that the radial compression ratio decreased with increasing illumination asymmetry.

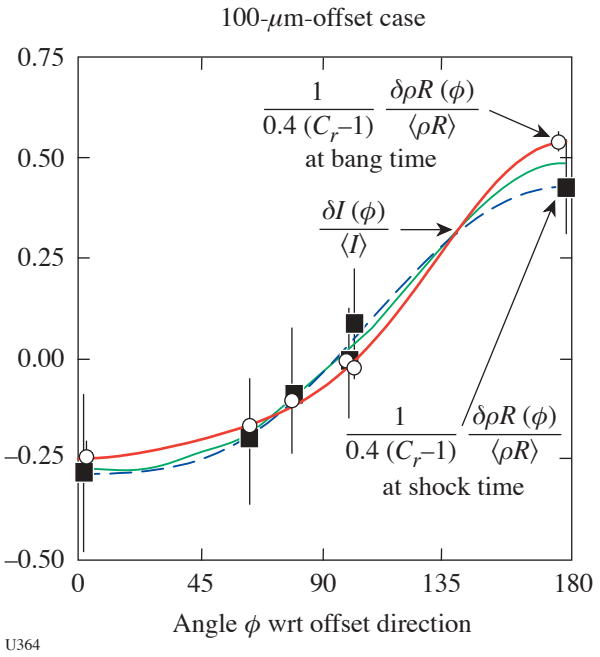

Figure 96.56
For an offset target implosion, the angular distribution of the measured ρR is similar at different times during the implosion.

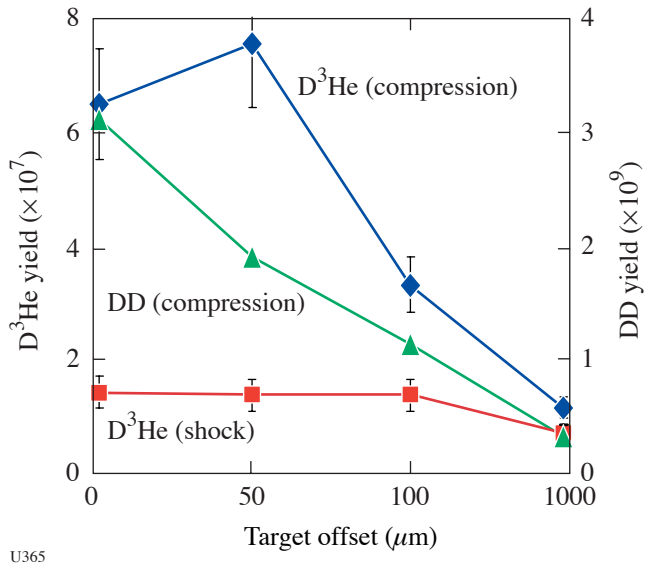

Figure 96.57
D^3He and DD proton yields as a function of the offset of targets from TCC. Despite the smearing of the shock coalescence in space and time, the D^3He proton yield at shock time remains largely unaffected by the drive asymmetry caused by target offset, while the yield at compression time decreases with offset.

OMEGA Laser Studies of the Interaction of Supernova Blast Waves with Interstellar Clouds

Principal Investigator: C. McKee (University of California, Berkeley)

The objective of this experiment is to conduct experiments on OMEGA to (1) explore the role of turbulence in laser–target interactions and (2) study the laboratory analog of astrophysical "mass-loaded flows." The current experiments involve the interaction of strong shocks with single and multiple dense clumps embedded in a low-density inter-clump background.

By varying the composition and size of the target, the investigators were able to systematically vary the Reynolds number (Re) of the flow and study the onset of turbulence in a compressible flow. These experiments are relevant to astrophysical flows in which powerful shock waves produced by supernovae, stellar winds, and other phenomena propagate through an inhomogeneous medium. Mass is stripped from clouds and injected into the low-density, generally hot, intercloud medium—a phenomenon known as mass loading. These experiments specifically address the question of how the mass loading is affected by the Re of the flow. It is possible to determine whether there are significant changes in the mass and momentum exchange between the cloud and the intercloud medium at Re higher than those accessible to direct numerical simulation (the limit on numerical simulations is typically $\mathrm{Re} < 10^3$). A specific goal of the investigation is to find evidence for the transition from a vortex sheet to a turbulent wake; this appears at $\mathrm{Re} \sim 2 \times 10^4$ in compressible flow experiments. During this first year of the study, a single dense clump (sphere) is used; future work may extend this research to the case of multiple clumps. The results of the experiments will be compared with both 2-D and 3-D direct numerical simulations using adaptive mesh refinement.

During FY03, 1.5 shot days were allocated for these studies, and 14 target shots were taken. The experiments for this first year were directed to demonstrating a clearly diagnosable transition to a turbulent flow, which the investigators believe may look like that observed in incompressible experiments. Side-on and face-on radiographic images of reasonably high quality at 5 ns (face-on only), 12 ns, 19 ns, and 26 ns were obtained. Figure 96.58 shows side-on radiographic images that display the evolution of the shocked spherical cloud at 12 ns, 19 ns, and 26 ns. At 12 ns, the shock has just passed over the cloud, and the spherical cloud displays a symmetrical extension in the axial direction with the start of a Kelvin–Helmholtz rollup of the sides of the cloud. By 19 ns, corresponding to 6.7

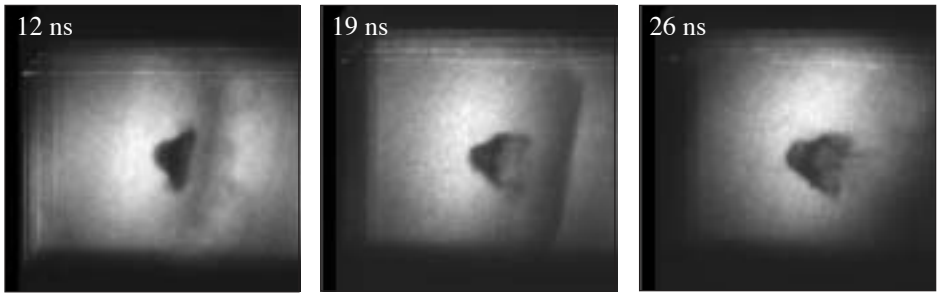

U366

Figure 96.58
X-ray radiographic images of the interaction of a strong shock wave with a spherical object. The sphere is initially 120 μm in diameter and located 500 μm from the ablative surface of a 1500-μm-diam cylindrical shock tube. (The side of each square image is approximately 1150 μm.)

crushing times, the face-on images (not shown) display the initial development of the vortex-ring instability predicted and observed in earlier work on Nova and OMEGA.[9,10] The basic symmetry of the shocked sphere seen in the side-on radiograph indicates that the flow is most likely still laminar. At 26 ns, corresponding to 9.8 crushing times, nonaxisymmetric flow is clearly evident in the side-on radiographs with evidence of asymmetric jetting and strong Kelvin–Helmholtz instabilities. This is most likely the start of strong vortex-ring instabilities and the transition to turbulent flow. Two-dimensional simulations to model the shock–sphere interaction have been conducted. Later time evolution of the interaction will require detailed 3-D AMR simulations that will also be performed.

High-Spatial-Resolution Neutron Imaging of Inertial Fusion Target Plasmas Using Neutron Bubble Detectors
Principal Investigaor: R. K. Fisher (General Atomics)

The goal of this research is to develop techniques to record the bubble spatial distribution in a high-efficiency liquid bubble chamber that may have potential use for NIF neutron imaging. This program had only limited funds and no dedicated shots in FY03. Its focus was the study of alternative bubble-recording techniques, including light scattering and x-ray transmission, with the goal of determining the most-promising method prior to initiating laboratory tests.

An initial assessment of x-ray transmission was carried out, and the following potential advantages of this approach were identified:

– a change in x-ray transmission allows measurements under expected NIF conditions since there will be many bubbles behind bubbles;

– the photoelectric effect dominates x-ray attenuation and minimizes the multiple scattering "crosstalk" issue inherent in light-scattering approaches;

– bubble-distribution measurements should be allowed over a wide range of NIF *n*-yields; flash x-ray timing can be chosen to optimize bubble radius and, therefore, $\Delta(\rho x)$ along x-ray paths.

1. Future Plans

- Complete preliminary assessment of x-ray and light-scattering approaches to bubble distribution measurements.

- Perform laboratory tests to address important issues, e.g., the effects of multiple scattering during light scattering/transmission measurements.

- Prepare for system tests/neutron-imaging experiments to test bubble chamber and readout techniques on OMEGA in FY05 and later.

  – The bubble chamber used will depend on the status of LLE and Russian research on bubble detector development for neutron imaging.

Dynamic X-Ray Diffraction of Shocked Single Crystals
Principal Investigator: M. Meyers (University of California, San Diego)

The NLUF x-ray-diffraction project focused on two separate goals: (1) to use the *in-situ* diffraction technique to study the response of a single-crystal lattice to shock loading, and (2) to characterize the deformation mechanisms in metals by shocked-sample recovery and electron microscopy. During FY03, two days of OMEGA shot time were allocated to this project, and 21 target shots were taken.

The *in-situ* diffraction technique provides a direct measurement of the lattice response under shock loading. It may be used to characterize a solid–solid phase transition such as the bcc–hcp transition in iron. The configuration for the diffraction

experiments was modified to use a different shock drive beam incident on the same side of the sample as the x-ray-diffraction probe in order to be able to hold the sample under compression for a longer time during the diffraction measurement. This modified geometry is shown in Fig. 96.59.

Recovery experiments provide a simple way to examine the deformation mechanisms governing high-strain-rate phenomena. By examining the residual microstructure and defect substructure with advanced analytical tools like transmission electron microscopy, the mechanisms in operation during shock loading can be inferred. The goal of these recent experiments is to probe the transition between the mechanisms of slip and twinning in single-crystal copper and copper–aluminum alloys in terms of composition, pressure, and orientation. Figure 96.60 shows micrographs of copper 2 wt% aluminum shot with laser energies of 200 J, which correlates to a peak pressure of 40 GPa. In the first image [Fig. 96.60(a)], the orientation is [001] and four twinning variants are observed. The second image [Fig. 96.60(b)] is the orientation $[\bar{1}34]$ revealing two sets of microtwins.

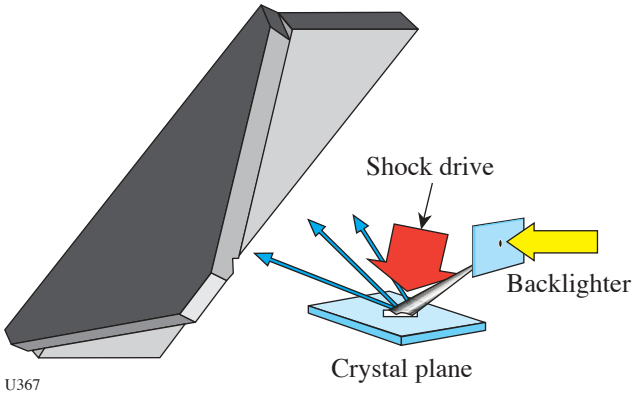

Figure 96.59
Schematic illustrating the geometry of the dynamic x-ray-diffraction experiment.

Study of Driven Ion-Acoustic Waves Under Direct-Drive Conditions

Principal Investigator: H. Baldis (University of California, Davis)

The aim of this program is to study the physics of laser interactions with ion-acoustic waves (IAW's) in plasmas at conditions relevant to direct-drive inertial confinement fusion (ICF) targets on the National Ignition Facility (NIF). Though no OMEGA shots were scheduled for this program in FY03, good progress was made on the understanding of the seeding of stimulated Brillouin scattering (SBS) by a number of effects. In direct-drive ICF geometry, many laser beams overlap with different angles of incidence, at any point over the capsule. In the plasma corona surrounding the capsules, this leads to a number of wave–wave coupling configurations, which modify the initial growth of the SBS instability. Preliminary studies have been carried out, both theoretical and experimental, on the effect of reflection of laser light and forward-scattered light from the critical density, as well the effect of seeding by side-scattered SBS light from adjacent beams.

The shots allocated to this project on OMEGA in FY04 will be dedicated to experiments to characterize some of these seeding mechanisms. The recently incorporated Thomson-scattering diagnostic will be used, at 4ω, to study the amplitude and saturation of IAW's associated with SBS. An important component will be the identification of seeding of the instability, by either sidescattering from adjacent beams or reflection

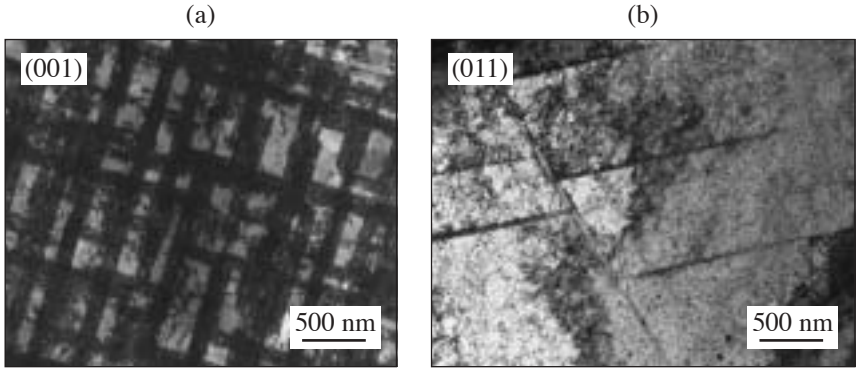

Figure 96.60
Transmission electron micrographs of a copper (2-wt%) aluminum sample irradiated with 200 J in a 2.5-ns pulse. The peak pressure in these samples was 40 GPa. (a) In copper (2-wt%) aluminum oriented to [001], four twin variants are observable at a high density; (b) in copper (2-wt%) aluminum oriented to $[\bar{1}34]$, two twinning variants are observable in considerably lower densities.

of laser light from the critical density. In past experiments the nonlinear coupling from different beams has been observed using the backscattered light as a diagnostic.[11]

Experimental and Modeling Studies of 2-D Core Gradients in OMEGA Implosions

Principal Investigator: R. C. Mancini (University of Nevada, Reno)

The objective of this program is to determine the spatially and temporally resolved two-dimensional (2-D) temperature and density core gradients of high-energy-density plasmas arising from OMEGA implosions. During the first year of the project substantial progress was made in the areas of instrument development, experiments, and data analysis.[12,13] One full OMEGA shot day was allocated, and nine shots were taken for this program. Two multi-monochromatic-imager (MMI) instruments were built and successfully fielded in indirect-drive implosion experiments on OMEGA. The plastic shells used in the experiments were filled with deuterium and doped with a tracer amount of argon for diagnostic purposes. The first imager operates in time-integration mode, while the second one records time-resolved images. For this second instrument, new (more-efficient) multilayer mirrors were designed and fabricated as well. With the availability of these additional instruments, simultaneous (i.e., in the same shot) recording of two sets of narrowband x-ray images of the core along two quasi-orthogonal directions perpendicular to the hohlraum axis is possible. This capability is critical for extracting information about the 2-D/3-D space structure of the core. A third imager has been tested in an effort to record a third set of narrowband images along a direction parallel to the hohlraum axis. Two series of five shots each were performed during FY03. In the first series, three types of beam pointing were tested that led to the production of round, "mild-sausage," and "sausage" implosion cores with a major axis along the hohlraum axis. In this way, it has been shown that a sequence of implosion cores can be produced where 2-D spatial structure effects are gradually "turned on." Processing the image data recorded in these implosions allowed the construction of 2-D emissivity maps associated to the argon He_β and Ly_β lines. Since the Ly_β to He_β emissivity ratio is a strong function of the temp-erature and a weak function of the density, Ly_β/He_β emissivity ratio maps were used to compute 2-D temperature maps of the core. Furthermore, 2-D scaled maps of the density were also obtained. Temperature and density maps show significant changes depending on the type of core, i.e., round, mild sausage, or sausage. In the second series of shots, time-resolved images were recorded.

The capsules used in both FY03 shot series were plastic shells filled with 50 atm of deuterium and doped with 0.1 atm of argon for spectroscopic diagnostic purposes. In addition to the x-ray imagers, time-resolved, space-integrated, argon *K*-shell x-ray line spectra were also recorded with the streaked SSCA or SSC1 crystal spectrometers in all shots. The line of sight (LOS) for these instruments was always through a laser entrance hole (LEH).

On the first series of shots, the focus was to record time-integrated images along two quasi-orthogonal directions close to the hohlraum midplane. In addition, a standard framing camera (XRFC2) was used to look at the implosion core down the hohlraum axis. A reference case of beam-pointing parameters was used to obtain round implosions (established in the team's previous NLUF project), and then the beams gradually moved (both cones, 2 and 3) in two steps of 30 μm each with the goal of driving mild-sausage and sausage implosion cores, i.e., ovals of gradually increasing eccentricity, with the major axis along the hohlraum axis. The results of the analysis clearly show the changes in core symmetry and spatial structure of the temperature and density distribution.

In the second shot series, the goal was to record time-correlated images and spectra with time resolution. Beam pointing was set to the reference case of round cores. MMI-3a (from the team's earlier NLUF project) and MMI-3b were mounted in TIM-2 and TIM-3, respectively, and SXRFC was mounted in TIM-4 (an SSCA was mounted in TIM-6); therefore, TIM-2, TIM-3, and TIM-4 defined a system of quasi-orthogonal *x*-*y*-*z* axes for these shots. Time-resolved data were successfully recorded with MMI-3b.

Progress in data analysis in FY03 focused on improving the capability of performing 1-D core gradient determination in round cores, and, in the first step, on developing and testing methods for extracting 2-D temperature and density spatial gradients from image data.

Figure 96.61 shows the results of 1-D core gradient determination for a round core. The gradients were extracted using a gradient reconstruction method that searches the parameter space of gradient functions with the goals of simultaneously and self-consistently fitting the spatial emissivity profile of the argon He_β line emission (obtained from a narrowband x-ray image) and the space-integrated argon line spectra covering the spectral range of the He_β, He_γ, and Ly_β lines and their associated Li- and He-like satellite transitions (i.e., multi-objective data analysis). The search in parameter space is

driven by a novel application of a niched-Pareto genetic algorithm (NPGA) to plasma spectroscopy. This algorithm is actually general and can be applied to other problems of multi-objective data analysis. The error bars are determined by taking into account solutions found in the vicinity of the optimal one, and by repeating the analysis for the same case considering the angle dependence of emissivity profiles, i.e., accounting for deviations from perfect spherical symmetry. Gradient uncertainties due to these effects are then added in quadrature. The consistency of these gradients with the emissivity spatial profile extracted from the analysis of the Ly_β image was also checked. Thus, these gradients are effectively constrained by three criteria: He_β and Ly_β emissivity spatial distributions and space-integrated line spectrum. Testing this capability in 1-D cases is important before extending them for application in 2-D problems.

An alternative method for temperature determination is based on the fact that the Ly_β/He_β emissivity ratio is a strong function of the temperature and a weak function of the density. Therefore, a space map of this emissivity ratio obtained by processing core image data can be directly transformed point by point into a space map of temperature. The temperature gradient determined by this method showed good consistency with the result obtained via the gradient reconstruction method.

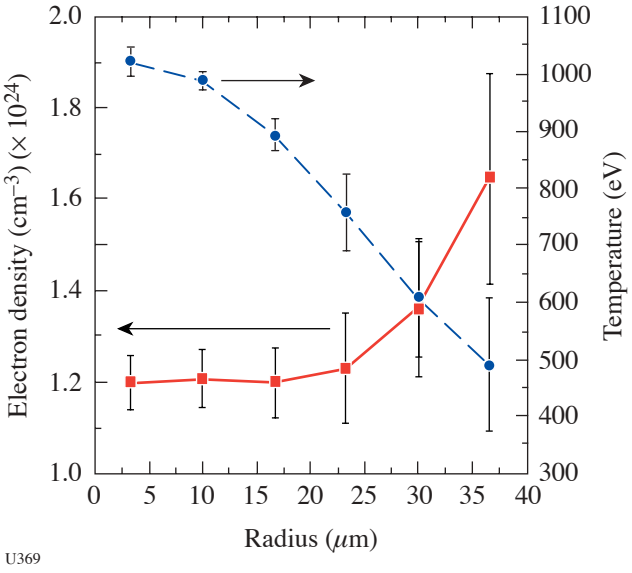

Figure 96.61
Results of 1-D core gradient reconstruction for OMEGA shot 26787.

In a first step toward determining the spatial distribution of temperature in the core beyond the 1-D approximation, the emissivity ratio method described in the previous paragraph was applied to the analysis of the image data recorded in the December 2002 shots. On shots 29885, 29889, and 29890, round, mild-sausage, and sausage cores were created intentionally (by adjusting the beam pointing) with the major axis along the hohlraum axis. Considering core slices cut perpendicular to the hohlraum axis and assuming axial symmetry (locally) in each slice, emissivity profiles in the core can be obtained from the He_β and Ly_β image data. This procedure can be interpreted as a generalized Abel inversion. Next, the Ly_β/He_β emissivity ratio maps were interpreted and directly converted into 2-D (actually, quasi-3-D) spatial maps of core temperature. Results obtained for these three shots are displayed in Figs. 96.62–96.64. The hohlraum axis is along the vertical direction. The characteristic size of these implosion cores is 60 to 80 μm. Changes in core symmetry and temperature spatial distribution are apparent from the maps.

After the temperature map has been determined, scaled density maps can be obtained by working separately with each line emissivity map (He_β or Ly_β) and solving point by point for the density given the local values of emissivity and temperature. These results are also shown in Figs. 96.62–96.64. Note that the density maps extracted from the He_β emissivity are not identical to those extracted using the Ly_β emissivity; however, they are very similar, suggesting that the process is sound. Again, changes are observed from round to sausage cores. In particular, a two-peak density (and temperature) spatial structure develops for the mild-sausage and sausage implosion cores along the major axis.

Finally, Fig. 96.65 shows the time-resolved data obtained in OMEGA shot 31594 (May 2003) with MMI-3b. Round-core beam pointing was used in this shot. Each frame is characteristic of a 50-ps time interval and displays simultaneous core images and a slit spectrum. Both images and spectra data show significant changes as a function of time that are being used to study the time evolution of the core's spatial structure. Work is in progress in the analysis of these data.

FY04 will focus on (1) obtaining time-resolved data for studying the 2-D spatial structure of round, mild-sausage, and sausage implosion cores, (2) contining work on alternative generalized Abel-inversion procedures, (3) applying 2-D gradient reconstruction methods to determine the spatial structure of implosion cores, and (4) performing detailed comparisons between data analysis and hydrodynamic simulation results.

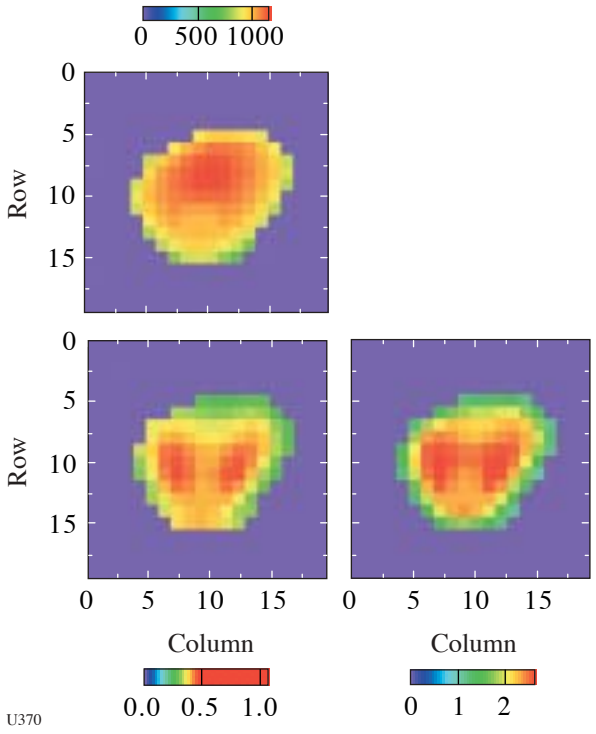

Figure 96.62
Time-integrated 2-D electron temperature (top, in eV) and scaled electron-density maps (bottom, in units of 1×10^{24} cm^{-3}) for OMEGA shot 29885, round implosion core case. Electron-density maps (left) based on He$_\beta$ emissivity and (right) based on Ly$_\beta$ emissivity.

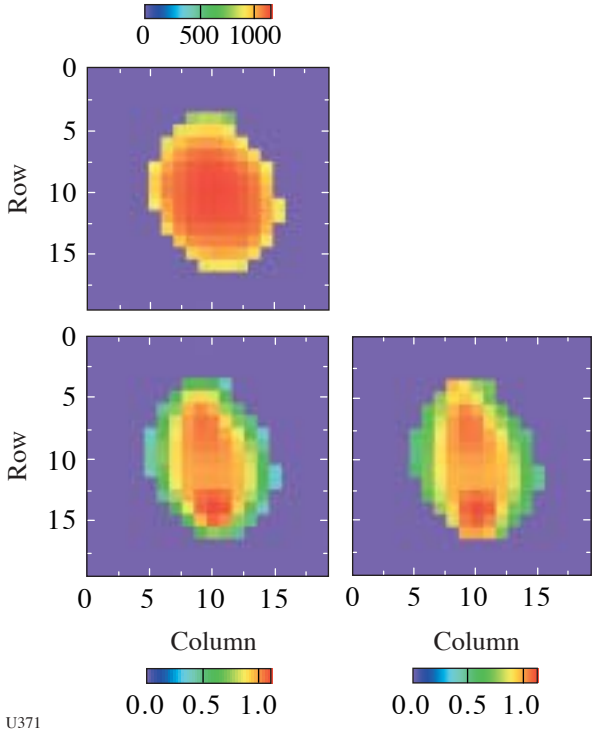

Figure 96.63
Time-integrated 2-D electron temperature (top, in eV) and scaled electron-density maps (bottom, in units of 1×10^{24} cm^{-3}) for OMEGA shot 29889, mild-sausage implosion core case. Electron-density maps (left) based on He$_\beta$ emissivity and (right) based on Ly$_\beta$ emissivity.

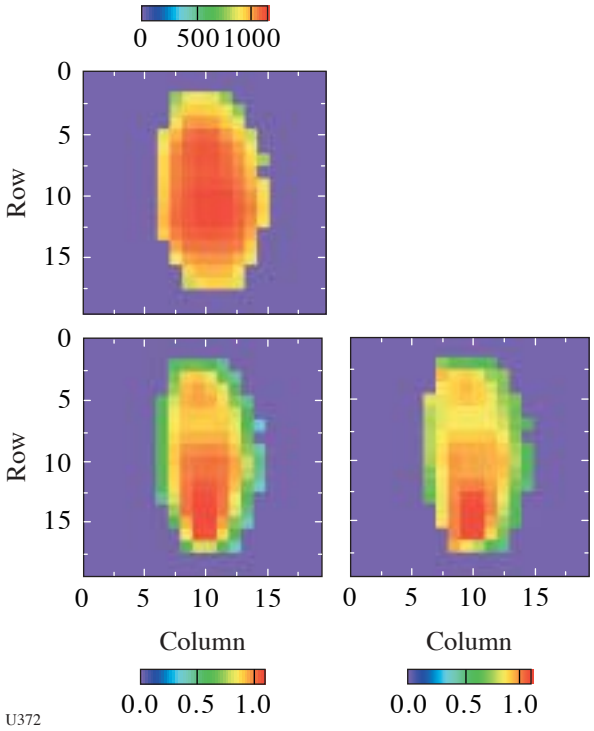

Figure 96.64
Time-integrated 2-D electron temperature (top, in eV) and scaled electron-density maps (bottom, in units of 1×10^{24} cm^{-3}) for OMEGA shot 29890, sausage implosion core case. Electron-density map (left) based on He$_\beta$ emissivity and (right) based on Ly$_\beta$ emissivity.

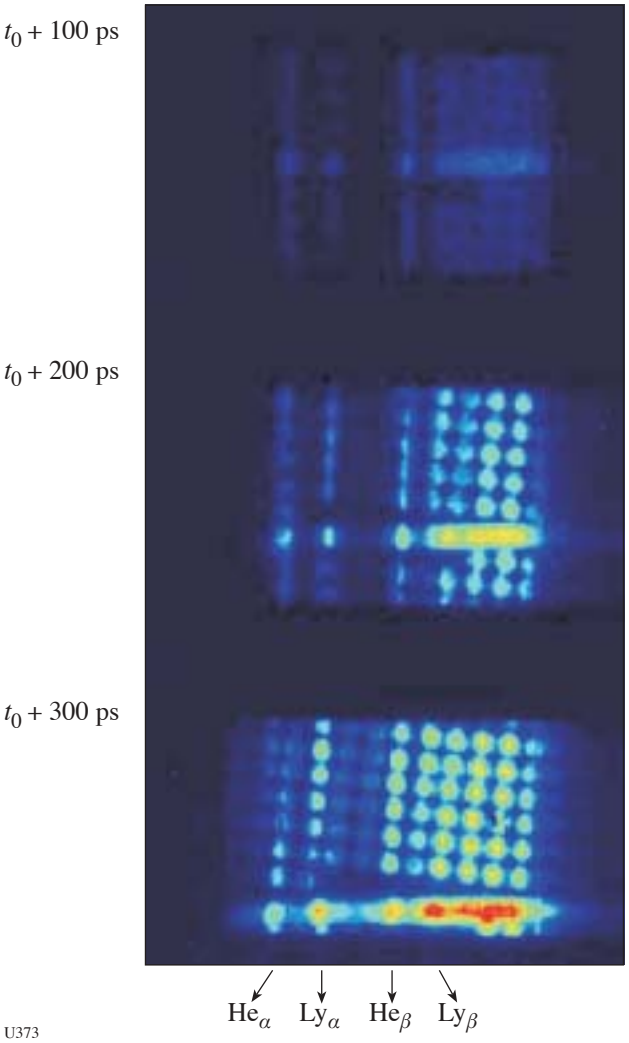

Figure 96.65
Time-resolved core images and slit spectrum recorded in OMEGA shot 31594 with MMI-3b.

Recreating Planetary Core Conditions on OMEGA: Techniques to Produce Dense States of Matter

Principal Investigator: R. Jeanloz (University of California, Berkeley)

The objective of this program is to use OMEGA to determine the nature of planetary fluids at the extreme conditions representative of the cores of the giant planets. To achieve the required conditions, this team has developed diamond anvil cell (DAC) targets for laser shock-compression experiments. With this technique the initial sample pressure is much higher than ambient (3 to 20 kbar), and the initial density may be from 1.5 to 5 times higher than ambient (depending on the sample) compared to nonpressurized preparation methods. The higher initial density results in a significantly larger final density and lower temperature in the shock-compressed state. Single- and multiple-shock Hugoniot techniques of precompressed targets can re-create deep interior states of giant solar planets, extrasolar planets, and low-mass stars.

In FY03, 1.5 shot days were allotted to this program, and 15 target shots were performed on precompressed samples (hydrogen, helium, and nitrogen) on the OMEGA laser. As shown in Fig. 96.66, a thin (≤200-μm) drive diamond was laser-ablated to send a shock through the sample (~100 μm thick) loaded in a DAC. The primary diagnostic was the velocity interferometer system for any reflector (VISAR). Table 96.VII lists the first ten target shots of FY03.

Highlights of the experiments are shown in Fig. 96.67, which shows the results of shot #31455: helium precompressed to 5.5 kbar. The sample remained transparent with a particle velocity of approximately 2 μm/ns. (It is likely that the laser was misaligned and the observed pressure was much lower than expected based on the incident energy.) Figure 96.68 shows the results for shot #30758: helium precompressed to 2.7 kbar. As in three other shots, one can see the shock breakout into the helium sample but the helium was nontransparent. Figure 96.69 shows the results for shot #30759: hydrogen precompressed to 3.6 kbar. The sample was nontransparent (transparent at the edges, where edge rarefaction has sufficiently lowered the pressure). At times after breakout of about 8 and 12 ns, re-shock and rattling of the shock into a more-reflective state were observed. The pressure of this shock is estimated to have been about 420 kbar with a re-shock pressure

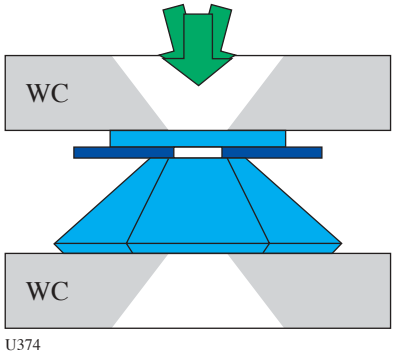

Figure 96.66
Illustration of diamond anvil cell (DAC) geometry. Tungsten carbide (WC) is used as a support for the DAC.

of about 1.1 Mbar. Figure 96.70 shows the results of shot #31457: nitrogen precompressed to 5.2 kbar. In this shot the nitrogen shock was reflecting, showing a strong decay in shock velocity from about 24 to 19 μm/ns. When the shock hit the back diamond, the VISAR fringes suddenly disappeared due to the diamond window going opaque (consistent with a diamond shock pressure above about 1.5 Mbar). The spatial extent of the shock reflectivity implied that the radius of curvature in this shot was 300 to 400 μm, consistent with the use of 300-μm phase plates.

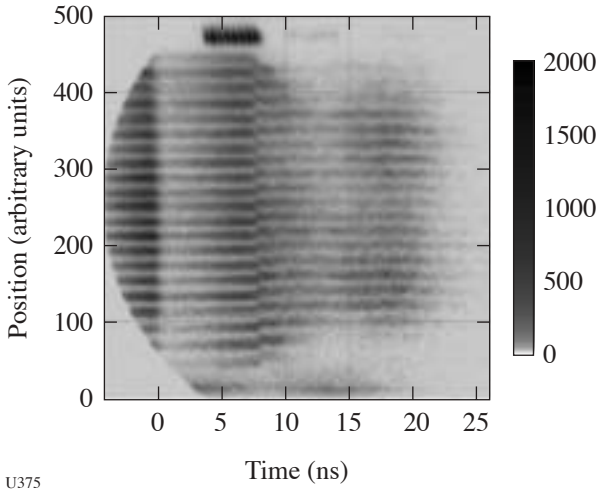

Figure 96.67
VISAR data from shot #31455: He precompressed to 5.5 kbar.

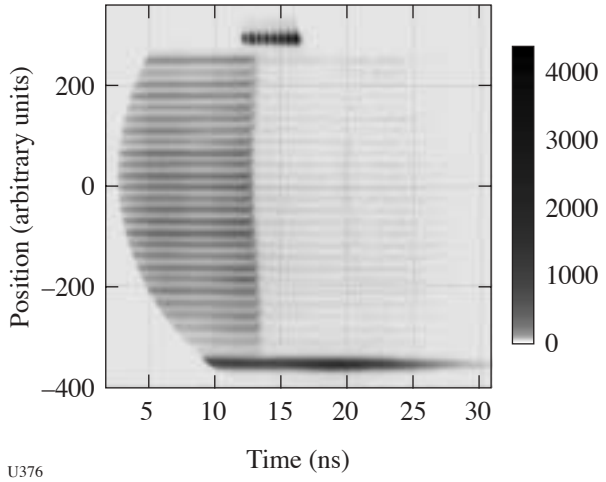

Figure 96.68
VISAR results from shot #30758: He precompressed to 2.7 kbar.

Table 96.VII: Target shots to explore planetary core conditions on OMEGA—the first ten shots of FY03.

LLE Shot #	Sample	Initial Pressure (kbar)	Initial Density (g/cc)	Laser Intensity (W/cm^2)	Results
30755	He	5.4	0.301	6.5×10^{14}	Opaque diamond
30756	He	5.4	0.301	5.2×10^{14}	Opaque diamond
30757	Surrogate	—	—	5.2×10^{14}	—
30758	He	2.7	0.211	5.1×10^{13}	Nontransparent
30759	H_2	3.6	0.127	4.5×10^{13}	Nontransparent
31454	He	1.6	0.154	5.3×10^{14}	Nontransparent
31455	He	5.5	0.304	2.7×10^{14}	Transparent
31456	H_2	6.2	0.142	2.7×10^{14}	Nontransparent
31457	N_2	5.2	0.935	4.1×10^{14}	Reflecting
31459	He	5.9	0.314	2.6×10^{14}	Nontransparent

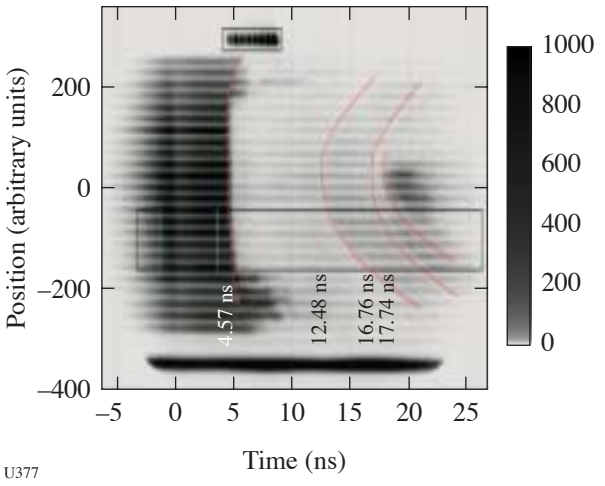

Figure 96.69
VISAR results of shot #30759: H_2 precompressed to 3.6 kbar.

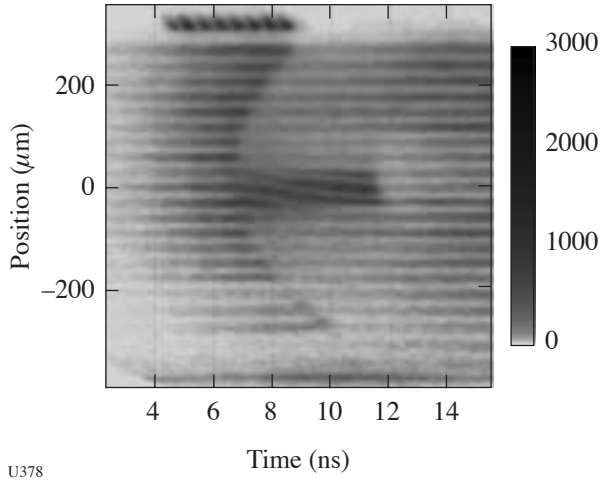

Figure 96.70
VISAR results from shot #31457: N_2 precompressed to 5.2 kbar.

After the shock leaves the sample, it travels through a 1.2-mm-thick single-crystal diamond cut in the (100) direction. Under weak shock loading, it is found that the diamond shears along four equivalent (111) planes, leaving a distinct fourfold symmetric fracture on the diamond table (Fig. 96.71). Considering the diamond's thickness, the shock assumes a somewhat spherical front so that the shock travels in different crystallographic directions within the diamond. It is reasonable to expect that the shock velocity, and hence the shock intensity, will reflect the symmetry of the diamond lattice. In fact, evidence of this symmetry breaking was observed by examining the recovered and deformed tungsten carbide support. When the tungsten carbide remained intact under strong shock loading, the deformation was not uniform, adopting a fourfold symmetry often characterized by a series of steps or "terraces" (Fig. 96.72). These terraced indentations occur where shear fractures along different (111) planes intersect, suggesting regions of greater stress in the diamond crystal (Fig. 96.73). It is noted that the fourfold symmetric strain cannot be caused by the tungsten carbide itself since it is amorphous and has no intrinsic fourfold symmetry.

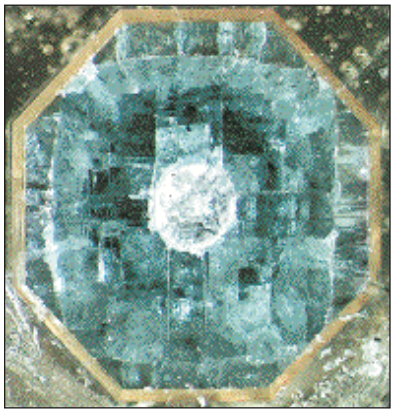

Figure 96.71
Photograph of diamond table showing central spall and four-fold shearing along (111) planes.

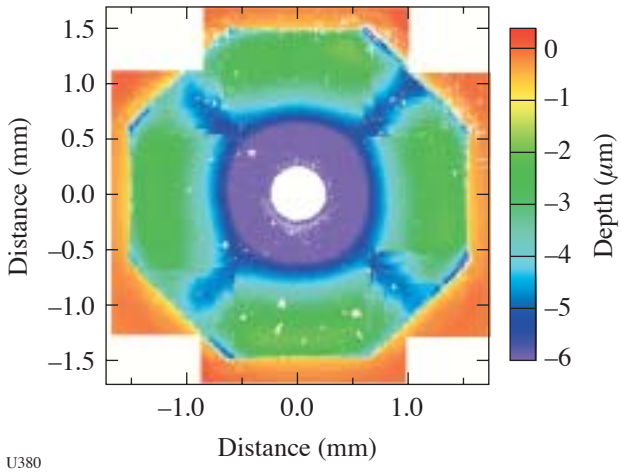

Figure 96.72
Depth profile of tungsten carbide support.

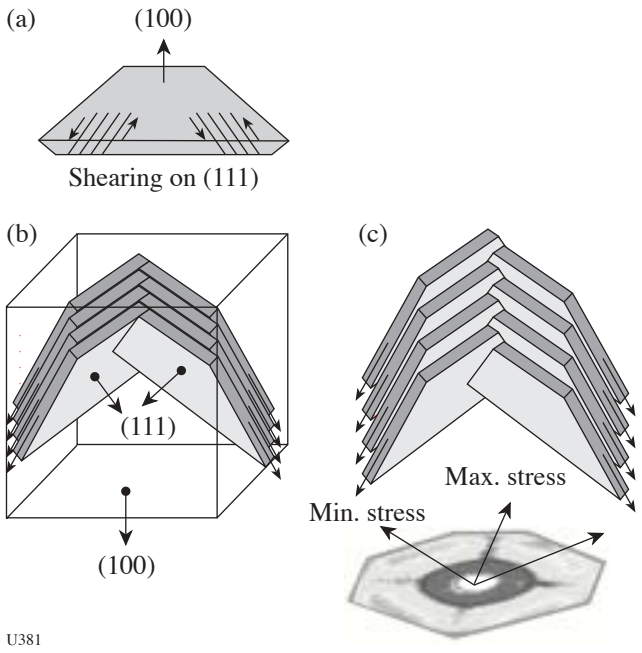

Figure 96.73
Illustration of shearing mechanism and relation to the plastic deformation in the tungsten-carbide backing plate.

During the second year of this study, the experiments will focus on determining the reflectivity transition and pressure–density equation-of-state measurements in hydrogen, helium, and nitrogen at several precompression pressures. New experimental approaches will also be developed to employ higher precompression pressures above 100 kbar so that regions of phase space can be accessed where exciting new predictions for the hydrogen phase diagram have been made, including a first-order dissociation in the liquid and a negative Clapeyron slope for the melt line at high pressures. Studies of the recovered material from the samples, to investigate expected phase changes such as the formation of graphite, amorphous carbon, and crystalline tungsten carbide, as well as searches for any new unpredicted phases, will continue.

FY03 LLNL OMEGA EXPERIMENTAL PROGRAM*

In FY03 Lawrence Livermore National Laboratory (LLNL) continued to be a major user of OMEGA. LLNL's 390 experimental shots can be divided into two groups: those in support of the inertial confinement fusion (ICF) program and those in support of high-energy-density sciences (HEDS), which include materials, equation-of-state, and physics experiments.

ICF Experiments

The ICF program on OMEGA in FY03 totaled 152 shots. Highlights of these experiments include the following:

Charged-Particle Spectroscopy (CPS): These implosions, done in collaboration with MIT, measured the charged fusion reactions produced from indirectly driven ICF implosions. Initial experiments ascertained the feasibility of using multiple CPS diagnostics as a measure of implosion asymmetry.

X-Ray Thomson Scattering: These shots showed that He- and H-like Ti x rays can be spectrally measured after scattering off near-solid-density plasmas. Theoretical fits to the data are in good agreement, opening the way for using this as a diagnostic for pusher ρR on National Ignition Facility (NIF) implosions.

Cocktail (Mixtures of Materials) Hohlraums: These experiments were performed to attempt to measure a predicted improvement in x-ray conversion efficiency and soft-x-ray albedo. Preliminary results seem to verify the latter, but not the former.

Planar Rayleigh–Taylor: A series of experiments were performed on polyimide targets to assess its usefulness as an ablator for ICF capsules. The data to date indicate a higher RT growth rate than calculated, even though acceleration measurements seem to match predictions.

Technique Development: A number of experimental techniques expected to be used on the NIF were tested with OMEGA shots. These included high-magnification x-ray imaging of imploded capsules, using target-mounted pinholes (Fig. 96.74), and development of a Kirkpatrick–Baez (KB) x-ray microscope with a spectrally narrow bandpass to look at x-ray line emission from a backlighter through a capsule. Additional experiments, done in collaboration with the University of Nevada–Reno, investigated spatially resolved spectroscopic measurements of pusher density using a Ti dopant within the inner layer of the capsule, while using Ar x-ray emission from the fuel region to deduce temperatures and densities in that region (Figs. 96.75 and 96.76).

*Acknowledgment: This work was performed under the auspices of the U.S. Department of Energy by University of California Lawrence Livermore National Laboratory under contract No. W-7405-Eng-48.

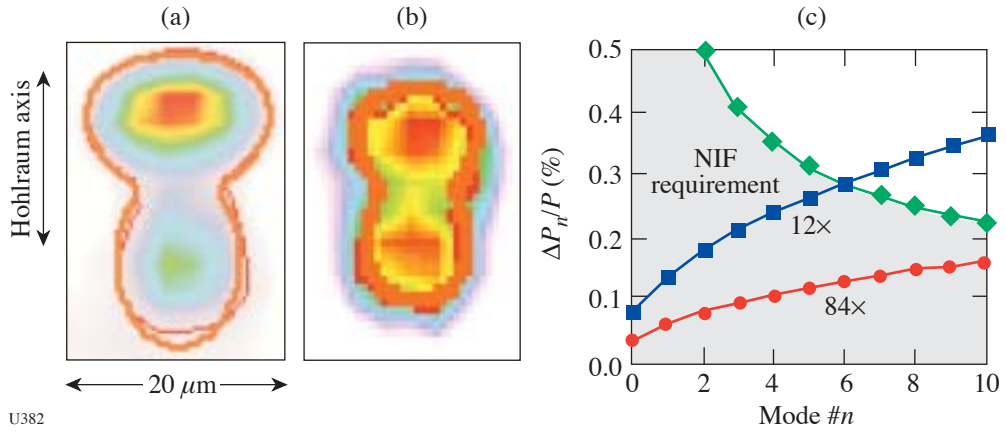

Figure 96.74
Examples of x-ray images taken with target-mounted pinholes of 5-μm aperture at a magnification of (a) 87× and (b) 12×. The resolution requirements of NIF targets are shown in (c) and compared to the achievable resolution of a 12× and 84× imaging system on the NIF.

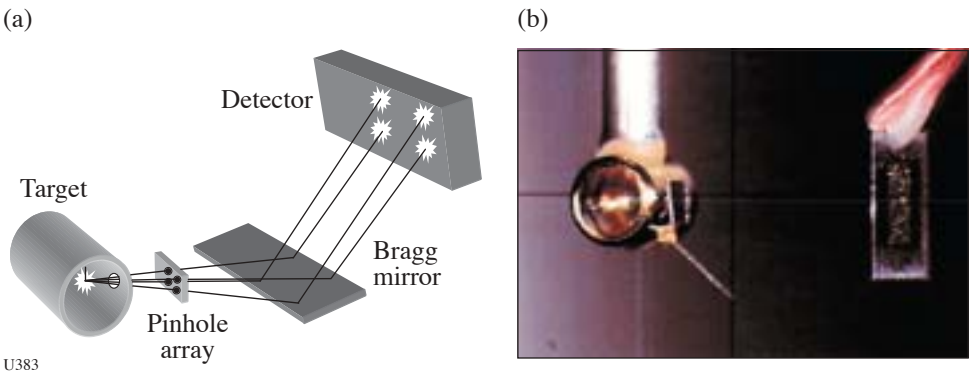

Figure 96.75
Illustration of a multi-monochromatic imaging (MMI) system based on an LLE-developed technique. Several MMI systems have been fielded for both LLNL and NLUF experiments on OMEGA: (a) schematic of MMI diagnostic illustrating the concept; (b) photograph of typical configuration used on hohlraum-driven experiments on OMEGA. Each device produces hundreds of 11-μm-resolution images. Spectral dispersion is achieved by a depth-graded WB_4C multilayer mirror with an energy resolution of ~75. The devices typically cover the energy range of 3 to 5 keV.

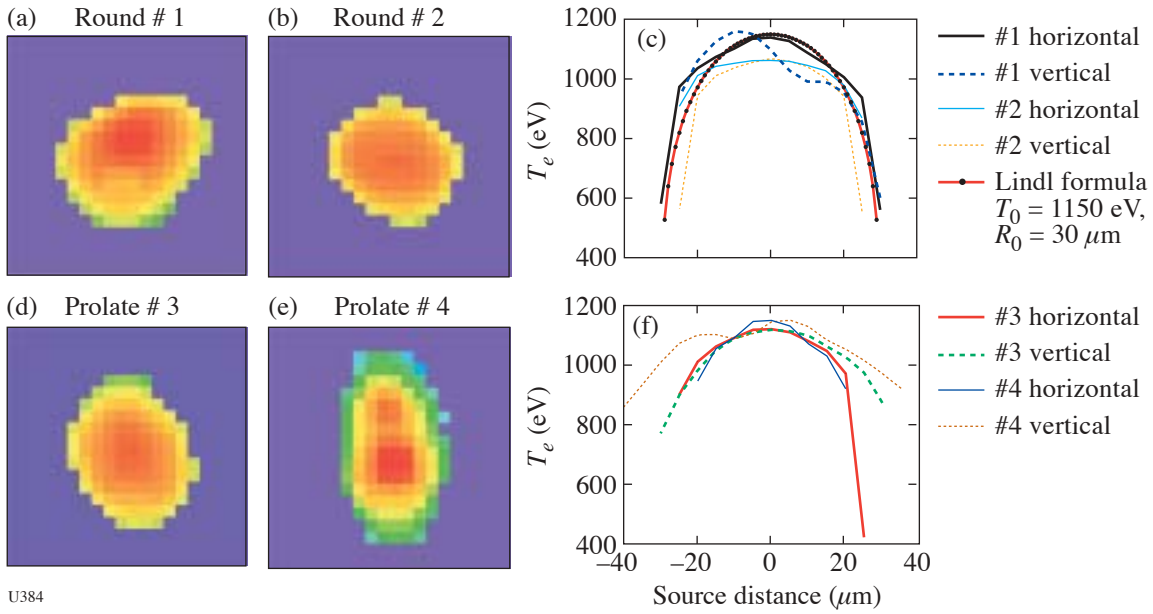

Figure 96.76
Inferred temperature maps taken on hohlraum-driven implosions of D_2-filled, Ar-doped capsules: (a), (b) 2-D temperature profiles, and (c) radial lineout of relatively round implosions; (d), (e) 2-D temperature profiles, and (f) radial lineout of prolate implosions.

Laser–Plasma Interaction: Laser–plasma interaction (LPI) experiments were carried out to explore the interaction of the laser with the large plasmas created when gas-filled hohlraums are used. Most of these experiments used gas bags as the initial target to provide a long-scalelength plasma with good diagnostic accessibility. Experiments measured Raman (SRS) and Brillouin (SBS) scattering levels, the effect of Langmuir damping, and energy exchange through SBS in crossed-beam experiments. The 4ω probe beam was successfully used for Thomson-scattering measurements, as shown in Fig. 96.77. Additional experiments in gas-filled hohlraums investigated the effect of gas pressure on capsule hydrodynamics and possible enhanced gold–gas mixing due to preroughened hohlraum walls. Still another experiment searched for evidence of early-time laser light directly striking the capsule in indirect-drive experiments. These results are compared to calculations in Fig. 96.78.

Several high-yield, direct-drive DT implosions were carried out in collaboration with LANL to provide high fluxes of 14-MeV neutrons for diagnostic development. The characteristics of a photoconductive diamond (PCD) device in measuring neutrons is shown in Fig. 96.79. At high neutron flux, the impedance of the transmission line (Z) causes saturation at $I_{max} = V/Z$.

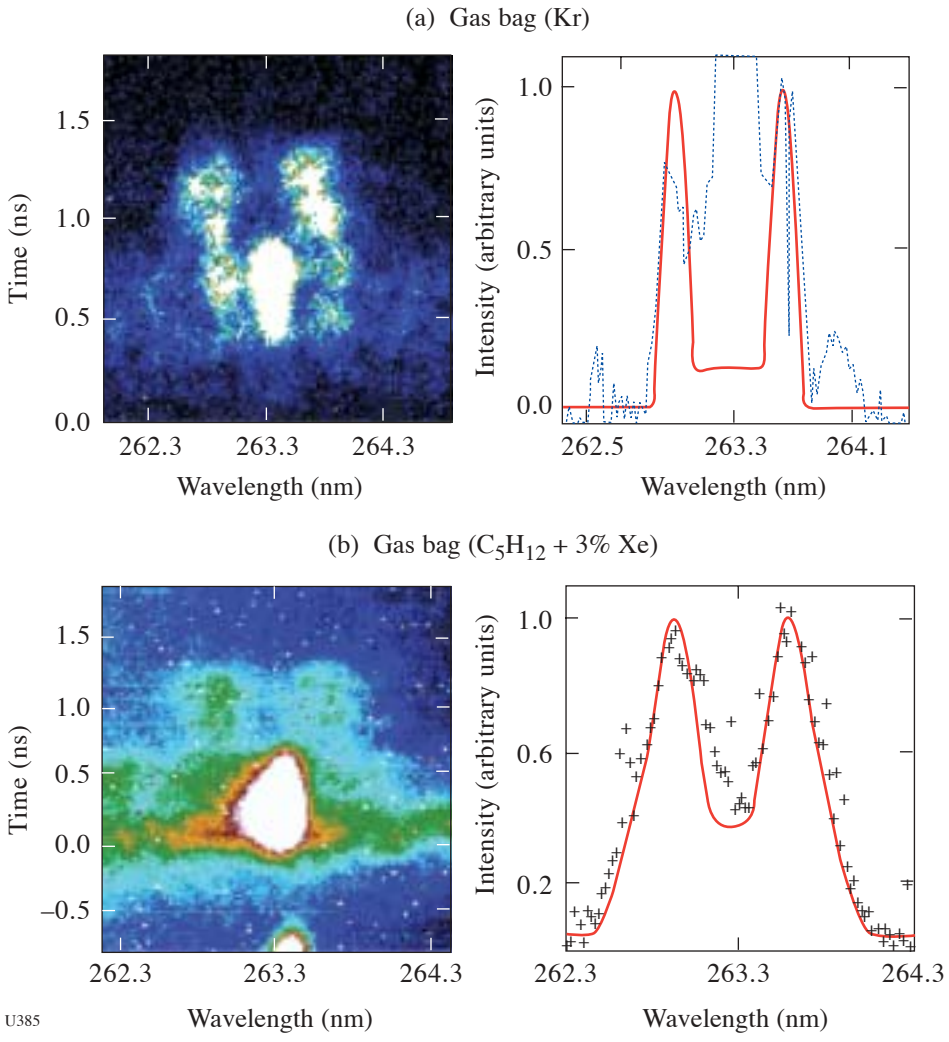

Figure 96.77
Illustrations of 4ω Thomson-scattering measurements on laser–plasma interaction experiments: (a) streaked record of Thomson-scattering signal from a Kr-filled gas-bag target; (b) streaked record of Thomson-scattering signal from C_5H_{12}–3%Xe–filled gas bag. While the heater beams are on, these measurements show an electron temperature of ~3.2 keV for the Kr-filled gas bag. The C_5H_{12}–3%Xe–filled gas shows an electron temperature of 1.5 keV late in time.

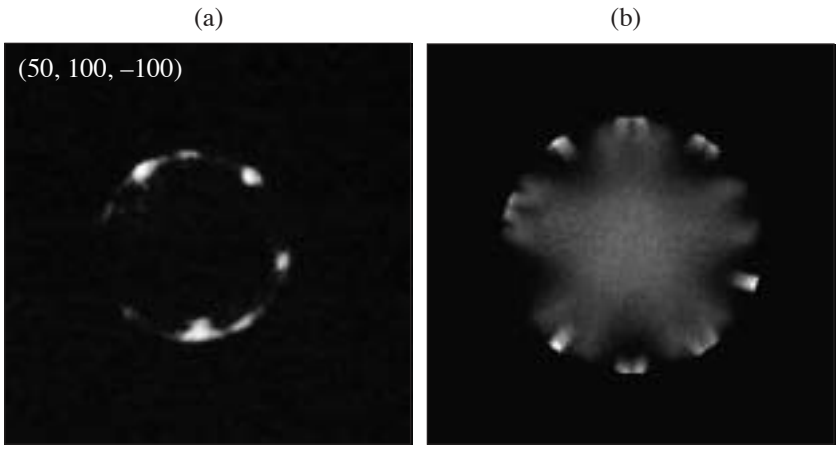

Figure 96.78
X-ray re-emission images are used to search for evidence of early-time laser light directly striking the capsules: (a) actual image; (b) experimental simulated image.

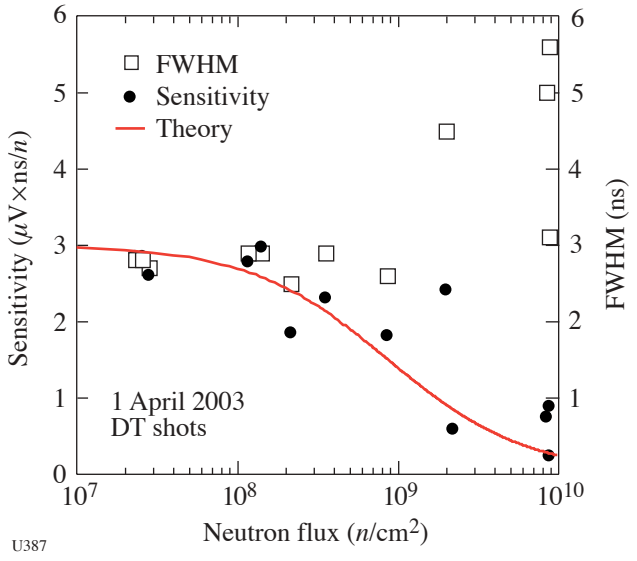

Figure 96.79
Experimental measurements of the sensitivity and full width at half maximum of the signal generated by a diamond detector in response to increasing neutron flux obtained from OMEGA experiments. The theoretical curve is from the x-ray work of Kania *et al.*[14]

HEDS/NWET Experiments

The High-Energy-Density-Science and Nuclear Weapons Effects Testing (NWET) Programs used 238 laser shots on OMEGA during FY03. Some of the experiments included the following:

IDrive: A substantial number of shots ("IDrive") were devoted to developing techniques for measuring material properties when subjected to substantial pressures, but still in the solid state. Low-temperature Rayleigh–Taylor experiments were performed with this experimental arrangement (Fig. 96.80).

NEL Preparation: Another large group of shots were devoted to using OMEGA to prepare for NIF early-light (NEL) experiments. These included testing concepts for point-projection backlighting using backlit pinholes as an x-ray source. An example of this work in Fig. 96.81 shows an excellent radiographic image of a propagating shock.

EOS Experiments: Equation-of-state (EOS) experiments were performed in a variety of materials by measuring the velocity of ablatively driven shocks within the material. LLNL is a major participant in an NLUF experiment that measured shock velocities through precompressed gases within diamond anvil pressure cells, as shown in Fig. 96.82. Shock experiments were also used to measure opacities at elevated pressures and temperatures.

Hot Hohlraums: Experiments were conducted with small hohlraums to develop sources at elevated radiation temperatures.

Convergent Rayleigh–Taylor: Rayleigh–Taylor instabilities were studied in a spherically convergent geometry, using pre-imposed perturbations on spherical capsules.

Double-Shell Capsules: Double-shell (one shell containing DD fuel within another, concentric, indirectly driven shell) targets were explored for a number of properties, including their sensitivity to high-energy photon preheat, and the timing of the fuel shock heating compared to the timing of the fuel compression.

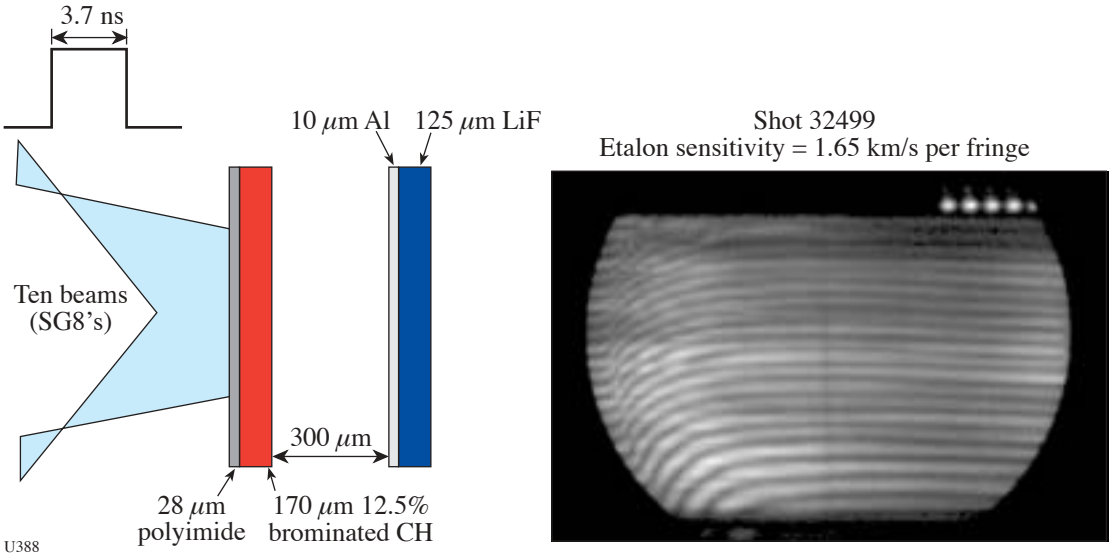

Figure 96.80
VISAR record on IDrive shot #32499 showing that smooth loading was achieved with no instabilities.

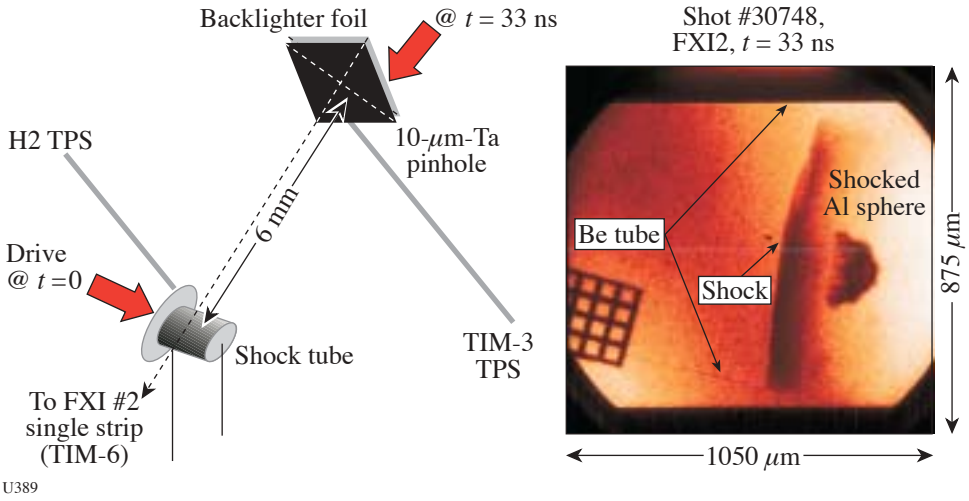

Figure 96.81
Illustration of the application of point backlighting to characterize the interaction of a shock with a spherical object.

Radiation Propagation: A number of experiments looked at the propagation of radiation in low-density materials.

Dynamic Hohlraum: Another experiment looked at the possibility of using a direct-drive configuration to create a dynamic hohlraum for driving implosions.

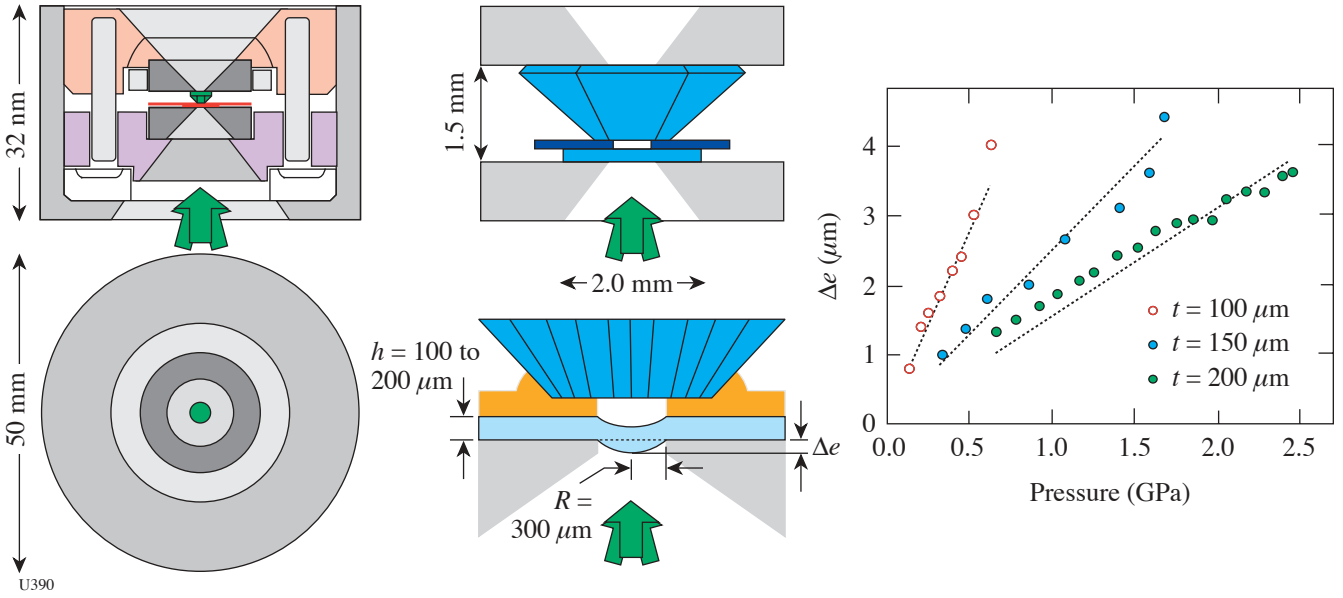

Figure 96.82
Experimental setup for an OMEGA equation-of-state experiment using a diamond anvil cell filled with a precompressed gas (such as hydrogen).

FY03 LANL OMEGA EXPERIMENTAL PROGRAMS

The Los Alamos National Laboratory (LANL) series of experiments on OMEGA in FY03 emphasized research into hydrodynamic instabilities, mix, material properties, neutron diagnostic development, and radiographic technique development for the Nation's inertial confinement fusion and stockpile stewardship missions.

Cylinder Implosions: One phase of the hydrodynamic instability experiments investigates the Richtmyer–Meshkov instability (RMI) in a convergent, compressible, miscible plasma system in the presence of strong shocks.[15] Fifty of the 60 OMEGA lasers illuminate small, hollow, epoxy cylinders with 18 kJ of energy. The center cylinder is filled with low-density foam. A very thin aluminum marker layer is placed between the foam and the epoxy. The laser energy heats the epoxy cylinder to extreme temperatures, causing approximately one-half of it to vaporize and expand outward (away from the axis), while the other half is pushed inward (implodes) by a strong shock wave. The passage of the shock wave through the target assembly heats the target materials and causes them to become plasmas. As a result, the interfaces along both sides of the marker band are accelerated, and the materials mix over time. The danger of RMI is that in an ignition capsule, if the mixing becomes severe enough, fusion reactions end and thermonuclear ignition—the ultimate goal of all ICF experiments—fails. To measure the amount of mixing, five additional OMEGA laser beams strike an iron foil at one end of the cylinder after a small time delay. X rays are emitted, travel lengthwise through the cylinder, are imaged by a pinhole, and are recorded by a framing camera.

In a basic experiment conducted this year, a simple sinusoidal perturbation was machined into the outside of the aluminum marker layer, creating a corrugated surface with the corrugations running the length of the cylinder.[16] It was hypothesized that these perturbations would grow due to the convergence of the system and the shock-driven RMI. Furthermore, it was expected that the growth rate of the perturbations would change for different numbers of perturbations. Measurements were made with targets that had 8, 16, or 28 perturbations machined into them (Fig. 96.83). As can be seen in the

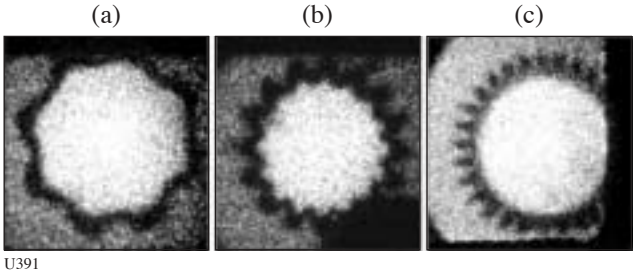

Figure 96.83
Axial radiographs of single-mode sinusoidally perturbed targets with mode numbers of (a) 8, (b) 16, and (c) 28. The dark band is the radiographically opaque aluminum marker layer.

figure, the amplitude of the corrugations at the outside of the marker layer is approximately the same in each case.

Asymmetric Direct-Drive Spheres: The asymmetric direct-drive spheres (ADDS) experiment tests the hypothesis that asymmetric implosions create more mixing of the shell material into the fusion fuel than do symmetric implosions. These directly driven 1100-μm-diam capsules were made of Si-GDP glass and filled with various pressures of DT. The convergence ratio was adjusted by varying the gas-fill pressure. The degree of asymmetry was varied from oblate to symmetric to prolate by adjusting the energy in each individual laser beam to make the correct overall pattern on the capsule.

This year, higher convergence implosions were conducted by reducing the fill pressure to 2.5 atm. These experiments had more mix than previously observed with 10 or 15 atm of gas fill. Figure 96.84 shows an x-ray image of a prolate implosion taken by the GMXI. Shell material can be seen all the way to the center. The yield was less affected by asymmetry in this experiment than it was with the 5 or 10 atm of gas fill.

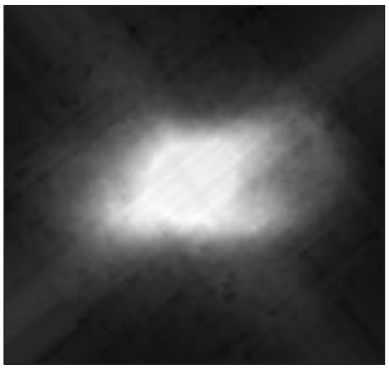
U392

Figure 96.84
A GMXI x-ray image of a prolate implosion showing that shell material has reached the core of the imploding capsule.

Neutron Diagnostics Development: In collaboration with Lawrence Livermore National Laboratory, symmetric implosions of DT-filled capsules aided the development of the carbon-vapor–deposited (CVD) diamond detector and the palm-top LANSA. These experiments also supported further development of the pinhole-based neutron imaging technique.

Double-Shell Targets: Direct-drive double-shell targets may provide an alternative, noncryogenic path to ignition on the National Ignition Facility (NIF).[17] Experiments are being pursued on OMEGA to understand the hydrodynamics of these implosions and the possibility of scaling them to NIF designs. The double-shell campaign examines the effect of drive, externally applied radiative preheat and foam composition on the implosion hydrodynamics, and the growth of mix due to hydrodynamic instabilities in a spherical geometry. Marker layers are implanted strategically in the capsule, and low-resolution radiography has been used to measure the zero-order hydrodynamic evolution of the capsule.

Twenty of the OMEGA laser beams were needed for backlighting, leaving only 40 beams to drive a symmetric implosion. The pointing of the remaining beams was offset from the center of the capsule to achieve a symmetric implosion. Radiographs were obtained from two different directions at multiple times with uniform area backlighting. A typical radiograph of a symmetric implosion is shown in Fig. 96.85. Neutron implosion data was also obtained simultaneously.

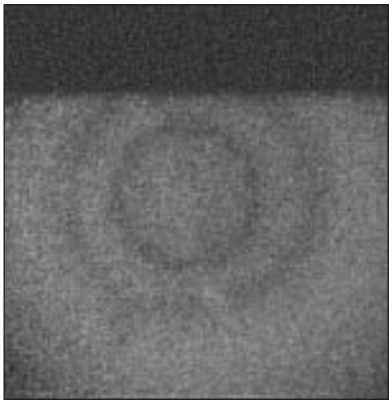
U393

Figure 96.85
A radiograph of a double-shell implosion target 1.7 ns after the beginning of the laser beams. The inner and outer shells and the intershell foam are clearly evident.

Supersonic Jet: In recent years we have fielded numerous supersonic-jet experiments[18] on OMEGA in a collaboration between Los Alamos National Laboratory, the Atomic Weapons Establishment, Lawrence Livermore National Laboratory, the University of Michigan, and the Laboratory for Laser Energetics. These experiments help validate our next-generation radiation-hydrodynamic codes. One of the outstanding questions is whether these types of jets should become turbulent, given their high Reynolds number. We have recently modified our experiments to have more Kelvin–Helmholtz shear, to run much later in time, and to increase the chance of going turbulent. To diagnose these large (several-millimeter) jets at very late times (100 to 1000 ns), we are developing

pinhole-apertured point-projection x-ray imaging (PAPBL) using an x-ray energy of about 5 keV.

This year's experiments have concentrated on validating a new target design and overcoming technical problems arising from the PAPBL imaging technique. High spatial resolution over a large field of view was demonstrated, and recent work has given unequivocal evidence of a jet in late-time radiographs. The experiment consists of a directly driven titanium "slug" that impacts a low-density foam. The jet of titanium formed in the carbonized-resorcinal-formaldehyde (CRF) foam is diagnosed by point-projection radiography.

Significant progress was made this year in utilizing pinhole-apertured x-ray point backlighting. Adequate backlighter intensity was obtained by using two laser beams (400 J per beam, 1-ns pulse length). Figure 96.86 shows a pinhole-aperture point-projection radiograph from the region of the resolution grid from a static-target experiment. Best fit to the experimental data is obtained by convolving a 15-μm FWHM Gaussian point-spread function with the ideal, theoretical grid transmission. This spatial resolution is comparable to that obtained in our previous pinhole-imaging experiments. The field of view of the earlier experiments was limited, however, to approximately 500 μm by the area-backlighting source, whereas that of the present point-backlit experiment covers approximately a 4-mm field of view. This represents a very significant potential increase of "information content" in comparison with the earlier work.

The new target design with PAPBL imaging successfully recorded clear evidence of the jet and the surrounding bow shock in the CRF foam (Fig. 96.87). Extensive design calculations for these experiments have been carried out at LANL

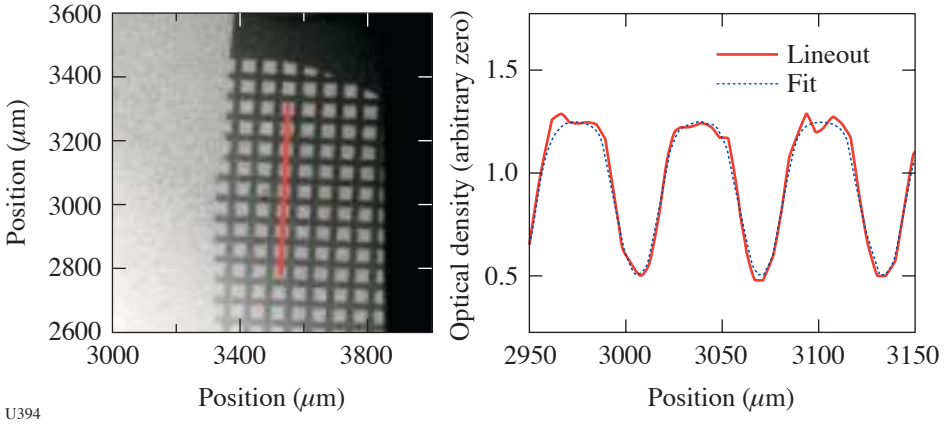

U394

Figure 96.86
Pinhole-aperture point-backlighter image of a static (not-driven) target. Best fit to the transmission of the image of the resolution grid is obtained when the ideal grid transmission is convolved with a 15-μm FWHM Gaussian spatial-resolution function.

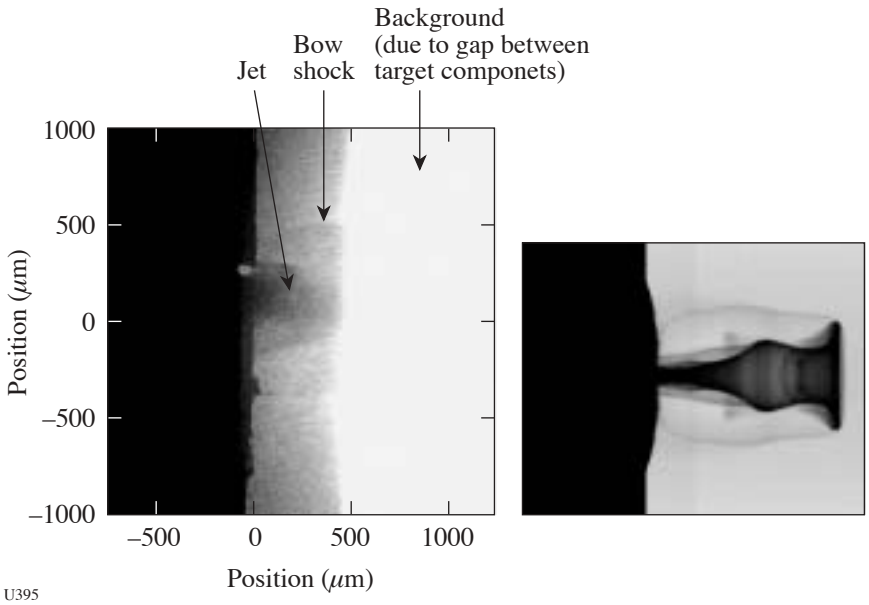

U395

Figure 96.87
Pinhole-aperture point-projection radiographic image of the titanium jet and bow shock in CRF foam and an NYM-PETRA simulation (shown at the same spatial scale). The experimental image is partially overlaid by background emission from the target, arising from an unintentional gap between target components.

using the *RAGE* code, and at AWE using the NYM and PETRA codes. Figure 96.87 also shows a simulated radiograph generated by NYM-PETRA. Careful analysis of the experimental images from our most-recent run indicates that the data in Fig. 96.87 are partially obscured by a region of emission resulting from an unintentional gap between the gold shield and titanium washer of the experimental package. A silver-loaded epoxy fillet, or modified shield design, would presumably reduce this problem in future experiments.

Time-Dependent Mix: The goal of the time-dependent mix experiment is the production of high-quality, time-resolved spectroscopic and imaging data that will constrain models of fuel–pusher mix in directly driven ICF implosions. The primary diagnostic marker is a thin (0.1-μm-thick) titanium-doped CH layer introduced at the fuel–pusher interface of an ICF capsule. The timing and intensity of emission from H-like Ti have been calculated to depend on the timing and amount of Ti that reaches the center of the fuel. In the first experiments, high-quality, time-resolved Ti *K*-shell spectroscopic data were obtained from targets that had a range of shell thicknesses and fill-gas pressures. The high quality of the data indicates the viability of this approach.

X-Ray Backlighting: Los Alamos also developed an x-ray-backlighting technique at 9 keV that produces uniform, large-area, monochromatic, high-resolution images of targets used for laser-driven AGEX and high-energy-density-physics (HEDP) experiments. X-ray imaging at moderate energy in laser-driven HEDP experiments is an essential, well-established tool for observing dynamic phenomena such as shock trajectories, interface motion, and instability growth. However, the standard technique using an area backlighter, coupled with the size of the object to be radiographed, requires an inordinate amount of laser energy to produce a monochromatic x-ray source above 7 keV.

High-resolution images were obtained using a pinhole-apertured point-backlighter (PAPBL) geometry and a Zn source. Figure 96.88(a) shows the raw image, recorded on x-ray film, of a thin-walled gold hohlraum used for radiation-driven experiments. Figure 96.88(b) shows the hohlraum in the center with 12 laser beams "driving" it. The top right corner shows the backlighter substrate while the object in the lower left-hand corner is the diagnostic camera. The high resolution, large dynamic range, and penetrating ability of the 9-keV x rays are apparent.

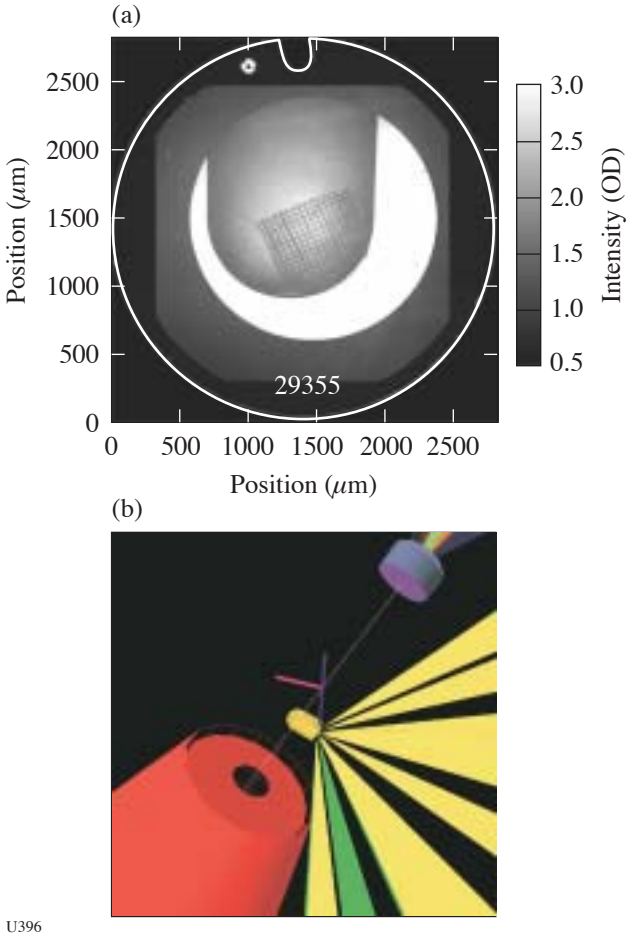

Figure 96.88
(a) Static x-ray radiograph with a 9-keV backlighter of a hohlraum with a resolution grid attached. A 62-μm (20-μm bar width) period grid was used for spatial calibration. (b) Configuration showing diagnostic nose tip, hohlraum, and backlighter substrate.

Beryllium Ablative Microstructure Stability (BAMS): Materials experiments concentrate on measuring the shock-propagation properties of beryllium because beryllium-based alloys are prime candidates for the NIF capsule material. Since the fusion yield depends strongly on the symmetry of the capsule during implosion, the importance of the elastic anisotropy of Be in the seeding of hydrodynamic instabilities is paramount. To measure this effect directly, Los Alamos began a series of beryllium ablative microstructure stability (BAMS) experiments. To that end, a 6-ns laser pulse was designed to achieve radiation pressure in a hohlraum environment to drive over 50 Rayleigh–Taylor growth times. LLE personnel have fabricated two separate pulse shapes, carried by 13 phased beams, which closely approximate the desired drive. Preliminary analysis of radiation temperature data (Dante and VISAR) indicates close agreement with calculations.

A small Be patch was mounted on the rear wall of the hohlraum opposite the laser entrance hole. Face-on x-ray radiography in the first experiment was used to assess the influx of Au from the hohlraum walls into the diagnostic line of sight and to observe machined perturbations in a Be-Cu (0.9% by atom) alloy. Self-backlighting by Au near the laser entrance hole shows growth of the 100-μm period perturbations with evidence of a Be bubble forming near the target axis (Fig. 96.89). Future experiments will optimize radiography techniques and possibly employ gas-filled hohlraums to inhibit Au transport toward the axis.

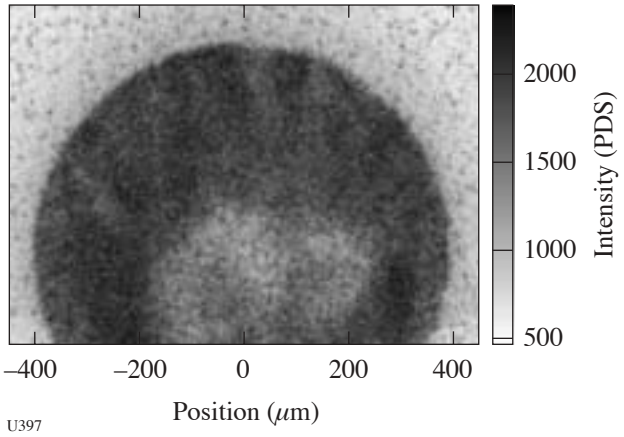

Figure 96.89
A radiograph of a sample Be backlit by Au emission within the hohlraum. The fringes correspond to the 100-μm period of machined perturbations in the Be patch. The light area on axis could be Au opacity or exclusion of Au by a Be bubble arising from the patch.

FY03 SNL OMEGA PROGRAMS

Sandia National Laboratories (SNL) carried out a total of 30 target shots on the OMEGA laser in FY03 and also participated in several of the campaigns led by other laboratories. The SNL-led campaigns included the following:

SOP/Aluminum Wedge Verification of Hohlraum Drive Temperature and Shock Temperature: In FY03, streaked optical pyrometer (SOP)[19] measurements of the shock velocity in aluminum wedges were begun on OMEGA to verify hohlraum radiation temperature. The aluminum wedges in these experiments were fielded side by side with indirect-drive ICF ablator samples for the purpose of SOP intensity calibration at the 280±20-nm bandpass. As was done years ago on Nova, this data can also be used, however, to verify the hohlraum radiation temperature.[20,21] There were some surprises in this new data. Figure 96.90(a) shows a comparison of the pre-shot calculation with the unfolded Al-wedge SOP data from OMEGA shot 31819 (5.56 kJ, 2 ns square). The measured Al shock velocity was about 12% higher than predicted in the pre-shot *LASNEX* calculations. The result of a post-shot calculation using a drive multiplier to match the data is also indicated in the figure. Figure 96.90(b) shows the overlay of a DANTE[22] measurement for a very similar previous hohlraum experiment done on a P6-P7 axis (OMEGA shot 27564; 5.53 kJ, 2 ns). It appears that both the post-shot and pre-shot versions of the drive are close to bounding the uncertainty of the DANTE measurement; however, the same conclusion is not reached in our analysis of the similar experiment employing a 1-ns drive. In this experiment (OMEGA shot 31820), the measured Al velocity was about 25% higher than the pre-shot prediction.

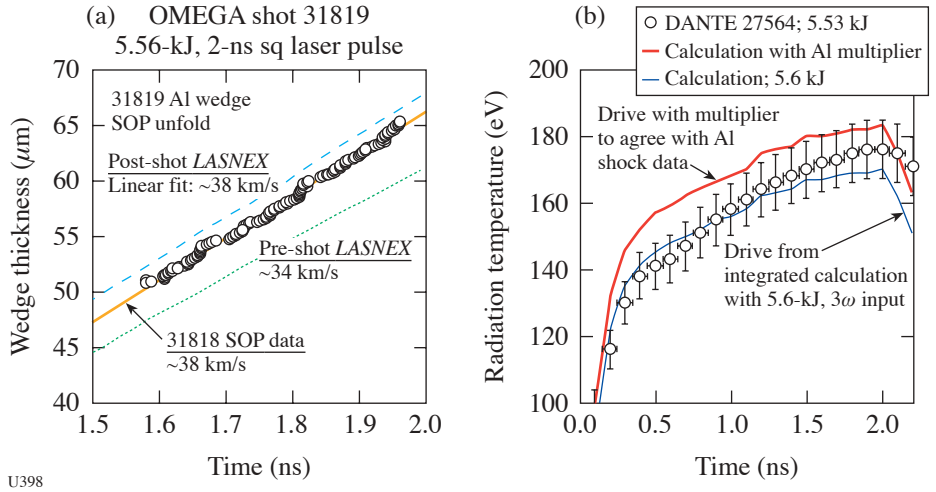

Figure 96.90
(a) Unfold of shock position versus time for Al wedge in OMEGA shot 31819 (5.56 kJ, 2 ns square) compared to pre-shot and post-shot *LASNEX* calculations. (b) Comparison of Dante unfold from OMEGA shot 27564 (5.53 kJ, 2 ns square) with drive from shot 31819 pre-shot and post-shot calculations.

These hohlraum drive measurement comparison issues will be explored further in the FY04 SNL campaign.

Experimental Verification of Shock Temperature and Preheat Reduction in Doped Ablator Samples: In FY03, the streaked optical pyrometer (SOP)[19] was used to view the preheat and shock breakout in side-by-side samples of doped and undoped indirect-drive ICF ablator samples. A key result was the experimental demonstration of preheat and shock temperature reduction via the use of mid-*Z* dopants in the low-*Z* ablator material.[23,24] Figure 96.91(a) shows the SOP image from OMEGA shot 31821 in which side-by-side, wedge-shaped samples of $C_{38}H_{60}O_2$ and $C_{39}H_{57}O_2Ge_2$ were driven by a hohlraum radiation pulse. It is clear from the image that the intensity levels of the preheat and the shock breakout are significantly reduced in the Ge-doped sample. Figures 96.91(b) and 96.91(c) show overlays of the intensity–time lineouts of side-by-side doped and undoped samples driven at hohlraum temperatures of ~160 eV (OMEGA shot 31818, 2 ns square) and ~200 eV (OMEGA shot 31821, 1 ns square). It found that the ~8× reduction in preheat and the 2× reduction in shock temperature are approximately consistent with *LASNEX* calculations that employ opacities based on the techniques of Refs. 25 and 26. Similar side-by-side experiments using undoped and Cu-doped beryllium samples are planned for early FY04. A new issue arising with this data is illustrated in Fig. 96.92. As indicated in the figure, the detailed analysis of the Ge-doped CH-wedge measurements indicates a shock velocity that is ~12% to 15% lower than the *LASNEX* calculations. This result would appear to be in contradiction to the Al-wedge results (see previous section) in which Al shock velocity is found to be higher than the *LASNEX* prediction (a result that is found even in the experiment employing side-by-side wedges of Al and Ge-doped CH). This issue will also be explored further in FY04.

Indirect-Drive ICF Ablator X-Ray Burnthrough Measurements: To achieve indirect-drive ignition of an ICF capsule, ablator burnthrough timing must be predicted to within a few percent. In FY03, the techniques described in Ref. 27 were employed to begin using the streaked x-ray imager (SXI) diagnostic[28] to view time-resolved x-ray burnthrough in side-by-side samples of ablator materials having different thicknesses or dopant levels. An example of this new data is shown in Fig. 96.93. The fact that the signals from the doped and undoped CH do not overlay with 700-eV offset is consistent with the calculations only if a significant contribution of second-order, 1.4-keV flux is included. This represents a new unresolved issue: the result is contrary to our past experience with the SXI data. Another interesting new issue that has come up in the SXI data that is related to the discussions of the two previous sections is illustrated in Fig. 96.94. Here, the new information on hohlraum drive is applied to the analysis of previous polyimide x-ray burnthrough data obtained in FY02. As indicated in the figure, it appears that the application of the new Al-wedge drive data leads to a significantly improved agreement between the calculated and measured x-ray burnthrough behavior.

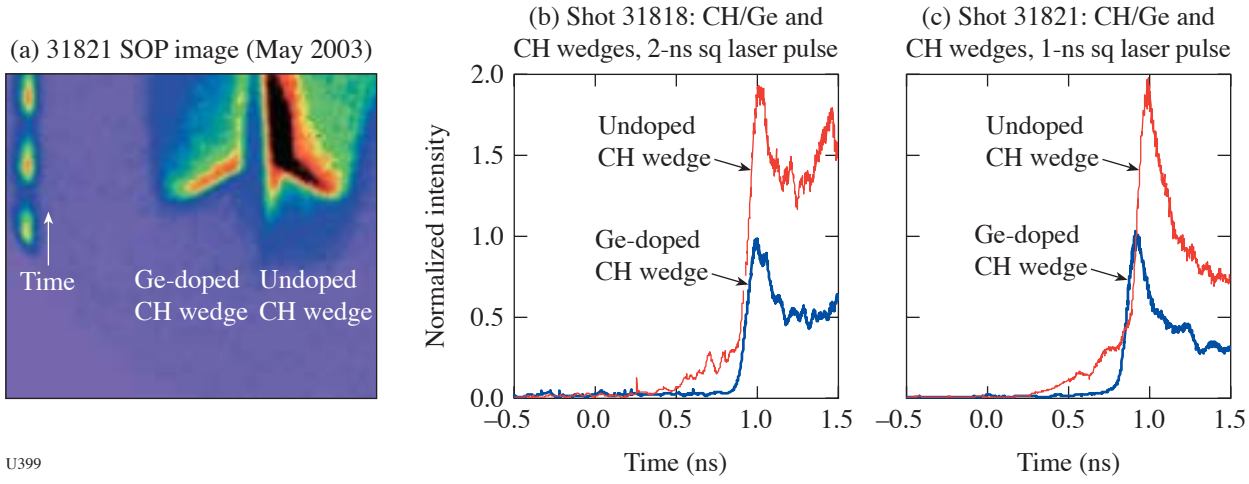

Figure 96.91
(a) SOP image from OMEGA shot 31821 in which side-by-side wedge-shaped samples of $C_{38}H_{60}O_2$ and $C_{39}H_{57}O_2Ge_2$ were driven by a hohlraum radiation pulse. (b) and (c) Overlays of the intensity–time lineouts of side-by-side doped and undoped samples driven at hohlraum temperatures of ~160 eV (OMEGA shot 31818, 2 ns square) and ~200 eV (OMEGA shot 31821, 1 ns square).

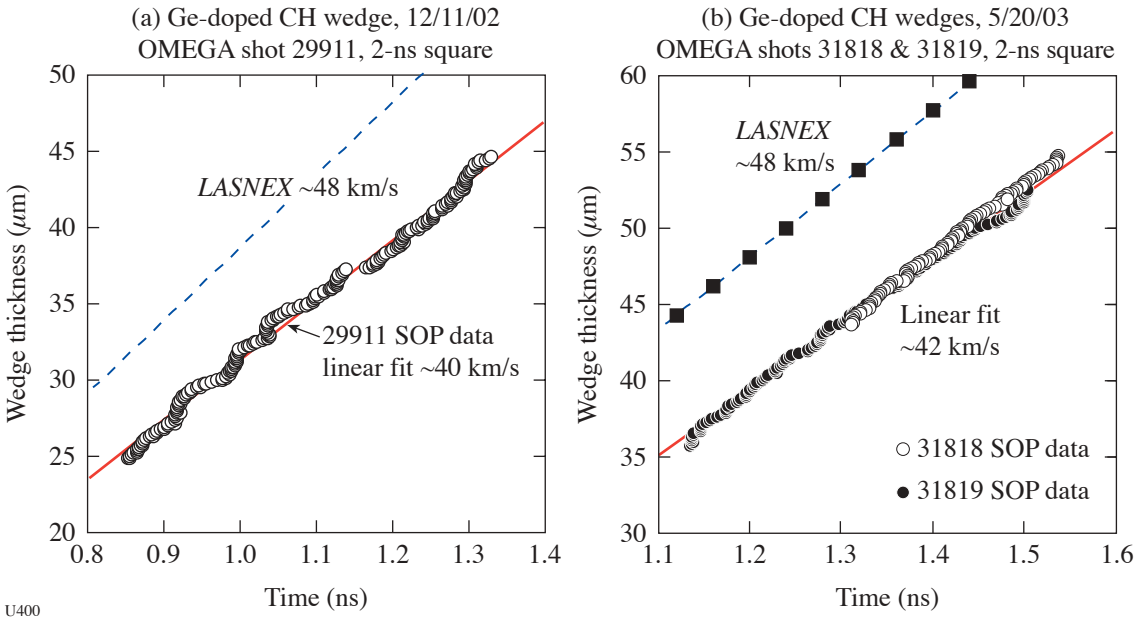

Figure 96.92
Unfold of shock position versus time for Ge-doped CH wedges in (a) OMEGA shot 29911 and (b) shots 31818 and 31819.

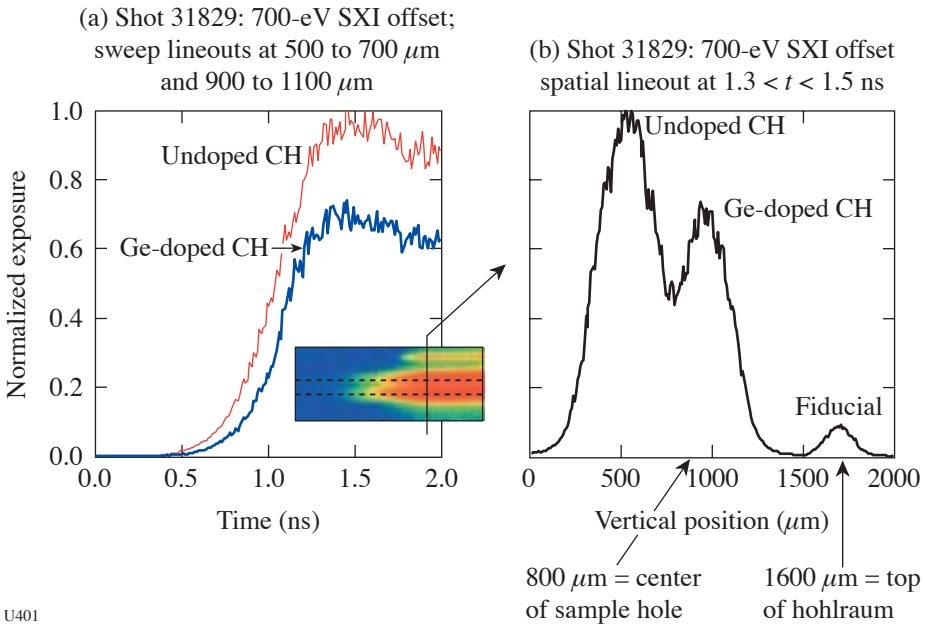

Figure 96.93
Spatial lineout through SXI streaked image including times between 1.3 and 1.5 ns for OMEGA shot 31829 employing side-by-side samples of Ge-doped and undoped CH.

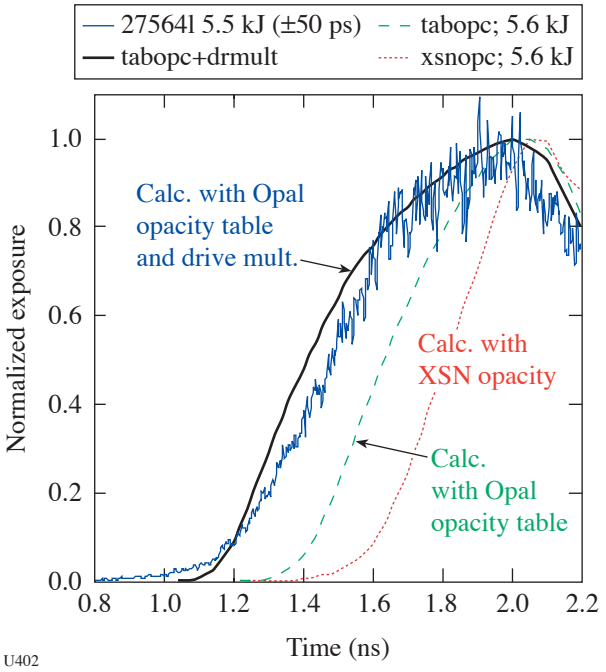

Figure 96.94
Comparison of *LASNEX* calculation variations to the SXI data lineout for OMEGA shot 27564.

CEA PROGRAMS

The Commissariat à l'Énergie Atomique (CEA) of France was allotted three shot days on OMEGA in FY03 and carried out 32 target experiments. The experiments were focused in two primary areas: (a) laser–matter interaction and (b) diagnostics development.

First Tests of the DEMIN Spectrometer on OMEGA

a. Laser–Matter Interaction: A new Thomson-scattering configuration for probing electron-plasma waves stimulated by Raman backscattering instability (SRS) was defined and successfully tested on OMEGA in FY03. In this experiment, two OMEGA beams at 3ω were used to stimulate and probe electron-plasma waves in a plasma preformed by 40 heater beams. This configuration will be used to investigate the growth and saturation of SRS in gas-bag targets (Fig. 96.95) representative of the homogeneous plasmas that will be produced on the NIF and LMJ. For this study, Thomson scattering is a valuable complementary diagnostic of backscattering stations because it provides measurements that are spatially resolved along the interaction-beam propagation axis, thus demonstrating that SRS activity is occurring in a plasma representative of the NIF and LMJ.

b. Diagnostics Development: The DEMIN (detector micromegas for neutrons) neutron spectrometer[29] designed by CEA was tested for the first time during ICF experiments on OMEGA in FY03. The DEMIN concept, derived from the one used on high-energy physics,[30] is based on the association of a neutron-to-proton converter with a thin gas chamber (600 μm). This design has an efficiency of 10^{-3} and 10^{-6}, respectively, for 14-MeV neutrons and 1-MeV photons. This intrinsic γ-ray insensitivity allows the measurement of secondary (DD target) and tertiary (DT target) neutrons in large γ background. This γ background is induced by (n, γ) interaction on hardware present in the experimental area [noted (n, γ) on Fig. 96.96].

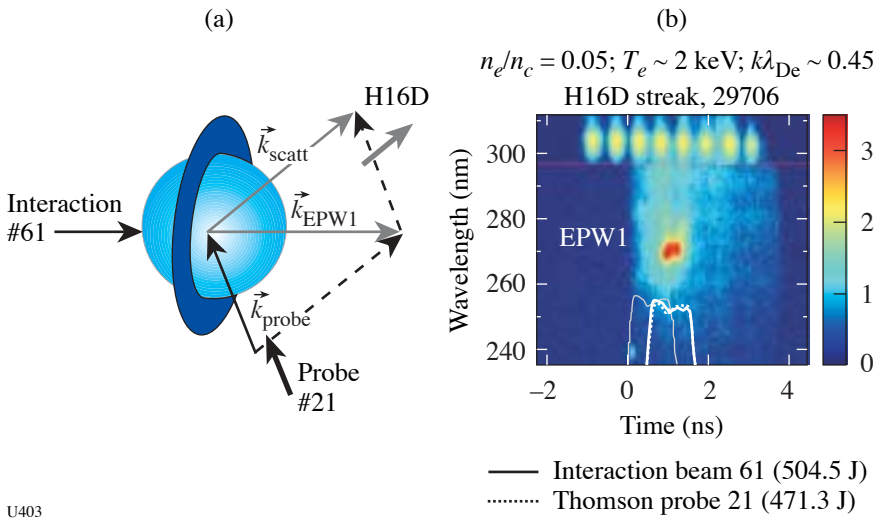

Figure 96.95
(a) Schematic of SRS experiment showing gas-bag target geometry with an interaction beam (61) and probe beam (21). (b) Streak camera recording of Thomson signal generated by scattering from electron-plasma waves generated by the SRS instability.

Recorded DEMIN signals show this relative γ transparency by comparison with a calibrated scintillator plus photomultiplier tube (HCB12). Figures 96.96 and 96.97 present photon and neutron flux as a function of the time after the target implosion.

In both cases, the comparison of signals from DEMIN and HCB12 shows the intrinsic γ-ray insensitivity of the DEMIN spectrometer. Gamma rays induce small or non-observed signals in the time-of-flight window, where secondary and tertiary neutrons will induce signals with several tens of millivolts.

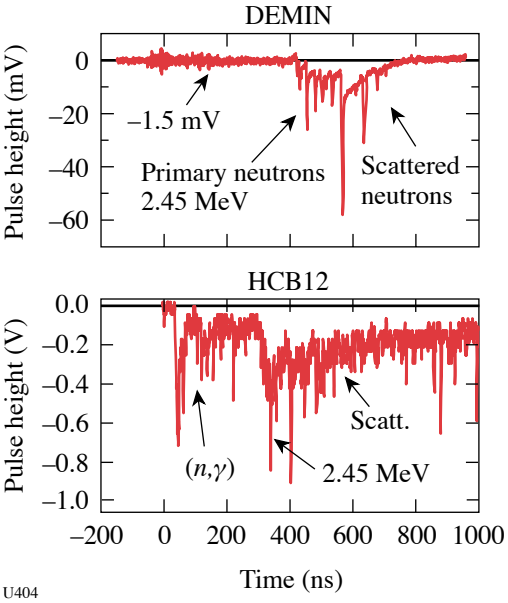

Figure 96.96
DEMIN record from DD target shot #31774. In the case of DD targets, γrays do not induce signals before primary and scattered neutrons in DEMIN. The noise in the measurement time window of expected secondary neutrons (12 to 17 meV) is low (±1.5 mV). In this DEMIN configuration, secondary neutrons will give several tens of millivolts. By comparison, γrays are clearly observed by the HCB12 detector and will mask any secondary neutron signal.

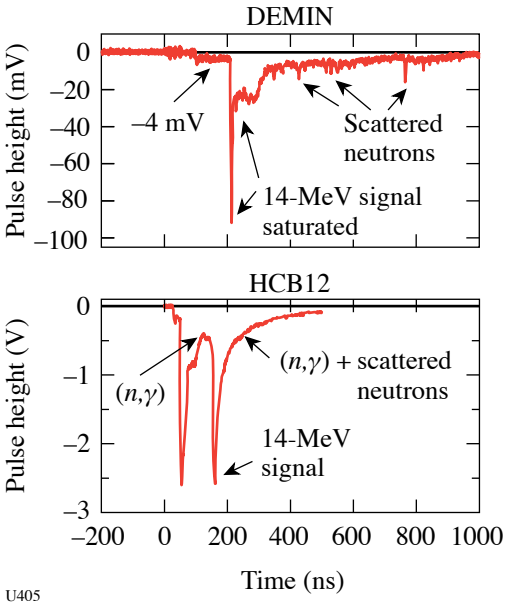

Figure 96.97
DEMIN record from DT target shot #31750. In the case of a DT target, the signal induced by the 14-MeV neutrons is saturated in DEMIN; the high yield of primary neutrons inhibits the electric field in the gas during few tens of nanoseconds. Whereas with the HCB12 detector the γ rays signal is as important as for 14-MeV neutrons, the DEMIN exhibits a low signal (≤4 mV).

Fast Photoconductor for Neutron Spectroscopy: the SCANED Concept

The SCANED (SCAttered NEutron Diagnostic) detector, designed by CEA, was tested during the DT shots campaign in May 2003. The concept is based on a photoconductor operating as a time-of-flight detector. The fast response of photoconductors is the main advantage, allowing location near the target; therefore, the neutron spectrum is recorded before the arrival of scattered neutrons and gamma rays produced on the chamber hardware. This concept is proposed for various measurements in ICF experiments: ion temperature, neutron yields, $\langle \rho R \rangle$ by secondary neutrons (DD target), and downscattered neutrons (DT target).[31,32] Moreover, photoconductors can be an alternative for diagnostics that may be inoperative with high yields (on the NIF and LMJ).

SCANED is composed of a *n*-irradiated AsGa detector (6×4 mm^2) fixed in a 50-Ω loaded design made of plastic and Teflon to minimize (n,n') and (n,γ) interactions. Signals are recorded by a set of three IN7100 oscilloscopes to get a large dynamic range.

The goals of the experiments performed in May were the measurement of the sensitivity to 14-MeV neutrons and the study of noise, EM effects, and the duration of the tail in the pulse shape after the prompt 14-MeV neutron interaction.

Two SCANED setups were tested at 1 m and 0.385 m from target chamber center (TCC), respectively. Figure 96.98 shows a typical spectrum for the closest location. We easily observe 14-MeV and 2.45-MeV neutron peaks, from D+T and D+D fusion, respectively. The gamma background induced by the neutron interaction in the chamber skin is measured about 29 ns after the 14-MeV neutron signal. A DMX diode located between SCANED and the target (at 13.5 cm from the target) induces background over 10 ns after the x-ray signal is emitted by the target.

Work is in progress to improve the response of photoconductors.

Capillaries Detector for ICF Capsule Neutron Images

14-MeV imaging detector arrays have been developed by assembling glass capillaries of 85-μm mean diameter into 100 $\times$ 100-mm^2 coherent arrays. The capillaries are filled with a liquid scintillator whose optical index is higher than the glass index. Neutron scattering of the hydrogen nuclei of the scintillator and the recoil ions produce light in several adjacent capillaries as they lose energy. The light distribution about the scattering point determines the detector spatial resolution. A 650-μm spatial resolution has been achieved; the resolution is enhanced to 325 μm by loading deuterium in the scintillator as the recoil deuterons have shorter mean free paths than recoil protons (Fig. 96.99). This array has been tested on the OMEGA neutron imaging system (NIS). These results will permit the achievement of high resolution in neutron images with moderate magnification ratio and practical line of sight on LMJ and the NIF.

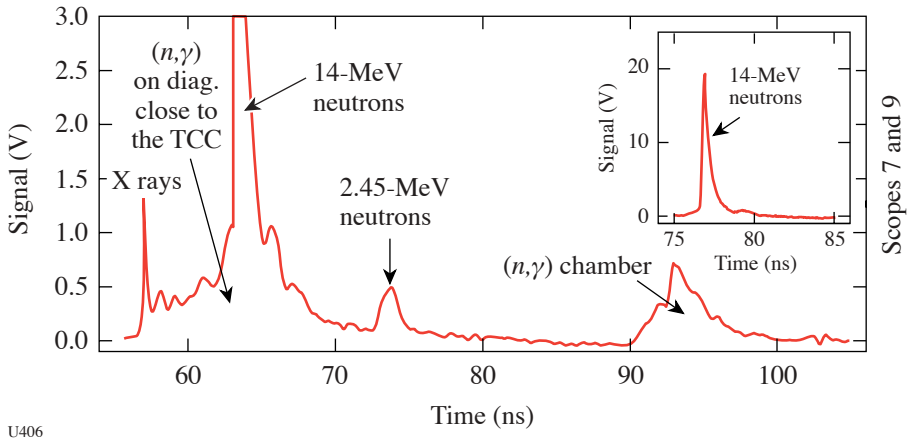

Figure 96.98
SCANED signal on shot 31756 (DT-filled target).

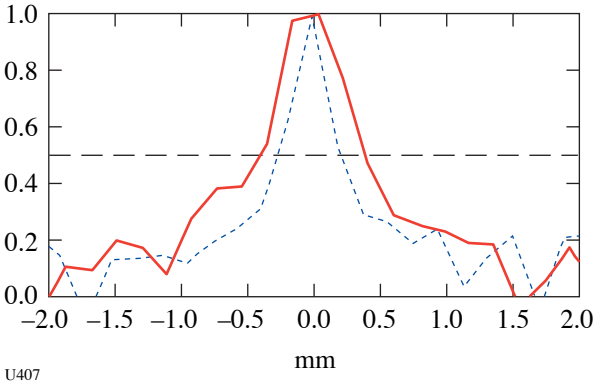

Figure 96.99
14-MeV neutron point-spread function measured in the 85-μm-diam capillaries array filled with a high-optical-index scintillator nondeuterated (solid line) and deuterated (dashed lines). Corrected from the 380-μm readout system resolution, the FWHM is 650 μm and 325 μm for the nondeuterated and deuterated scintillator, respectively.

Neutron-Induced Current Generation

High-pulsed neutron irradiation can drive a transient current generation on coaxial cables. For intense, 14-MeV neutron irradiation that will exit on future ICF facilities such as LMJ in France and the NIF in the U.S., this effect can generate a signal on a 50-Ω load as high as a few hundred volts. On such a facility, coaxial cable will be widely used to transfer the electrical signals generated by the detectors placed close to the source to their recording devices placed away from the target to be sufficiently protected against the nuclear environment induced by this neutron irradiation. All of these cables will be affected by the parasitic signals induced by the pulsed neutron irradiation during high-yield neutron shots. No simple protective method (other than cumbersome 1-m-thick shielding) can protect the cable from this intense neutron irradiation. To investigate the potential level of this effect, OMEGA was used as an intense, pulsed, 14-Mev neutron source on direct-drive-yield neutron shots (up to 10^{14} neutrons of 14 MeV). OMEGA shots can induce a weaker but sufficient signal to be recorded if a coaxial cable can be placed sufficiently close to the target. In this case, a standard high-bandwidth coaxial cable (1/4-in.-diam, semi-rigid SMA type) was set at 25 cm on the neutron source by means of a diagnostic inserter (TIM). A weak but clear signal was recorded (Fig. 96.100).

Each weak bump on this recorded signal is associated with the 14-MeV neutron burst (time duration of 100 ps, which corresponds to a space extension of 5 mm) on each U-turn of the zigzag coaxial cable placed closest to the neutron source (see Fig. 96.101). In order to accurately time-reference each induced signals with respect to the time of neutron production, a standard x-ray diode was added at the end of the coaxial cable to record the instant of the neutron production (associated with a hard-x-ray burst). This time is represented by the signal bump #4, which corresponds to the arrival of the x ray on the diode. Each of the bumps is clearly identified due to the arrival of the neutron burst at each of the U-turns (bumps 1 to 6). Moreover, each signal generated by the neutrons on each U-turn is also reflected by the coaxial end and represents later bumps (7 to 11), so a clear time reference is associated with each bump and clearly shows the effect of pulsed neutron generation on a coaxial cable.

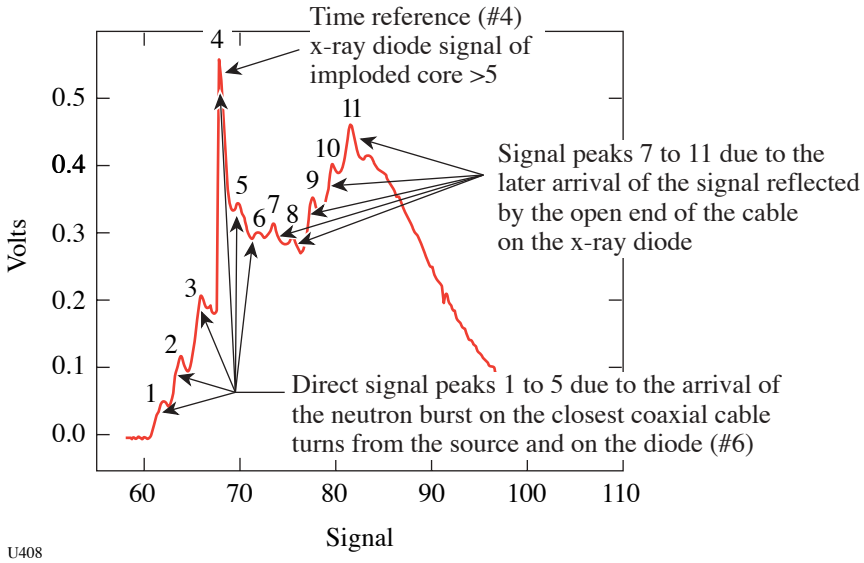

Figure 96.100
Signal recorded by a high-bandwidth (7-GHz), single-shot oscilloscope on high-yield OMEGA neutron shots.

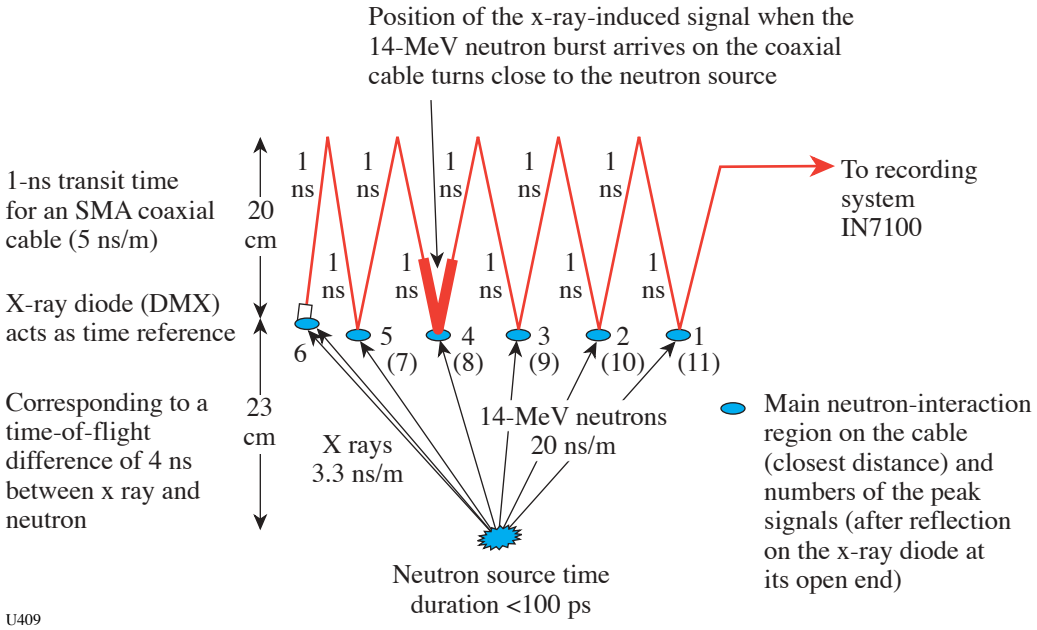

Figure 96.101
Schematic drawing of the experimental setup showing the origin of each signal bump.

REFERENCES

1. H. F. Robey *et al.*, Phys. Plasmas **10**, 614 (2003).
2. P. A. Keiter, R. P. Drake, T. S. Perry, H. F. Robey, B. A. Remington, C. A. Iglesias, R. J. Wallace, and J. Knauer, Phys. Rev. Lett. **89**, 165003 (2002).
3. A. C. Calder *et al.*, Astrophys. J. Suppl. Ser. **143**, 201 (2002).
4. A. Miles, D. Braun, J. Edwards, H. F. Robey, R. P. Drake, D. R. Leibrandt, E. C. Harding, J. P. Knauer, and D. Arnett, "Numerical Simulation of Supernova-Relevant Laser-Driven Hydrodynamics Experiments on OMEGA," submitted to Physics of Plasmas.
5. R. P. Drake, B. A. Remington, and D. D. Ryutov, "Experimental Astrophysics with Intense Lasers," submitted to Review of Modern Physics.
6. R. D. Petrasso, J. A. Frenje, F. H. Séguin, C. K. Li, B. E. Schwartz, C. Stoeckl, P. B. Radha, J. A. Delettrez, D. D. Meyerhofer, S. Roberts, T. C. Sangster, and J. M. Soures, Bull. Am. Phys. Soc. **47**, 145 (2002).
7. B. E. Schwartz, F. H. Séguin, J. A. Frenje, R. D. Petrasso, C. K. Li, P. B. Radha, D. D. Meyerhofer, S. Roberts, T. C. Sangster, J. M. Soures, and C. Culligan, Bull. Am. Phys. Soc. **47**, 219 (2002).
8. C. K. Li, F. H. Séguin, J. A. Frenje, R. D. Petrasso, J. A. Delettrez, R. L. Keck, J. M. Soures, P. W. McKenty, F. J. Marshall, V. N. Goncharov, J. P. Knauer, D. D. Meyerhofer, P. B. Radha, S. P. Regan, T. C. Sangster, and W. Seka, "ρR Asymmetry in the Spherical Implosion of Inertial Confinement Fusion," submitted to Physical Review Letters.
9. R. I. Klein *et al.*, Astrophys. J. **583**, 245 (2003).
10. H. F. Robey, T. S. Perry, R. I. Klein, J. O. Kane, J. A. Greenough, and T. R. Boehly, Phys. Rev. Lett. **89**, 085001 (2002).
11. C. Stoeckl, R. E. Bahr, B. Yaakobi, W. Seka, S. P. Regan, R. S. Craxton, J. A. Delettrez, R. W. Short, J. Myatt, A. V. Maximov, and H. Baldis, Phys. Rev. Lett. **90**, 235002 (2003).
12. L. A. Welser, R. C. Mancini, J. A. Koch, S. Dalhed, R. W. Lee, I. E. Golovkin, F. Marshall, J. Delettrez, and L. Klein, Rev. Sci. Instrum. **74**, 1951 (2003).
13. L. A. Welser, R. C. Mancini, J. A. Koch, N. Izumi, H. Dalhed, H. Scott, T. W. Barbee, Jr., R. W. Lee, I. E. Golovkin, F. Marshall, J. Delettrez, and L. Klein, J. Quant. Spectrosc. Radiat. Transf. **81**, 487 (2003).
14. D. R. Kania *et al.*, J. Appl. Phys. **68**, 124 (1990).
15. N. E. Lanier *et al.*, Phys. Plasmas **10**, 1816 (2003).
16. M. M. Balkey *et al.*, "Production and Metrology of Cylindrical Inertial Confinement Fusion Targets with Sinusoidal Perturbations," Los Alamos National Laboratory report LA-UR-03-3682 (2003); to be published in *Fusion Science and Technology*.
17. W. S. Varnum, N. D. Delamater, S. C. Evans, P. L. Gobby, J. E. Moore, J. M. Wallace, R. G. Watt, J. D. Colvin, R. Turner, V. Glebov, J. Soures, and C. Stoeckl, Phys. Rev. Lett. **84**, 5153 (2000).
18. J. M. Foster *et al.*, Phys. Plasmas **9**, 2251 (2002).

19. J. A. Oertel *et al*., Rev. Sci. Instrum. **70**, 803 (1999).

20. R. L. Kauffman *et al*., Phys. Rev. Lett. **73**, 2320 (1994).

21. R. L. Kauffman *et al*., Rev. Sci. Instrum. **66**, 678 (1995).

22. H. N. Kornblum, R. L. Kauffman, and J. A. Smith, Rev. Sci. Instrum. **57**, 2179 (1986).

23. R. E. Olson *et al*., "Preheat Effects on Shock Propagation in Indirect-Drive Inertial Confinement Fusion Ablator Materials," to be published in Physical Review Letters.

24. R. E. Olson *et al*., "Shock Propagation, Preheat, and X-Ray Burn-through in NIF Ignition Capsule Ablator Materials," submitted to Physics of Plasmas.

25. A. Bar-Shalom *et al*., Phys. Rev. A **40**, 3183 (1989).

26. F. J. Rogers, B. G. Wilson, and C. A. Iglesias, Phys. Rev. A, Gen. Phys. **38**, 5007 (1988).

27. R. E. Olson *et al*., Rev. Sci. Instrum. **74**, 2186 (2003).

28. T. J. Orzechowski *et al*., Phys. Rev. Lett. **77**, 3545 (1996).

29. M. Houry *et al*., "A New Diagnostic Design to Achieve Neutron Spectroscopy in a High Gamma Background on ICF Experiments," presented at the EuroConference on Advanced Diagnostics for Magnetic and Inertial Fusion, Varenna, Italy, 3–7 September 2001.

30. Y. Giomataris *et al*., Nucl. Instrum. Methods Phys. Res. A **376**, 29 (1996).

31. D. C. Wilson *et al*., Nucl. Instrum. Methods Phys. Res. A **488**, 400 (2002).

32. G. J. Schmid, LLNL, private communication (2002).

Publications and Conference Presentations

Publications

I. Begishev, V. Bagnoud, M. Guardalben, L. Waxer, J. Puth, and J. Zuegel, "Optimization of an Optical Parametric Chirped Pulse Amplification System for the OMEGA EP Laser System," in *Advanced Solid-State Photonics, OSA Technical Digest* (Optical Society of America, Washington, DC, 2003), pp. 252–254.

S. H. Chen, H. M. P. Chen, Y. Geng, S. D. Jacobs, K. L. Marshall, and T. N. Blanton, "Novel Glassy Nematic Liquid Crystals for Non-Destructive Rewritable Optical Memory and Photonic Switching," Adv. Mater. **15**, 1061 (2003).

S. W. Culligan, Y. Geng, S. H. Chen, K. Klubek, K. M. Vaeth, and C. W. Tang, "Strongly Polarized and Efficient Blue Organic Light-Emitting Diodes Using Monodisperse Glassy-Nematic Oligo(fluorene)s," Adv. Mater. **15**, 1176 (2003).

J. E. DeGroote, S. D. Jacobs, J. M. Schoen, H. J. Romanofsky, and I. A. Kozhinova, "Magnetorheological Finishing of a Diamond Turned Poly(Methylmethacrylate) Flat," in *Optifab 2003* (SPIE, Bellingham, WA, 2003), Vol. TD02, pp. 65–68.

Q. Guo, X. Teng, and H. Yang, "Surface Patterns of Tetragonal Phase FePt Thin Films from Pt@Fe_2O_3 Core-Shell Nanoparticles Using Combined Langmuir-Blodgett and Soft Lithographic Techniques," in *Unconventional Approaches to Nanostructures with Applications in Electronics, Photonics, Information Storage and Sensing*, Materials Research Society, Vol. 776, edited by O. D. Velev, T. J. Bunning, Y. Xia, and P. Yang (Materials Research Society, Warrendale, PA, 2003), pp. 187–192.

I. V. Igumenshchev, R. Narayan, and M. A. Abramowicz, "Three-Dimensional Magnetohydrodynamic Simulations of Radiatively Inefficient Accretion Flows," Astrophys. J. **592**, 1042 (2003).

A. Jukna and R. Sobolewski, "Time-Resolved Photoresponse in the Resistive Flux-Flow State in Y-Ba-Cu-O Superconducting Microbridges," Supercond. Sci. Technol. **16**, 911 (2003).

T. Z. Kosc, K. L. Marshall, and S. D. Jacobs, "Polymer Cholesteric Liquid Crystal Flakes for Particle Displays," in *2003 SID International Symposium, Digest of Technical Papers*, 1st ed., edited by J. Morreale (Society for Information Display, San Jose, CA, 2003), Vol. 34, Book 1, pp. 581–583.

J. Li, W. R. Donaldson, and T. Y. Hsiang, "Very Fast Metal–Semiconductor–Metal Ultraviolet Photodetectors on GaN with Submicron Finger Width," IEEE Photonics Technol. Lett. **15**, 1141 (2003).

A. E. Marino, J. Hayes, L. L. Gregg, and S. D. Jacobs, "Grain Decoration in Aluminum Oxynitride (ALON) from Polishing on Bound Abrasive Laps," in *Optifab 2003* (SPIE, Bellingham, WA, 2003), Vol. TD02, pp. 81–83.

D. N. Maywar, S. Banerjee, A. Agarwal, D. F. Grosz, M. Movassaghi, A. P. Küng, and T. H. Wood, "Impact of Relaxed Dispersion Map and Gain Ripple on Ultra-Wideband 10-Gbit/s Transmission," Electron. Lett. **39**, 1266 (2003).

M. Mikulics, M. Marso, P. Kordoš, S. Stanček, P. Kováč, X. Zheng, S. Wu, and R. Sobolewski, "Ultrafast and Highly Sensitive Photodetectors Fabricated on High-Energy Nitrogen-Implanted GaAs," Appl. Phys. Lett. **83**, 1719 (2003).

J. A. Randi, J. C. Lambropoulos, S. D. Jacobs, and S. N. Shafrir, "Determination of Subsurface Damage in Single Crystalline Optical Materials," in *Optifab 2003* (SPIE, Bellingham, WA, 2003), Vol. TD02, pp. 84–86.

A. E. Schoeffler, L. L. Gregg, J. M. Schoen, E. M. Fess, M. Hakiel, and S. D. Jacobs, and "Pre-Polishing on a CNC Platform with Bound Abrasive Contour Tools," in *Optifab 2003* (SPIE, Bellingham, WA, 2003), Vol. TD02, pp. 24–27.

J. L. Sternal, S. N. Shafrir, J. A. Randi, L. L. Gregg, and S. D. Jacobs, "Refractive Index Anisotropy in Optics Using a Birefringence Mapper," in *Optifab 2003* (SPIE, Bellingham, WA, 2003), Vol. TD02, pp. 125–127.

A. Sunahara, J. A. Delettrez, C. Stoeckl, R. W. Short, and S. Skupsky, "Time-Dependent Electron Thermal Flux Inhibition in Direct-Drive Laser Implosion," Phys. Rev. Lett. **91**, 095003 (2003).

R. Varshneya, J. E. DeGroote, L. L. Gregg, and S. D. Jacobs, "Characterizing Optical Polishing Pitch," in *Optifab 2003* (SPIE, Bellingham, WA, 2003) Vol. TD02, pp. 87–89.

L. J. Waxer, V. Bagnoud, I. A. Begishev, M. J. Guardalben, J. Puth, and J. D. Zuegel, "High-Conversion-Efficiency, Optical Parametric Chirped-Pulse-Amplification System Using Spatiotemporally Shaped Pump Pulses," Opt. Lett. **28**, 1245 (2003).

Forthcoming Publications

E. L. Alfonso, R. Q. Gram, and D. R. Harding, "Modeling Temperature and Pressure Gradients During Cooling of Thin-Walled Cryogenic Targets," to be published in Fusion Science and Technology.

K. Anderson and R. Betti, "Laser-Induced Adiabat Shaping by Relaxation in Inertial Fusion Implosions," to be published in Physics of Plasmas.

K. Anderson and R. Betti, "Theory of Laser-Induced Adiabat Shaping in Inertial Fusion Implosions: The Decaying Shock," to be published in Physics of Plasmas.

V. Bagnoud and J. D. Zuegel, "Independent Phase and Amplitude Control of a Laser Beam Using a Single-Phase-Only Spatial Light Modulator," to be published in Optics Letters.

Y. Geng, A. C. A. Chen, J. J. Ou, S. H. Chen, K. Klubek, K. M. Vaeth, and C. W. Tang, "Monodisperse Glassy-Nematic Conjugated Oligomers with Chemically Tunable Polarized Light Emission," to be published in Chemistry of Materials.

Y. Geng, A. Trajkovska, S. W. Culligan, J. J. Ou, H. M. P. Chen, D. Katsis, and S. H. Chen, "Origins of Strong Chiroptical Activities in Films of Nonafluorenes with a Varying Extent of Pendant Chirality," to be published in the Journal of the American Chemical Society.

O. V. Gotchev, L. J. Hayes, P. A. Jaanimagi, J. P. Knauer, F. J. Marshall, and D. D. Meyerhofer, "Large-Grazing-Angle, Multi-Image Kirkpatrick–Baez Microscope as the Front End to a High-Resolution Streak Camera for OMEGA," to be published in Review of Scientific Instruments.

M. J. Guardalben, J. Keegan, L. J. Waxer, V. Bagnoud, I. A. Begishev, J. Puth, and J. D. Zuegel, "Design of a Highly Stable, High-Conversion-Efficiency, Optical Parametric Chirped-Pulse Amplification System with Good Beam Quality," to be published in Optics Express.

T. I. Lakoba, C. Dorrer, and D. N. Maywar, "Polarization-Mode Dispersion of a Circulating Loop," to be published in the Journal of the Optical Society of America B.

J. Leuthold, R. Ryf, D. N. Maywar, S. Cabot, and J. Jacques, "Demonstration of Nonblocking Cross Connect Concept Based on Regenerative All-Optical Wavelength Converter over 42 Nodes and 16800 km," to published in IEEE Photonics Technology Letters.

X. Z. Lin, X. Teng, and H. Yang, "Direct Synthesis of Narrowly Dispersed Silver Nanoparticles Using a Single-Source Precursor," to be published in Langmuir.

S. G. Lukishova, A. W. Schmid, A. J. McNamara, R. W. Boyd, and C. R. Stroud, Jr., "Room-Temperature Single Photon Source: Single-Dye-Molecule Fluorescence in Liquid Crystal Host," to be published in the IEEE Journal of Selected Topics in Quantum Electronics.

F. J. Marshall, J. A. Delettrez, R. Forties, R. Keck, J. H. Kelly, P. W. McKenty, S. P. Regan, and L. J. Waxer, "Direct-Drive-Implosion Experiments with Enhanced-Fluence Balance on OMEGA," to be published in Physics of Plasmas.

D. L. McCrorey, R. C. Mancini, V. A. Smalyuk, S. P. Regan, and B. Yaakobi, "Spectroscopic Determination of Compressed-

Shell Conditions in OMEGA Implosions Based on Ti *K*-Shell Line Absorption Analysis," to be published in Review of Scientific Instruments.

R. L. McCrory, D. D. Meyerhofer, R. Betti, T. R. Boehly, R. S. Craxton, T. J. B. Collins, J. A. Delettrez, R. Epstein, V. Yu. Glebov, V. N. Goncharov, D. R. Harding, R. L. Keck, J. H. Kelly, J. P. Knauer, S. J. Loucks, L. Lund, J. A. Marozas, P. W. McKenty, F. J. Marshall, S. F. B. Morse, P. B. Radha, S. P. Regan, S. Roberts, W. Seka, S. Skupsky, V. A. Smalyuk, C. Sorce, C. Stoeckl, J. M. Soures, R. P. J. Town, B. Yaakobi, J. A. Frenje, C. K. Li, R. D. Petrasso, F. H. Séguin, K. A. Fletcher, S. Padalino, C. Freeman, and T. C. Sangster, "Direct-Drive Inertial Confinement Fusion Research at the Laboratory for Laser Energetics," to be published in the proceedings of Current Trends in International Fusion Research: A Review.

R. L. McCrory, D. D. Meyerhofer, S. J. Loucks, S. Skupsky, R. E. Bahr, R. Betti, T. R. Boehly, R. S. Craxton, T. J. B. Collins, J. A. Delettrez, W. R. Donaldson, R. Epstein, J. A. Frenje, V. Yu. Glebov, V. N. Goncharov, D. R. Harding, P. A. Jaanimagi, R. L. Keck, J. H. Kelly, T. J. Kessler, J. P. Knauer, C. K. Li, L. D. Lund, J. A. Marozas, P. W. McKenty, F. J. Marshall, S. F. B. Morse, R. D. Petrasso, P. B. Radha, S. P. Regan, S. Roberts, T. C. Sangster, F. H. Séguin, W. Seka, V. A. Smalyuk, C. Sorce, J. M. Soures, C. Stoeckl, R. P. J. Town, B. Yaakobi, and J. D. Zuegel, "Progress in Direct-Drive Inertial Confinement Fusion Research at the Laboratory for Laser Energetics," to be published in Nuclear Fusion.

R. Narayan, I. V. Igumenshchev, and M. A. Abramowicz, "Magnetically Arrested Disk: An Energetically Efficient Accretion Flow," to be published in the Astrophysical Journal.

B. A. Remington, G. Bazan, J. Belak, E. Bringa, M. Caturla, J. D. Colvin, M. J. Edwards, S. G. Glendinning, D. Ivanov, B. Kad, D. H. Kalantar, M. Kumar, B. F. Lasinski, K. T. Lorenz, J. M. McNaney, D. D. Meyerhofer, M. A. Meyers, S. M. Pollaine, D. Rowley, M. Schneider, J. S. Stölken, J. D. Wark, S. V. Weber, W. G. Wolfer, and B. Yaakobi, "Materials Science Under Extreme Conditions of Pressure and Strain Rate," to be published in Metallurgical and Materials Transactions A.

X. Teng and H. Yang, "Synthesis of Face-Centered Tetragonal FePt Nnaoparticles and Granular Films form Pt@Fe_2O_3 Core–Shell Nanoparticles," to be published in the Journal of the American Chemical Society.

A. Verevkin, A. Pearlman, W. Slysz, J. Zhang, R. Sobolewski, M. Currie, A. Korneev, G. Chulkova, O. Okunev, P. Kouminov, K. Smirnov, B. Voronov, and G. N. Gol'tsman, "Ultrafast Superconducting Single-Photon Detectors for Near-Infrared-Wavelength Quantum Communications," to be published in the Journal of Modern Optics.

Y. Wang, J. F. Wong, X. Teng, X. Z. Lin, and H. Yang, " 'Pulling' Nanoparticles into Water: Phase Transfer of Oleic Acid Stabilized Monodisperse Nanoparticles into Aqueous Solutions of α-Cyclodextrin," to be published in Nano Letters.

Y. Xu, M. Khafizov, L. Satrapinsky, P. Kúš, A. Plecenik, and R. Sobolewski, "Time-Resolved Photoexcitation of the Superconducting Two-Gap State in MgB_2 Thin Films," to be published in Physical Review Letters.

J. Zhang, N. Boiadjieva, G. Chulkova, H. Deslandes, G. N. Gol'tsman, A. Korneev, P. Kouminov, M. Leibowitz, W. Lo, R. Malinsky, O. Okunev, A. Pearlman, W. Slysz, K. Smirnov, C. Tsao, A. Verevkin, V. Voronov, K. Wilsher, and R. Sobolewski, "Noninvasive CMOS Circuit Testing with NbN Superconducting Single-Photon Detectors," to be published in Electronics Letters.

J. D. Zuegel and D. Jacobs-Perkins, "An Efficient, High-Frequency Bulk Phase Modulator," to be published in Applied Optics.

Conference Presentations

T. R. Boehly, T. J. B. Collins, E. Vianello, D. Jacobs-Perkins, D. D. Meyerhofer, D. G. Hicks, P. M. Celliers, G. W. Collins, S. J. Moon, M. E. Foord, J. H. Eggert, and R. Cauble, "Quartz Equation-of-State (EOS) Measurements at the OMEGA Laser Facility," 13th APS Topical Conference on Shock Compression of Condensed Materials, Portland OR, 20–25 July 2003.

The following presentations were made at the SPIE 48th Annual Meeting, San Diego, CA, 3–8 August 2003:

J. E. DeGroote, H. J. Romanofsky, I. A. Kozhinova, J. M. Schoen, and S. D. Jacobs, "Polishing PMMA and Other Optical Polymers with Magnetorheological Finishing."

L. L. Gregg, A. E. Marino, and S. D. Jacobs, "Grain Decoration in Aluminum Oxynitride (ALON) from Polishing on Bound-Abrasive Laps."

P. A. Jaanimagi, "Breaking the 100-fs Barrier with a Streak Camera."

K. L. Marshall, B. Klehn, B. Watson, and D. W. Griffin, "Recent Advances in the Development of Phase-Shifting Liquid Crystal Interferometers for Visible and Near IR-Applications."

K. L. Marshall, B. Schudel, and I. A. Lippa, "Transition Metal Dithiolene Complexes as Near-IR Dyes for Liquid Crystal Device Applications" (invited).

T. Z. Kosc, K. L. Marshall, and S. D. Jacobs, "Polymer Cholesteric Liquid Crystal Flakes for Particle Displays: Impact of Flake Geometry and Materials Processing on Field-Induced Motion in a Fluid Host," XII International Materials Research Conference, Cancun, Mexico, 17–21 August 2003 (invited).

The following presentations were made at the Third International Conference on Inertial Fusion Sciences and Applications, Monterey, CA, 7–12 September 2003:

V. Bagnoud, I. A. Begishev, M. J. Guardalben, J. Keegan, J. Puth, L. J. Waxer, and J. D. Zuegel, "Optical Parametric Chirped-Pulse Amplifier as the Front End for the OMEGA EP Laser Chain."

T. R. Boehly, T. J. B. Collins, E. Vianello, D. Jacobs-Perkins, D. D. Meyerhofer, D. G. Hicks, P. M. Celliers, G. W. Collins, S. J. Moon, M. E. Foord, J. H. Eggert, and R. Cauble, "Deuterium Equation-of-State Measurements Using Laser-Driven Shocks."

T. J. B. Collins, S. Skupsky, V. N. Goncharov, R. Betti, P. W. McKenty, P. B. Radha, R. Epstein, A. Poludnenko, A. Frank, and S. Mitran, "High-Gain, Direct-Drive Foam Target Designs for the National Ignition Facility."

D. R. Harding, E. L. Alfonso, L. M. Elasky, L. S. Iwan, J. Sailer, W. Seka, A. Warrick, and M. D. Wittman, "Formation of Deuterium-Ice Layers in OMEGA Targets."

T. J. Kessler, J. Bunkenburg, H. Huang, A. Kozlov, C. Kelly, and D. D. Meyerhofer, "The Coherent Addition of Gratings for Pulse Compression in High-Energy Laser Systems."

C. K. Li, F. H. Séguin, J. A. Frenje, R. D. Petrasso, J. A. Delettrez, R. L. Keck, J. M. Soures, P. W. McKenty, F. J. Marshall, V. N. Goncharov, J. P. Knauer, D. D. Meyerhofer, P. B. Radha, S. P. Regan, T. C. Sangster, and W. Seka, "ρR Asymmetry in the Spherical Implosions of Inertial Confinement Fusion."

R. L. McCrory, "Progress in Inertial Confinement Fusion Research in the United States" (keynote speaker).

P. W. McKenty, T. C. Sangster, J. A. Delettrez, R. Epstein, V. Yu. Glebov, D. R. Harding, J. P. Knauer, R. L. Keck, S. J. Loucks, L. D. Lund, R. L. McCrory, F. J. Marshall, D. D. Meyerhofer, S. F. B. Morse, S. P. Regan, P. B. Radha, S. Roberts, W. Seka, S. Skupsky, V. A. Smalyuk, C. Sorce, J. M. Soures, J. A. Frenje, C. K. Li, R. D. Petrasso, F. H. Séguin, K. A. Fletcher, S. Padalino, C. Freeman, N. Izumi, J. A. Koch, R. A. Lerche, M. J. Moran, T. W. Phillips, and G. J. Schmid, "Direct-Drive Cryogenic Target Implosion Performance on OMEGA."

T. C. Sangster, "Bridging the Gap: Ignition Diagnostics for the National Ignition Facility."

S. Skupsky, R. Betti, T. J. B. Collins, V. N. Goncharov, J. A. Marozas, P. W. McKenty, P. B. Radha, T. R. Boehly, J. P. Knauer, F. J. Marshall, J. P. Harding, J. D. Kilkenny, D. D. Meyerhofer, T. C. Sangster, and R. L. McCrory, "Advanced Direct-Drive Target Designs for the NIF."

T. Z. Kosc, K. L. Marshall, and S. D. Jacobs, "Polymer Cholesteric Liquid Crystal Flake Particle Displays Utilizing Maxwell–Wagner Polarization Effects for Switching," 23rd International Display Research Conference, Phoenix, AZ, 15–18 September 2003.

UNIVERSITY OF
ROCHESTER